ANL/FPP-77-1

ANL/FPP-77-1

FUSION POWER PROGRAM
QUARTERLY PROGRESS REPORT

January–March 1977

ARGONNE NATIONAL LABORATORY, ARGONNE, ILLINOIS

Prepared for the U. S. ENERGY RESEARCH
AND DEVELOPMENT ADMINISTRATION
under Contract W-31-109-Eng-38

DISCLAIMER

Printed in the United States of America
Available from
National Technical Information Service
U. S. Department of Commerce
5285 Port Royal Road
Springfield, Virginia 22161
Price: Printed Copy $5.50; Microfiche $3.00

Distribution Category:
Controlled Thermonuclear Processes
and Plasma Physics (UC-20)

ANL/FPP-77-1

ARGONNE NATIONAL LABORATORY
9700 South Cass Avenue
Argonne, Illinois 60439

FUSION POWER PROGRAM
QUARTERLY PROGRESS REPORT

January—March 1977

Weston M. Stacey, Jr., Director
Joseph B. Darby, Jr., Associate Director
Samuel D. Harkness, Associate Director

FOREWORD

This quarterly report describes fusion-related activities in research, development, and reactor design and analysis conducted within the Fusion Power Program and within other programs at Argonne National Laboratory.

Previous quarterly reports issued were:

CTR/TM-11	January—March 1974
CTR/TM-24	April—June 1974
CTR/TM-29	July—September 1974
CTR/TM-38	October—December 1974
ANL/CTR/TM-39	January—March 1975
ANL/CTR/TM-45	April—June 1975
ANL/CTR-75-3	July—September 1975
ANL/CTR-75-5	October—December 1975
ANL/CTR-76-2	January—March 1976
ANL/CTR-76-4	April—June 1976
ANL/CTR-76-5	July—September 1976
ANL/FPP-76-6	October—December 1976

TABLE OF CONTENTS

TABLE OF CONTENTS (Continued)

TABLE OF CONTENTS (Continued)

LIST OF FIGURES

LIST OF FIGURES (Cont.)

LIST OF FIGURES (Cont.)

LIST OF TABLES

I. FUSION REACTOR MATERIALS

A. Plasma Materials Interactions

1. Surface Phenomena Induced by Thermonuclear Plasmas

a. Surface Damage of Stainless Steel Irradiated in Princeton Large Torous (PLT)

S. K. Das and M. Kaminsky, Physics Division

A joint experiment has been started with Princeton Plasma Physics Laboratory (PPPL) in which surface damage of targets irradiated in Princeton's Large Torous (PLT) has been investigated. Two stainless steel targets exposed to plasma discharges in PLT were supplied by Dr. S. Cohen, PPPL. One of the targets was a stainless steel cap for a bolt holding the limiter and was exposed to plasma discharges (predominantly hydrogen) during the period between 12-20-75 and 3-30-76. The other target was a Type 305 stainless steel exposed to H_2, D_2, He, He + Ar, H_2 + Ar plasma discharges during the period between 6-30-76 and 12-1-76. This target was mounted on a flange so that the target surface was recessed by $\sim$ 10 cm from the outer limiter tip and $\sim$ 4 cm from the vacuum wall.

Figures I-1(a) - I-1(c) show scanning electron micrographs of the irradiated area of the stainless steel cap at increasing magnification. The irradiated area appears to have melted (Figure I-1a) and cracked in several places (Figures I-1b and I-1c). It appears possible that the melting could have been caused by runaway electrons. The cracks could have been caused by the severe thermal stress gradients caused by localized melting.

In addition to the melting and cracking, some titanium deposits were also found on the surface (Figure I-1b). Figures I-1(d) and I-1(e) show x-ray spectra from the stainless steel surface and from the deposit, respectively. A large titanium peak can be clearly seen in the spectrum (Figure I-1e) taken from the deposit. The titanium has very likely been released from the titanium bolts (which have lost their protective stainless steel cap) holding the limiter in place.

Examination of the Type 305 stainless steel target did not show any detectable surface damage. Figures I-2(a) and I-2(b) show scanning electron micrographs (SEMs) of the area exposed to plasma discharges at two different magnifications. The scratches seen on the surface were also present in the unirradiated areas (a portion of the target was masked off) shown in Figures I-2(c) and I-2(d), and are due to mechanical polishing. Since the target was recessed $\sim$ 10 cm from the limiter tip and $\sim$ 4 cm from the vacuum wall, it is possible that the target surface had a relatively small exposure to particle fluxes from the plasma discharge. There were approximately 10^4 discharges of $\sim$ 1 second duration; with an estimated flux of $\sim 10^{15}$ particles/cm^2-s to the walls, the maximum exposure of the wall would be $\sim 10^{19}$ particles/cm^2; the particles have a mean energy of $\sim$ 200 ev. Of this exposure to the wall surface, the recessed stainless steel target may have received only a small fraction.

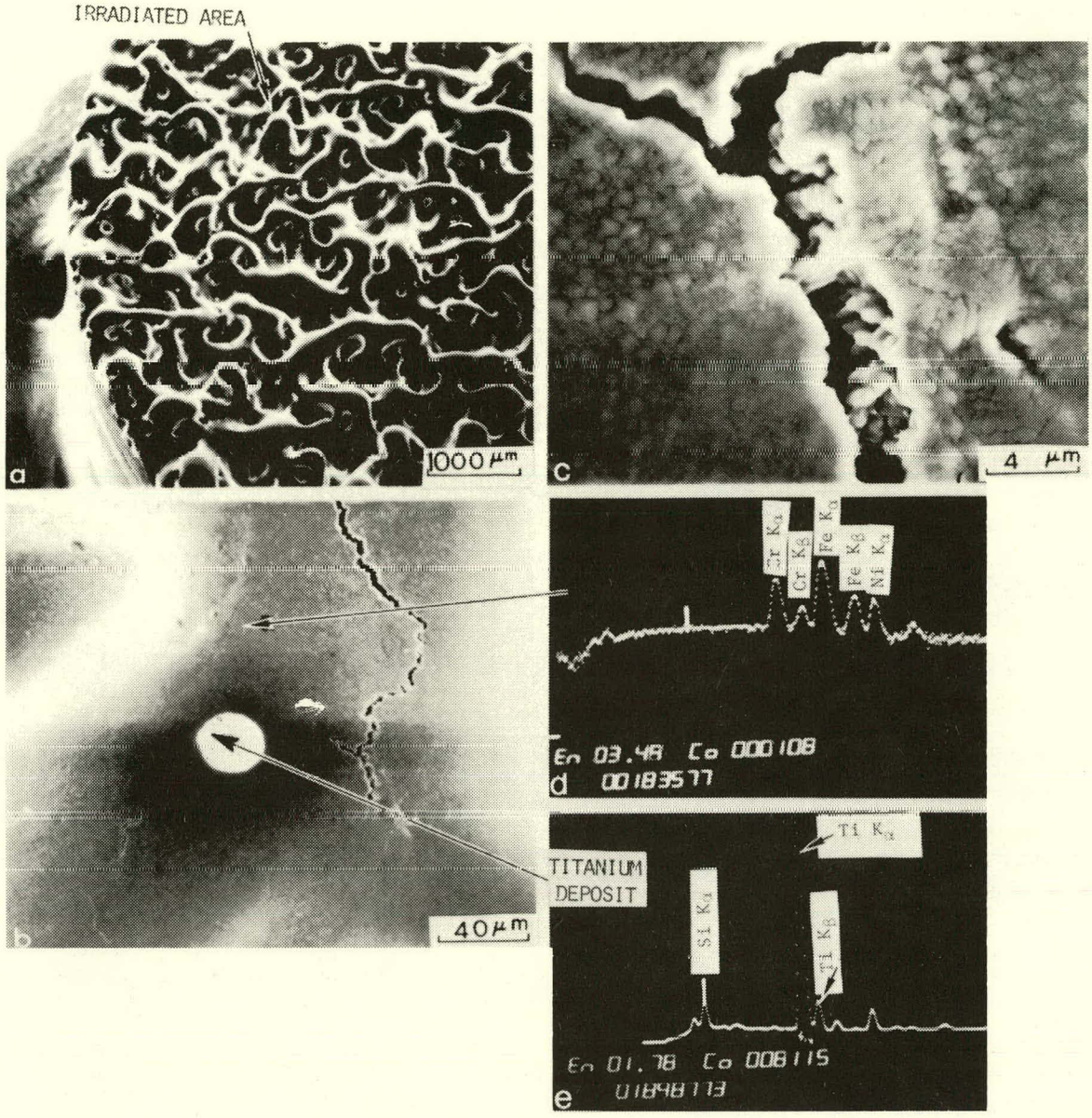

Figure I-1. (a)-(c) Scanning electron micrographs (SEMs) of stainless steel cap for a bolt holding the limiter in PLT; (d) x-ray spectrum of the stainless steel surface from the region marked by arrow in Figure I-1(b); (e) x-ray spectrum of the deposit on the stainless steel surface marked by arrow in Figure I-1(b).

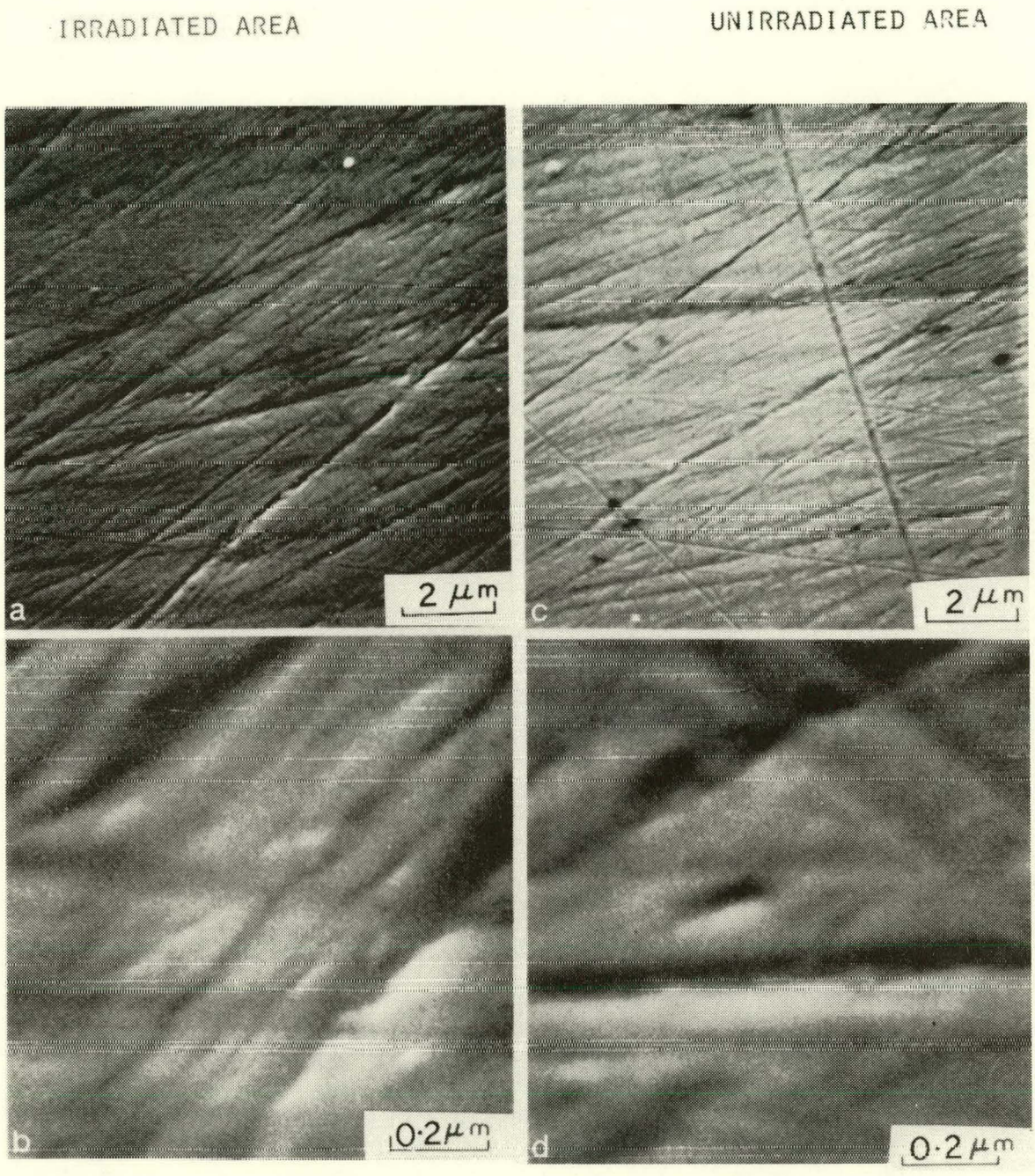

Figure I-2. SEMs of Type 305 stainless steel exposed to plasma discharges in PLT. (a)-(b) irradiated area; (c)-(d) unirradiated area.

b. Radiation Blistering of Nb Implanted Sequentially with He^+ Ions Having an Implant Profile Similar to that Expected in T-20

M. Kaminsky, S. K. Das, M. Guseva,* V. Gusev,* M. Martynenko*

Radiation blistering studies of Nb implanted sequentially with He^+ ions in the energy range 3-500 keV so as to give a uniform helium concentration over large portions of the implant depth were reported recently.[1] The aim of the present joint experiment between Kurchatov Institute, Moscow, and ANL is to study blistering of Nb irradiated with He^+ ions so that the implant profile is similar to that expected in the Russian Tokamak T-20. The energy and the dose of the He^+ ions were chosen to match theoretically calculated He^+ ion spectrum expected in T-20.

In the first set of irradiations cold-worked and annealed Nb targets were irradiated at Kurchatov Institute starting with 0.5 keV He^+ ions and extending up to 90 keV in eleven steps. Subsequently, the same area was irradiated at ANL starting at 150 keV and increased in nine steps up to 3.5 MeV. The irradiations were carried out for total doses of 0.123 C/cm^2 and 1.12 C/cm^2 at ambient temperatures.

Figure I-3(a) and I-3(b) show typical surfaces of annealed polycrystalline Nb after irradiations with $^4He^+$ ions with increasing energies from 0.5-90 keV to a total dose of 0.11 C/cm^2, and after subsequent irradiation with 150 keV-3.5 $^4He^+$ ions to a total dose of 0.013 C/cm^2, respectively. No blisters could be observed after these two irradiations. Figure I-3(c) shows a typical area of cold-worked Nb irradiated with 0.5-90 keV $^4He^+$ ions to a total dose of 0.11 C/cm^2. In contrast with the annealed case (Figure I-3a) the cold-worked surface shows (Figure I-3c) blisters with diameters in the range from $\sim$ 0.3 μm to $\sim$ 4 μm. After subsequent irradiation with 150 keV-3.5 MeV $^4He^+$ ions, no significant change in the surface could be detected (Figure I-3d). The observations of blisters for the cold-worked Nb and not for the annealed Nb (for the same doses) is consistent with our earlier observations that the critical dose for blister appearance is lower for the cold-worked targets than for annealed ones. Figure I-4(a) shows the annealed Nb surfaces after irradiation with 0.5-90 keV $^4He^+$ ions to a higher dose of 1.0 C/cm^2. Now blisters whose diameters fall into several major size clases could be seen. Figure I-4(b) shows the same area as in Figure I-4(a) after subsequent irradiation with 150 keV-3.5 MeV He^+ ions to a dose of 0.12 C/cm^2. After this additional small dose no changes in the surface could be seen. Figure I-4(c) shows the surface of a cold-worked Nb target after irradiation with 0.5-90 keV He^+ ions to a total dose of 1.0 C/cm^2. Here also, blisters whose diameters fall into several major size classes (the size classes can be correlated with He ion energies) can be seen. Further irradiation of the same area (as in Figure I-4c) with 150 keV-3.5 MeV $^4He^+$ ions does not cause (Figure I-4d) any detectable change. These results indicate a trend in blister formation

---

* Kurchatov Institute, Moscow, U.S.S.R.

[1] M. I. Guseva, et al., CTR Quarterly Progress Report, January-March, 1976, Argonne National Laboratory, ANL/CTR-76-2, see also J. Nucl. Mat. 63 (1976) 245.

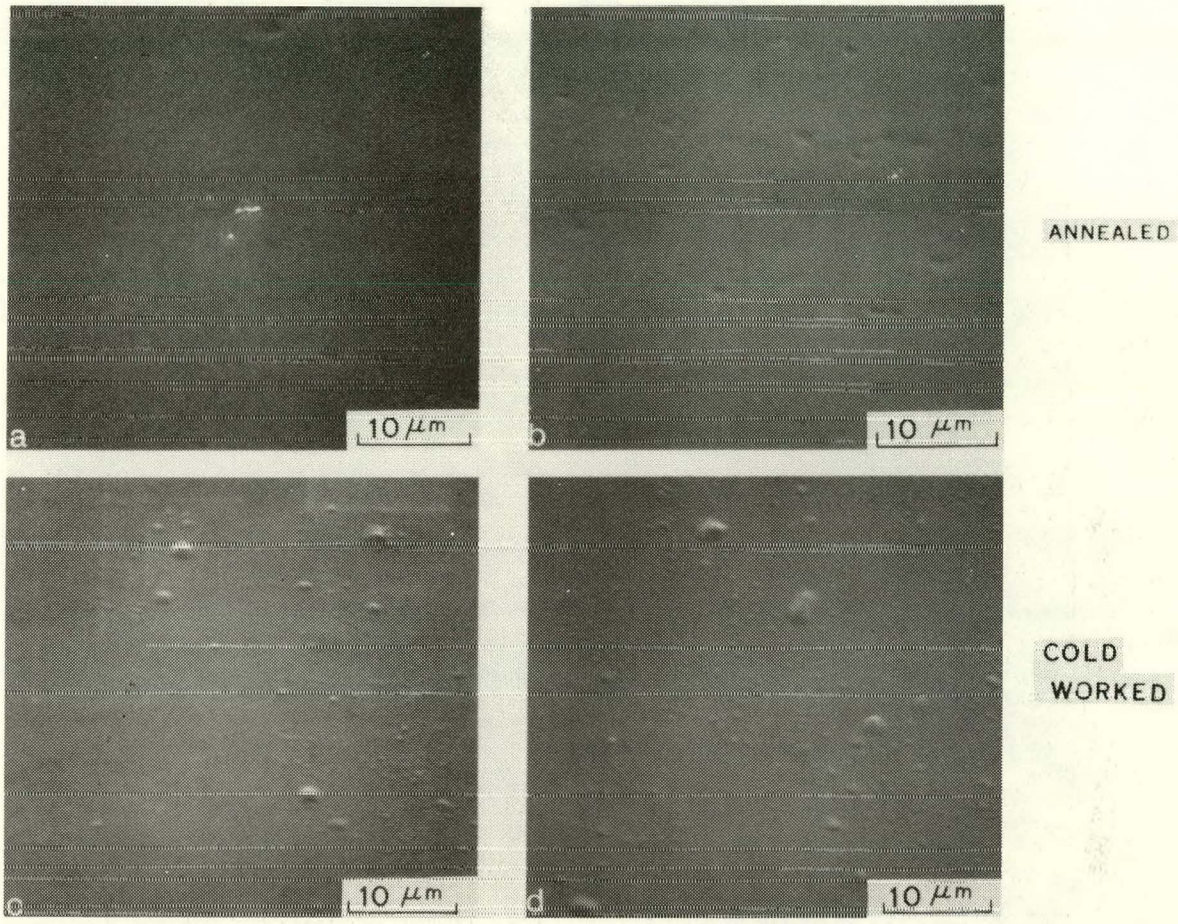

Figure I-3. SEMs of polycrystalline Nb surfaces irradiated at room temperature with $^4He^+$ ions: (a) annealed Nb after 0.5-90 keV $^4He^+$ irradiation to a dose of 0.11 C/cm^2 at Kurchatov; (b) annealed Nb after further irradiation at ANL with 150 keV-3.5-MeV $^4He^+$ ions to an additional dose of 0.013 C/cm^2; (c) cold-worked Nb after same irradiation as in (a); (d) cold-worked Nb after the same irradiation as in (b).

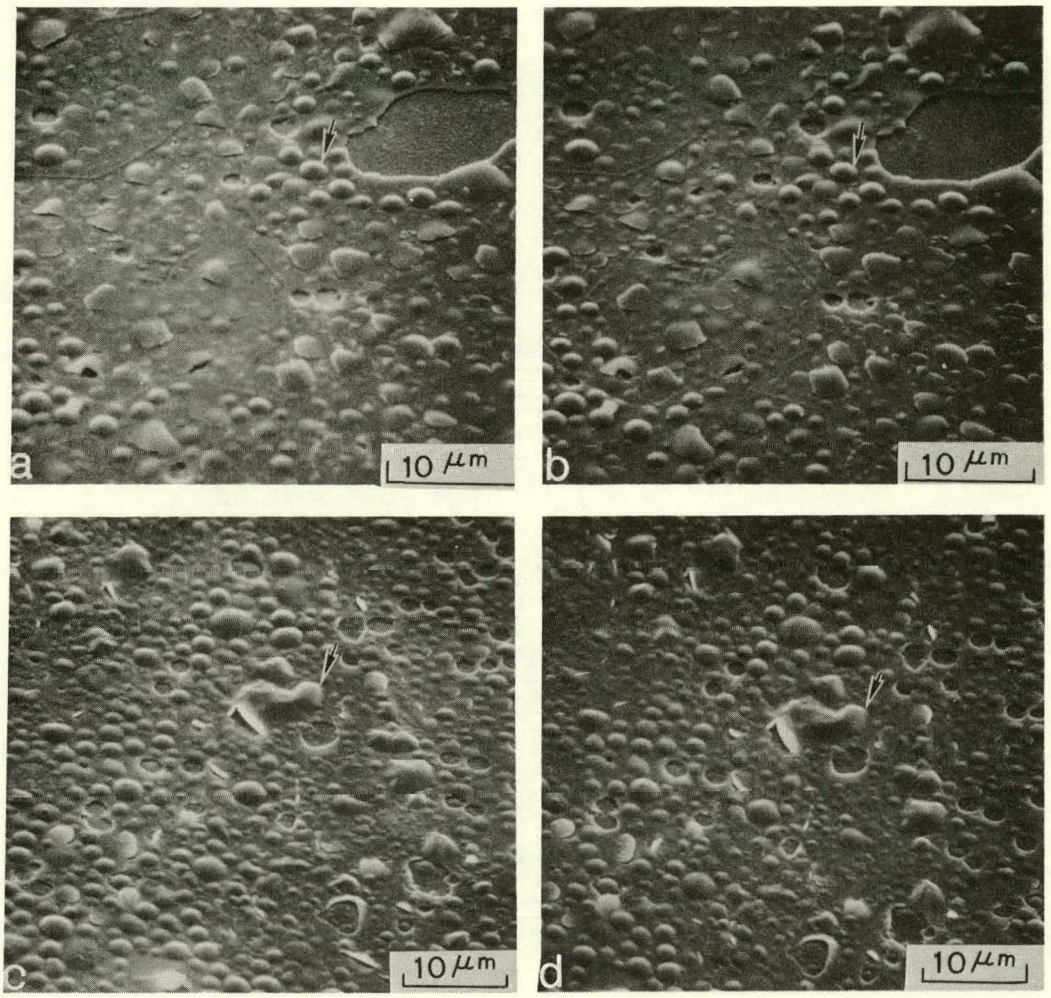

Figure I-4. SEMs of polycrystalline Nb surfaces irradiated at room temperature with $^4He^+$ ions: (a) annealed Nb after 0.5-90 keV $^4He^+$ irradiation to a dose of 1.0 C/cm^2 at Kurchatov; (b) same area as in Figure I-4(a) but after further irradiation at ANL with 150 keV-3.5 MeV $^4He^+$ ions to an additional dose of 0.12 C/cm^2; (c) cold-worked Nb after 0.5-90 keV $^4He^+$ ion irradiation to a dose of 1.0 C/cm^2 at Kurchatov; (d) same area as in Figure I-4(c) but after further irradiation at ANL with 150 keV-3.5 MeV $^4He^+$ ions to an additional dose of 0.12 C/cm^2.

by sequential irradiation of surfaces with helium ions at different energies, which is compatible with our previous results of sequential irradiations in the energy range 3-500 keV.[1]

Experiments are in progress where the irradiations were started at high energy and continued to lower energies.

2. Light Emission from Ion Bombarded Surfaces

D. M. Gruen and R. B. Wright, Chemistry Division

The upgrading of the duoplasmatron ion source facility has been completed. Additions to the facility include a 6" oil diffusion pump and liquid N_2 trap which enable base pressures of 3×10^{-8} torr to be routinely obtained. The ion optics of the facility were improved by the addition of a gridded Einzel lens system for focusing the mass analyzed ion beam onto the target. Mass analysis is accomplished by a 45° double-focusing magnet which was also part of the upgrading. The new target chamber, separated from the ion source vacuum chamber by a Conflat flange sealed stainless steel gate valve, is provided with multiple Conflat flange sealed access ports for target insertion, pressure measurements and viewing ports, and allows various size beam defining apertures to be installed so that the beam size at the target can be controlled. The target chamber is further pumped (1×10^{-8} base pressure) by a 2" oil diffusion pump and liquid N_2 trap. Provision has also been made for cryopumping (14°K) the chamber with a closed cycle helium refrigerator coupled to a copper cryopanel which surrounds the target during ion bombardment. Routine beam currents of 220 μA H_1^+, 130 μA H_2^+, 150 μA H_3^+, 210 μA D_1^+, 120 μA D_2^+, 140 μA D_3^+, 175 μA He^+, and 100 μA Ar^+ at 15 keV on a 1 cm^2 area are presently achieved.

A Varian model #981-2043 ion bombardment gun (0-3 keV) can also be incorporated into the target chamber which can be used separately for ion bombardment or simultaneously with the duoplasmatron ion source for synergistic investigations. This ion source will operate with H_2, D_2, N_2, O_2, He, Ar, Kr and Xe gases but the resulting ion beam is not mass separated.

Three major *in situ* surface analytical techniques will be used in conjunction with the duoplasmatron facility: SIMS for determining the mass, ion fraction and energy of sputtered products (described in ANL/CTR-76-2); matrix isolation spectroscopy for the characterization of the neutral sputtered products in their ground states (described in ANL/CTR-75-3); and SCANIIR for measuring the excited electronic states of neutral and ionic sputtered products during ion bombardment. Bombardment of samples for later study outside the target chamber can of course also be done.

Equipment for utilizing the surface analysis technique known as SCANIIR (Surface Composition by Analysis of Neutral and Ion Impact Radiation) has been assembled and is currently being used in experimental studies of physichemical sputtering. The target chamber of the duoplasmatron facility has been equipped with a Conflat flange mounted LiF window assembly from the Harshaw Chemical Co. (2.1" diameter optical opening) for transmission of the optical radiation emitted by the electronically excited sputtered particles (transmission from 7 μ to 1216 Å). The optical radiation is focused

by a quartz Supracil 1 lens (50 mm diameter, focal length 75 mm) onto the entrance slit of a McPherson Model #218 vacuum or atmospheric scanning monochromator. Two gratings are presently available: 2400 groove/mm, blazed at 3000 Å and MgF_2 overcoated (1050 to 5000 Å spectral range); and 1200 groove/mm, blazed at 5000 Å and MgF_2 overcoated (1050 to 10,000 Å spectral range). Detection of the dispersed radiation is by an RCA C31034A-02 (2000-9300 Å) photomultiplier tube which is cooled to -25°C by a Products for Research, Inc. model TE-104TS-RF thermoelectric refrigerated photomultiplier tube housing. The output of the PM tube is processed by an Ortec, Inc. photon counting system (9301 preamplifier, 9302 amplifier/discriminator, 9340 log/lin ratemeter or a 9315 photon counter, 9325 digital/analog converter). The spectra are then displayed on a Hewlett Packard 7101B strip chart recorder.

The materials investigated so far include Ti, Cu, Si, SiO_2 and graphite. Atomic line spectra of the target material were observed in all cases with a 15 keV Ar^+ incident ion beam. With the graphite sample, in addition to atomic carbon lines, a spectral band indicative of C_2 was also detected. Incident beams of 15 keV H^+ or D^+ produced very weak atomic line spectra and also the Balmer series atomic spectra resulting from the backscattered neutral incident projectiles. Incident He^+ also gives rise to atomic line spectra characteristic of backscattered He atoms.

3. Electromigration in Ion Bombardment*

W. Primak, E. Monahan, Solid State Science Division

Although electromigration has been known for many years, it does not appear to have been recognized as a deterioration mechanism for surfaces of materials exposed to charged particle bombardment. Spectacular effects caused by electromigration of alkali ions have been observed recently in the course of an investigation of the properties of glasses for insulator applications in radiation environments such as occur in fusion power devices, reactors, accelerators and in the solid storage of radioactive wastes. Another example was found during an investigation of the stability of lithium niobate intended for acoustical monitoring of LMFBR's.

The effect was encountered first in the case of Pyrex glass bombarded with either protons or helium ions at about 400°C. An altered surface layer with a thickness several times the range of the bombarding ions was seen in optical measurements. This thickness proved to be that containing the alkali equivalent to the incident ion charge. The thickness was particularly large in the case of Pyrex glass because the alkali content of this glass is low. Other glasses having a higher alkali content were studied next; and for these, also, the altered layer was of the thickness containing the alkali equivalent to the incident charge. In the case of one borosilicate crown glass sample (Schott u. Gen., Type BK-7) which was bombarded at 375°C, the altered layer was 0.6 of the range.

In the case of the Pyrex glass samples, the surface was observed to have collapsed. Such collapse had been reported previously for glasses subjected to electrolysis (ion-depletion studies).

---

* Reported to the Division of Physical Research, March, 1977. Reported to the American Physical Society at Chicago, Illinois, February 7, 1977.

In the case of a crown glass (Type C-1) subjected to helium ion bombardment at elevated temperatures, a frothiness just resolvable under the microscope was found. Since there is no evidence for helium trapping causing blistering in this material on helium ion bombardment at room temperature, and since trapping is expected to be diminished on elevating the temperature, it is speculated that the frothiness may be caused by oxygen, the negative ion, electromigrating to the surface.

The above results were obtained with 140 keV protons and helium ions. A more complex electromigration phenomenon was observed for a lithium niobate sample bombarded with deuterons at 600°C. An altered layer 1/10 of the range was found. This corresponded to the thickness containing half the alkali equivalent to the incident charge. This behavior can be explained by the hypothesis that in addition to the electromigration of lithium, the niobium was reduced in valency by one.

Electromigration resulting from charged particle bombardment of materials at elevated temperatures may prove to be a severe problem in a variety of applications including thermonuclear reactor first walls. Unlike other surface bombardment problems, it involves not only a layer with the thickness of the particle range, but the whole thickness of the material. Moreover, the electromigration problem may prove particularly bad for coatings, where ions might migrate to interfaces and could cause detachment of the coating; or ions from the substrate might be electrolyzed into the coating and change its properties.

B. Alloy Development for Irradiation Performance

1. Irradiation-Induced Swelling in Dual-Ion-Irradiated Fe-15Cr-20Ni Alloy

S. C. Agarwal, B. Okray Hall, A. Taylor and F. V. Nolfi, Jr., Materials Science Division

An Fe-15Cr-20Ni alloy was selected for initial dual-ion experiments since its swelling behavior has been well-characterized by Johnston, et al.,[2] for Ni^+ irradiation of specimens preinjected with 15 appm He. From a 10-mil-thick cold-rolled strip procured from W. G. Johnston, 3-mm-diameter specimens were prepared and then simultaneously bombarded with $^{58}Ni^+$ and $^3He^+$ ions at the ANL 4-MeV Dual-beam Irradiation Facility. The alloy condition and various other run parameters used are listed in Table I-1. Following irradiation, the specimens were sectioned to a depth of $\sim$ 5500 Å from the irradiated surface and then thinned from the back for TEM studies.

TEM examination of the 25-dpa specimens for the three He:dpa ratios has been completed, and the results are summarized in Table I-2. The observed cavity size for the two higher He:dpa ratios (100:1 and 50:1) is about twice

---

[2] W. G. Johnston, T. Lauritzen, J. H. Rosolowski, and A. J. Turkalo, G. E. Technical Inforamtion Series, Report #76CRD019 (1976).

Table I-1. Summary of Dual-beam Irradiation of an Fe-15Cr-20Ni Alloy

Alloy	Fe-15Cr-20Ni (composition in wt %)
Alloy Condition	Vacuum-annealed ($\sim 10^{-7}$ torr) at 1020°C for 30 min and then He quenched
Nominal Run Temperature	660°C
Bombarding Ions	3.5 MeV $^{58}Ni^{+}$ and foil degraded 1.18 MeV $^{3}He^{+}$
Ni^{+} Dose Rate	$\sim$ .0 x 10^{-3} dpa s^{-1}
He:dpa Ratio[a] (appm/dpa)	100:1 (10^{-4} α/disp), 50:1 (5 x 10^{-5} α/disp) and 10:1 (10^{-5} α/disp)
Ni^{+} Doses for each He:dpa Ratio (dpa)[b]	25, 17, 6, and 3

[a] Nominal values

[b] All specimens received 1-min exposure to ^{3}He beam before the Ni^{+} beam was turned on.

Table I-2. Swelling in Fe-15Cr-20Ni Alloy Irradiated at 660°C with 3.5-MeV Ni^{+} + 1.18-MeV $^{3}He^{+}$ Ions (Ni^{+} Dose Rate 3.0 x 10^{-3} dpa s^{-1})

He:dpa Ratio (appm/dpa)	100:1 (10^{-4} α/disp)	50:1 (5 x 10^{-5} α/disp)	10:1 (10^{-5} α/disp)
Total Dose (dpa)	25	25	25
Average Cavity Diameter (Å)	381	406	216
Average Cavity Density (cm^{-3})	2.97 x 10^{14}	1.32 x 10^{14}	1.55 x 10^{15}
Average Swelling ΔV/V (%)	1.05	0.55	1.03
Estimated Number of He Atoms Injected (cm^{-3})[a]	2.1 x 10^{20}	1.0 x 10^{20}	2.1 x 10^{19}
Estimated Number of He Atoms Needed if Observed Cavities were Equilibrium He Bubbles (cm^{-3})[b]	1.13 x 10^{20}	5.63 x 10^{19}	1.87 x 10^{20}

[a] The density and atomic weight values used were those for pure Fe.

[b] Surface-energy value used was 1500 ergs cm^{-2}.

as large as for the lowest ratio (10:1). The observed swelling for the lowest and the highest He concentrations is about the same ($\sim$ 1.0%) and is approximately twice as large as for the intermediate He concentration ($\sim$ 0.55%). These differences in swelling are taken into account in the observed differences in cavity densities for the three specimens. Moreover, the calculations indicate that, in the two higher He specimens, the cavities may well be near equilibrium He-bubbles, whereas in the lowest helium specimen the concentration of implanted He is only one-tenth of what would be needed for equilibrium bubbles.

Johnston, et al.[2] irradiated the alloy used in this investigation with 5-MeV Ni^{+} ions at 675°C and a dose rate of 10^{-2} dpa/s^{-1}. The specimens had been preinjected with 15-appm He. These investigators observed 10% swelling at 25 dpa, which is in contrast to the 1% swelling at 25 dpa reported here. The dose rate used in the present experiments is $\sim$ 1/3 of that employed by Johnston, et al.,[2] and the run temperature is also lower (660 vs 675°C). The reasons for these differences in observed swelling levels are not clear, but it is questionable that they can be accounted for by the differences in run temperatures and dose rates.

Metallographic examination of as-irradiated surfaces revealed swelling steps in the highest and lowest He:dpa-ratio specimens, which is consistent with TEM results that show higher swelling for these specimens. However, resolvable steps were not observed in the 50:1 specimens. Typical cavity structures for the three He concentrations are shown in Figure I-5. Under strong two-beam contrast conditions, most of the cavities are observed to have nucleated on dislocations. The dislocation structure in the 25-dpa specimens consists mainly of networks with only a few loops. Preliminary observations of the population of cavities on grain boundaries (GB) show denuded zones near GB only in grains with {001} orientation. The distribution of cavities near and through GB between grains of other orientations (mostly {110}) is the same as observed in the matrix. An attempt is being made to find an explanation for these observations.

2. Nucleation Theory

B. Okray Hall and H. Wiedersich, Materials Science Division

A comprehensive time-dependent nucleation and growth model of dislocation loops, voids, and helium bubbles is being developed to describe the microstructural evolution in the first wall of a fusion-reactor during irradiation and simultaneous helium production. The model is built up in stages. The early development of the interstitial loop microstructure in irradiated materials is being examined, using the time-dependent nucleation model described in a previous report.[3] Using parameters typical of nickel, the interstitial loop size distributions and concentrations were calculated as a function of time for several temperatures, displacement rates, and sink-annihilation probabilities.

---

[3] Fusion Power Program Quarterly Progress Report, October-December, 1976, Argonne National Laboratory, ANL/FPP-76-6, (1977).

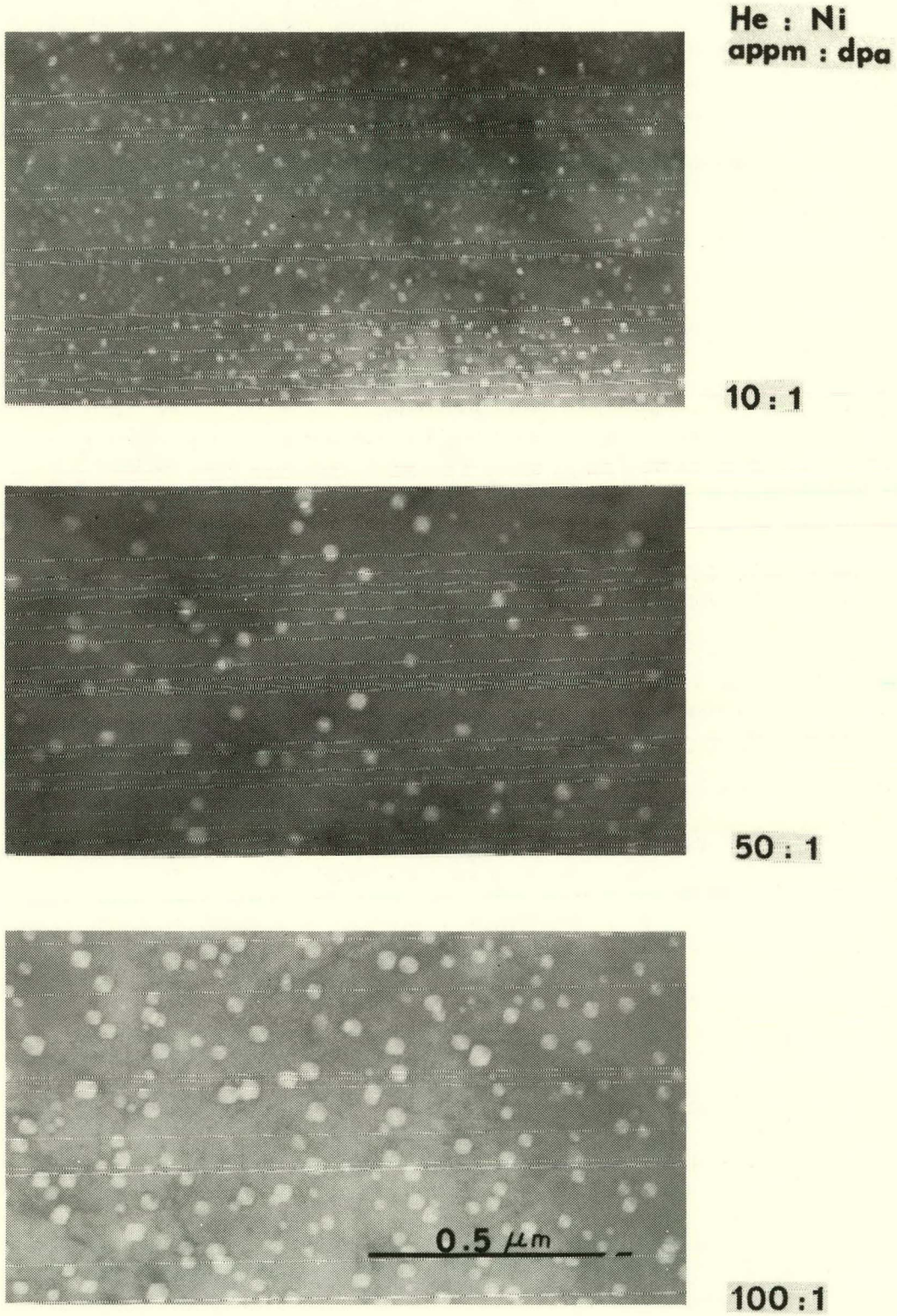

Figure I-5. Cavity Microstructure in Fe-15Cr-20Ni Dual-ion-irradiated to a Dose of 25 dpa.

The loop number densities typical of the irradiation conditions are established in very short times, corresponding to doses of $\sim 10^{-5}$ displacements per atom (dpa). Figure I-6 shows the variation of number density with time for a displacement rate $\dot{n} = 10^{-4}$ dpa/s, a sink-annihilation probability of 10^{-7} (corresponding to a dislocation density of $\sim 10^{8}$ cm/cm^3), and several temperatures. As the temperature increases, the apparent saturation or steady-state value of the loop number density decreases. An increase in the sink-annihilation probability also lowers the number density, whereas an increase in displacement rate increases the steady-state value. These qualitative trends, including the order of magnitude of the loop number density, are consistent with the limited experimental evidence available.

When the number density nears its saturation value, the interstitial clusters are small, typically containing 20-25 interstitials. Figure I-7 shows loop concentrations as a function of the number of interstitials in the cluster for several times. At very short times the size distribution falls off from a maximum for single interstitials. As the irradiation progresses, the interstitial population decreases as a result of either loss to the nucleated loops and/or by recombination with vacancies, and the maximum of the size distribution moves toward larger sizes. The distribution broadens with time and the height of the maximum decreases.

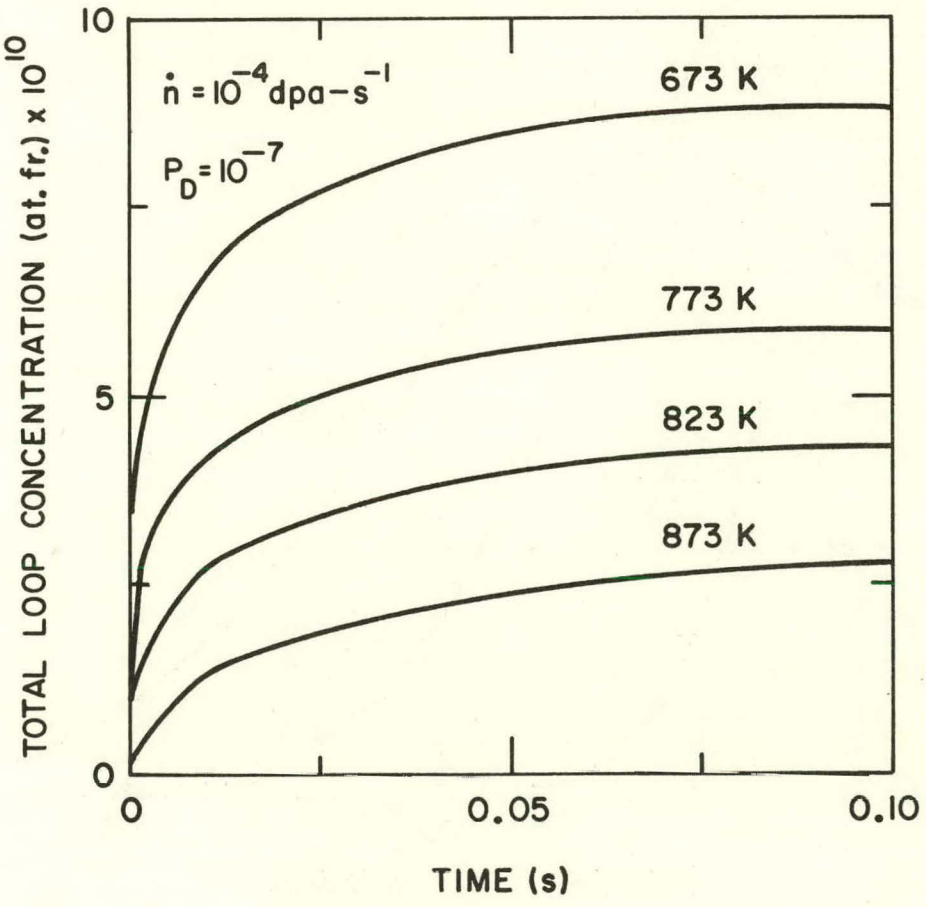

Figure I-6. Total loop concentration (at. fr.) as a function of time for several temperatures. Displacement rate = 10^{-4} dpa-s^{-1}. Sink-annihilation probability = 10^{-7}. Note atom fraction of 10^{-9} equals 10^{14} loops/cm^3.

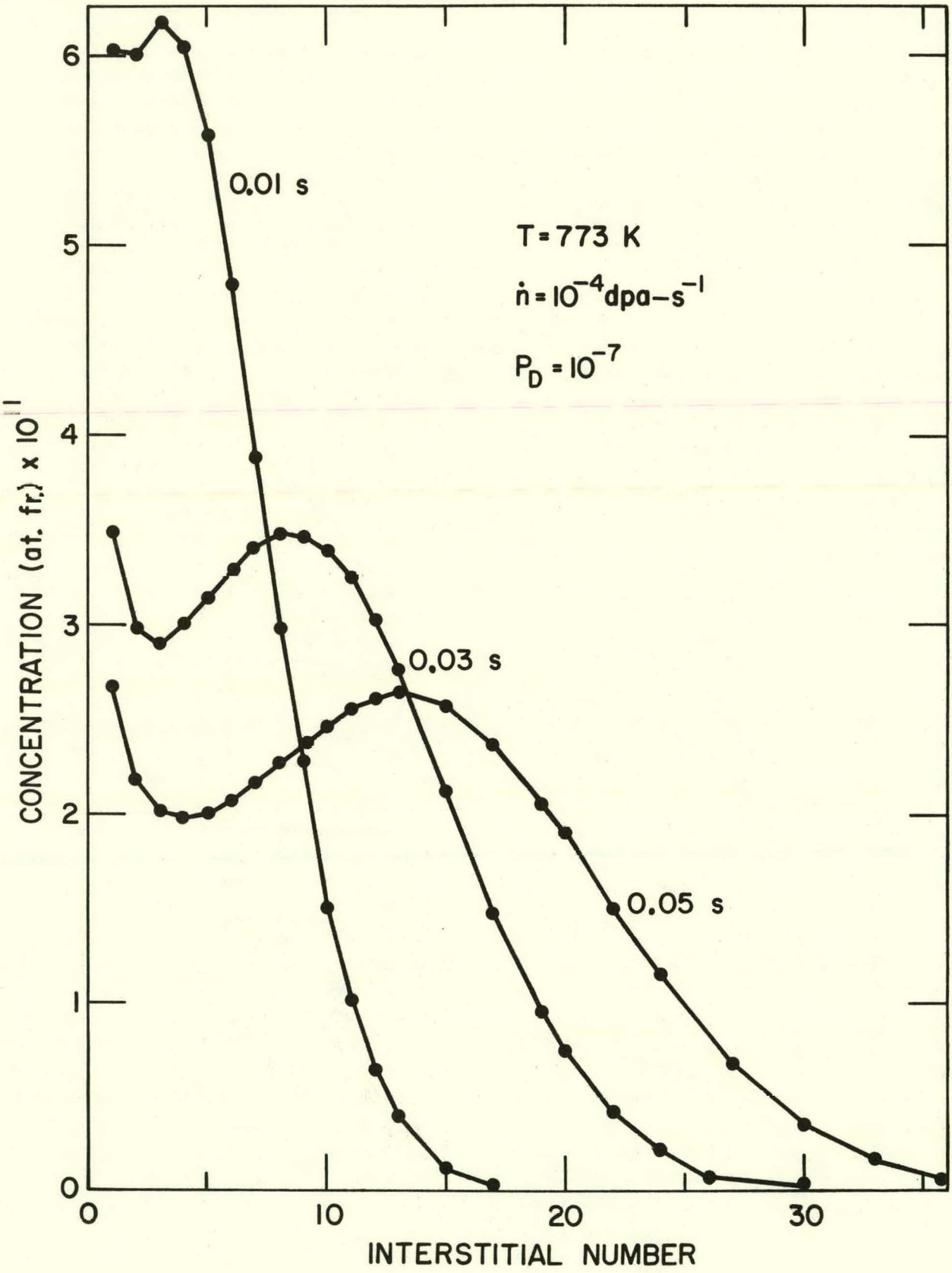

Figure I-7. Interstitial cluster-size distribution at several times. Temperature = 773 K. Sink-annihilation probability = 10^{-7}. Displacement rate = 10^{-4} dpa-s^{-1}.

The loop concentration reaches a steady-state value early in the irradiation before the vacancy supersaturation becomes sufficiently high for vacancy clustering to occur. Loop nucleation and void nucleation are therefore sequential rather than simultaneous, and only loop growth need be considered during the void nucleation period.

An experiment designed to study loop-size distributions in nickel and several nickel alloys bombarded with Ni^+ ions to low doses (< 1 dpa) is currently underway in cooperation with D. I. Potter under DPR-funding.

3. Helium-bubble Formation in V-15Cr-5Ti at Elevated Temperatures

R. F. Mattas, Materials Science Division

Helium embrittlement in metals poses a potentially serious problem to the integrity of the first wall of a fusion reactor. It is believed that helium produced by (n,α) reactions aggregates along grain boundaries and promotes grain-boundary failure. Two known methods can be used to simulate helium production by (n,α) reactions, helium-ion implantation and decay of tritium to ^3He in tritium-doped materials. Recently, tensile tests at temperatures between 600 and 900°C were conducted on V-15Cr-5Ti specimens that contained helium introduced by the two simulation methods.[4,5] The helium concentration in the ion implanted specimens was 25 appm, and the helium concentration in the tritium decay specimens ranged from 27 to 39 appm. The test results indicated that large reductions in ductility occurred at ∿ 700°C and above in samples containing helium introduced by tritium decay, whereas reductions in ductility of similar magnitude occurred at ∿ 750°C and above in samples containing helium introduced by ion bombardment. A possible reason for the shift in temperature of the onset of ductility loss may be due to the difference in helium-bubble distributions produced by the two simulation methods. The size distribution and locations of the bubbles would be expected to influence embrittlement. To test this hypothesis, transmission-electron microscopy (TEM) has been used to examine the distribution and annealing kinetics of helium bubbles in V-15Cr-5Ti samples in which the helium was introduced by tritium decay.

The TEM specimens, which contained ∿ 30 appm He, were punched out of the grip ends of the tensile specimens used for the embrittlement experiment. The doping procedure used to introduce the helium by tritium decay has been described previously.[4] These samples, as well as control samples that contained no helium were annealed for 30 min at temperatures ranging from 800 to 1150°C. The temperature of the samples was measured by an optical pyrometer, and the expected accuracy of the measurements was ± 5°C. The annealing treatments were carried out in a dynamic vacuum of ∿ 2×10^{-8} torr. Following the annealing, the samples were thinned for TEM examination.

---

[4] R. F. Mattas, H. Wiedersich, D. G. Atteridge, A. B. Johnson, and J. F. Remark, "Elevated-temperature Tensile Properties of V-15Cr-5Ti Containing Helium Introduced by Ion Bombardment and Tritium Decay," Second Topical Meeting on the Technology of Controlled Nuclear Fusion, Vol. 1, 199 (1976).

[5] A. T. Santhanam, A. Taylor, and S. D. Harkness, "Charged-particle Simulation Studies of Vanadium and Vanadium Alloys," in Defects and Defect Clusters in BCC Metals and Their Alloys, R. J. Arsenault, ed., 18, 175 (1976).

Helium bubbles were observed in all samples annealed at temperatures between 800 and 1150°C. The bubbles occurred at three primary locations: at the grain boundaries, at the surfaces of large precipitates, and in clusters in the matrix in association with small plate-like precipitates. Examples of these locations are shown in Figure I-8. The platelets have a {100} habit plane and are similar in appearance to the $V_{16}N$ precipitates observed in nitrogen-doped vanadium.[6] A high density of coherent platelets was also observed in an ion bombarded specimen which was tensile tested at 850°C. Under two-beam diffraction conditions, the plate-like precipitates obscure the helium bubbles (Figure I-8a). Kinematic conditions are necessary to observe the bubbles (Figure I-8b). The large precipitates were observed after annealing

[6] D. Shah and C. Altstetter, Mat. Sci. Eng., 26, 175 (1976).

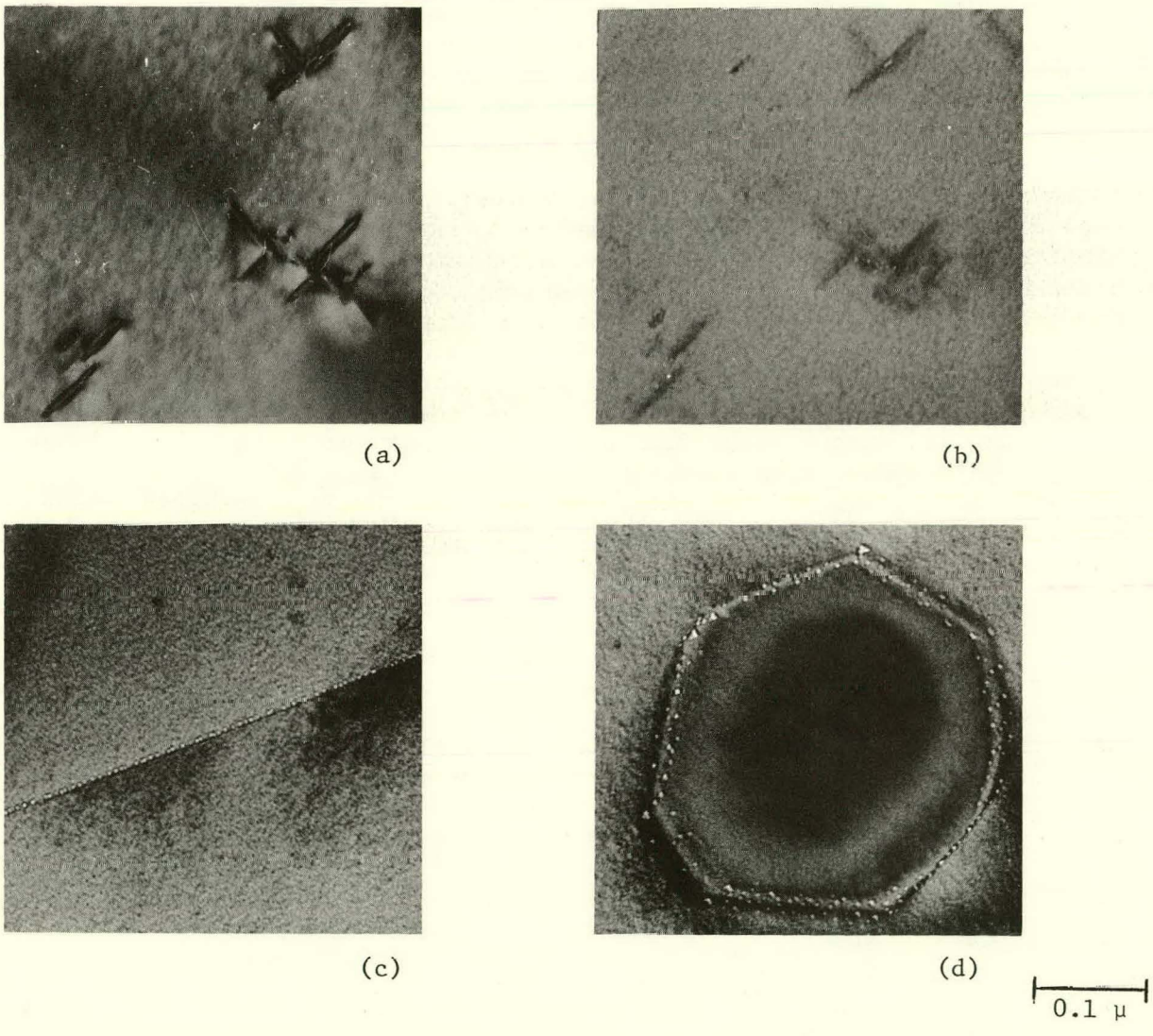

Figure I-8. Plate precipitates after annealing at 850°C; (a) two-beam diffraction conditions, and (b) kinematical conditions. Helium-bubble distributions after annealing at 950°C; (c) at a grain boundary and (d) at a large precipitate.

at all temperatures, but platelets were observed only in the 800-900°C range. At temperatures above 900°C, the platelets apparently had dissolved, leaving only helium bubble clusters in the matrix.

After the bubbles were formed by annealing, they did not appear to migrate over large distances. However, a general coarsening of the bubble distribution occurred as the annealing temperature increased. The coarsening of the bubbles in the matrix is shown in Figure I-9. At 800°C, the average bubble size was ∿ 17 Å in diameter, whereas at 1100°C, the average diameter was ∿ 48 Å. As the diameter increased, the bubbles took on a cubic or oblong shape. This faceting of the bubbles also occurred on the grain boundaries as well as on the surfaces of the precipitates.

A TEM examination of tensile specimens tested at 850°C, containing helium introduced by ion bombardment, revealed the presence of only a few helium bubbles at grain-boundary triple points.[5] Thus, the two methods of introducing helium into the samples lead to different bubble distribution.

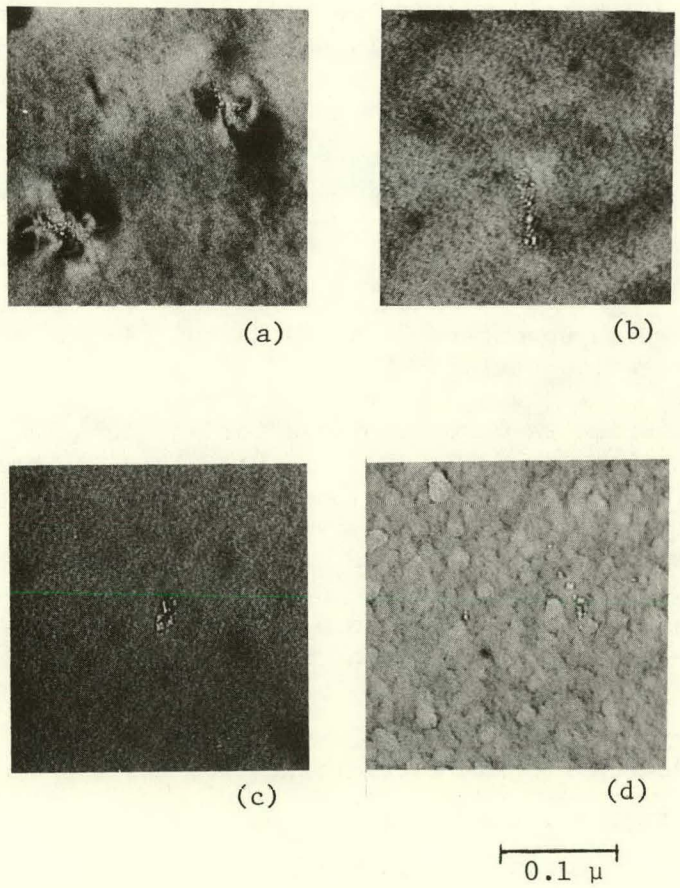

Figure I-9. Helium-bubble clusters in matrix at annealing temperatures of (a) 800°C, (b) 900°C, (c) 1000°C, and (d) 1100°C.

C. Special Purpose Materials Development

1. Development of Barriers to Tritium Migration in Fusion Devices and Reactors

V. A. Maroni, Chemical Engineering Division

Current emphasis in the barrier development program is being placed on methods for developing thin, resilient, permeation resistant coatings on stainless steels and other potential construction materials for near term fusion devices.[7] At least three approaches to this problem appear to exist. (1) Coatings that develop naturally on austenitic materials may provide the required permeation resistance in cases where the integrity of the surface layer is not overly sensitive to environment. (2) Materials that develop contiguous stable coatings in a wide range of environments could be applied in thin layers directly to the surfaces of austenitic alloys. And (3) The composition of conventional alloys could be modified to include additive elements which demonstrably improve the resiliency of the surface coatings that normally form on these alloys. The latter two approaches are presently being pursued in our laboratory. In addition, we have completed a study of the magnitude of permeation resistance (over and above that of the pure material) that is likely to be required by the more prominent classes of construction materials considered for service in fusion reactors. Progress during the second quarter of FY-1977 is summarized below.

---

[7] W. M. Stacey, Jr., et al., Fusion Power Program Quarterly Progress Report, October-December, 1976, Argonne National Laboratory, ANL/FPP-76-6 (1977).

a. Permeation Studies

E. H. Van Deventer, V. A. MacLaren,* V. A. Maroni, Chemical Engineering Division

Permeation measurements were completed for an aluminum modified 400-series stainless steel† (18 w/o Cr, 0.5 w/o Ni, 2 w/o Al, bal. Fe) and a sample of 321-SS with an aluminum/aluminum oxide/aluminum sputter deposited laminar‡ coating approximately 4 μm in overall thickness. Results for the modified 400-series stainless steel are shown in Figure I-10 together with the permeation curve for 430-SS (16 w/o Cr, bal. Fe) obtained from literature data.[8] The numbers indicate the chronological order of data gathering; the open circles represent data obtained on the as-received material in our high vacuum permeation apparatus without any pretreatment; and the triangles

---

* Undergraduate Research Program Participant from North Dakota State University.

† Obtained from Thermacore, Inc.

‡ Prepared by Grumman Aerospace Corporation.

[8] D. W. Rudd and J. B. Vetrano, "Permeability of Metals and Enameled Metals to Hydrogen," Atomics International Report, NAA-SR-6109 (October, 1961).

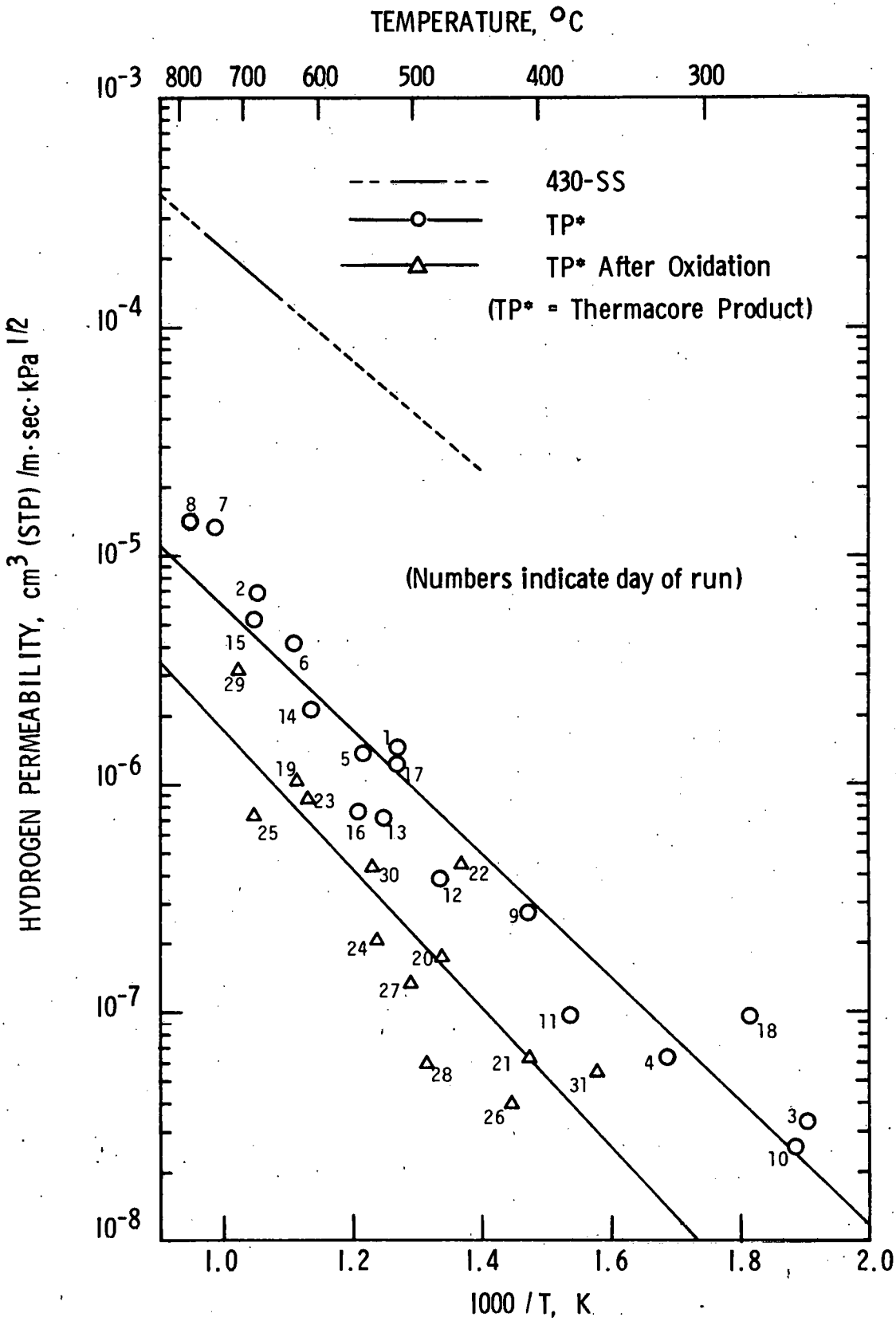

Figure I-10. Hydrogen permeation data for the aluminum modified 400-series SS (Thermacore Product) and literature data for 430-SS.

represent data obtained in the same apparatus after exposure of the downstream side of the sample to air at 730°C for three hours. The overall reduction in permeation observed after exposure of the sample (lower curve in Figure I-10) when compared to the 430-SS data is over 150-X. Results for the laminar coated 321-SS sample showed only a modest reduction in permeability compared to uncoated 321-SS ($\sim$ 20-X) and were generally less encouraging than the previously reported data for a pure aluminum coated 321-SS sample.[7]

During the second quarter of FY-1977, extensive metallurgical analyses of the two samples described above and of a number of samples from previous permeation studies were initiated. The analytical methods currently being employed include electron microprobe examinations and scanning electron microscopy. From correlations of permeation data with surface morphology for different types of barrier samples, we find that thicker surface coatings actually seem to lead to correspondingly poorer barrier performance. This may be due in part to increased stress related cracking with the thicker coatings. Future studies will attempt to address this question in a more systematic way.

Another recently started project involves modification of the upstream portion of the hydrogen permeation apparatus to permit measurements at lower hydrogen driving pressures than are presently accessible and in a better characterized environment. Added features to the upstream compartment will include a mass spectrometer, a low range capacitance manometer (to 10^{-5} torr), and a trap to collect nonmetallic impurities.

b. Analysis of Permeation Barrier Requirements

V. A. MacLaren and V. A. Maroni, Chemical Engineering Division

In the previous progress report,[7] we described the initial results of an attempt to determine permeation barrier requirements for various structural metals and alloys based on a model which normalizes a given material's hydrogen permeability against its thermal conductivity. Arguments for the reasonableness of this approach as a first order of approximation were given in Reference 7 and will be expanded upon in subsequent publications.[9,10] During the second quarter of FY-1977 the temperature dependence of thermal conductivity (which had been ignored in our earlier efforts) was worked into the model, a computer code to execute the calculations was written, and additional permeation data sets inclusive of an increased number of materials were analyzed. Fitting parameters for the thermal conductivity and tritium permeability extracted and adjusted along the lines described previously[7] are given in Table I-3. (References to the actual sources of data will be included in a subsequent publication.[10]) Results of calculations using these fitting parameters are presented in Table I-4 for a base case reactor having the following characteristics: (1) thermal power = 5000 MW, (2) heat exchanger wall temperature

---

[9] V. A. Maroni, "Some Perspective on Tritium Permeation in Fusion Reactors Based on Existing Data and Experience," Transactions of the 1977 ANS Annual Meeting, June 12-16, 1977, New York, New York.

[10] V. A. Maroni, "Survey of Hydrogen Isotope Permeation Data for Metals and Alloys," Argonne National Laboratory (report in preparation).

Table I-3. Summary of Permeability and Thermal Conductivity Input Constants For Metals and Alloys

Thermal Conductivity, Watt/cm-°K = A + B*T(°K)

Permeability, Ci/cm-Day (Torr**0.5) = Phi*exp(-QP/RT)

Material[a]	A	B	QP	PHI
Vanadium (UL)	2.720E-01	1.150E-04	1.420E 01	6.330E 04
Vanadium (LL)	2.720E-01	1.150E-04	1.500E 01	1.300E 00
Niobium (AVG)	2.380E-01	1.540E-04	3.400E 00	1.340E 02
Niobium (UL)	2.380E-01	1.540E-04	5.200E 00	2.600E 02
Niobium (LL)	2.380E-01	1.540E-04	1.700E 01	8.260E 02
Molybdenum	1.470E 00	-3.460E-04	2.050E 01	1.290E 02
Nickel (LT 631 K)	1.170E 00	-8.600E-04	1.280E 01	1.020E 02
Nickel (GT 631 K)	5.020E-01	2.160E-04	1.280E 01	1.020E 02
304-SS	1.140E-01	1.390E-04	1.600E 01	1.290E 02
316-SS	9.090E-02	1.380E-04	1.590E 01	1.730E 02
430-SS	2.080E-01	3.720E-05	1.120E 01	4.610E 01
Incoloy 800 (LPD)	5.450E-02	1.870E-04	1.770E 01	3.480E 02
Incoloy 800 (HPD)	5.450E-02	1.870E-04	1.530E 01	8.190E 01
Inconel X	6.410E-02	1.762E-04	1.530E 01	1.510E 02
Inconel 600	8.550E-02	1.650E-04	1.530E 01	1.510E 02
Croloy	4.450E-01	-1.510E-04	9.300E 00	1.100E 01

[a]
UL = Upper limit value based on literature data indicating high permeability values.
LL = Lower limit value based on literature data indicating low permeability values.
AVG = Average of several permeation data sets.
LPD = Permeation data measured at low driving pressures (< 1 torr).
HPD = Permeation data measured at high driving pressures (> 1,torr).
GT = Greater than
LT = Less than
E ± XX = x $10^{\pm XX}$.

Table I-4. Summary of Calculated Tritium Permeation Rates vs. Temperature For Selected Materials Using the Base Case Plant Conditions Listed Below

	Reactor Thermal Power = 5000.0 MW Wall Temperature Gradient = 60.0°K Tritium Upstream Pressure = 10^{-10} Torr Tritium Downstream Pressure = 0.0 Torr			
	Permeation Rate Ci/Day			
Temperature, °K	600.0	800.0	1000.0	1200.0
Material[a]				
Vanadium (UL)	1.039E 03	1.912E 04	1.074E 05	3.335E 05
Vanadium (LL)	1.091E-02	2.374E-01	1.474E 00	4.896E 00
Niobium (AVG)	1.951E 04	3.641E 04	5.146E 04	6.346E 04
Niobium (UL)	8.366E 03	2.277E 04	4.036E 04	5.788E 04
Niobium (LL)	1.337E 00	4.320E 01	3.380E 02	1.304E 03
Molybdenum	2.901E-03	2.259E-01	3.162E 00	1.881E 01
Nickel (LT 631 K)	2.825E 00	--	--	--
Nickel (GT 631 K)	--	4.010E 01	1.886E 02	5.206E 02
304-SS	8.083E-01	2.030E 01	1.353E 02	4.664E 02
316-SS	1.340E 00	3.243E 01	2.109E 02	7.141E 02
430-SS	1.388E 01	1.407E 02	5.585E 02	1.387E 03
Incoloy 800 LPD	6.205E-01	2.074E 01	1.625E 02	6.210E 02
Incoloy 800 HPD	1.093E 00	2.209E 01	1.280E 02	3.999E 02
Inconel X	1.978E 00	4.053E 01	2.371E 02	7.462E 02
Inconel 600	1.821E 00	3.821E 01	2.275E 02	7.253E 02
Croloy	1.059E 01	8.139E 01	2.892E 02	7.031E 02

[a] UL = Upper limit value based on literature data indicating high permeation values.
LL = Lower limit value based on literature data indicating low permeation values.
AVG = Average of several permeation data sets.
LPD = Data measured at low driving pressure (< 1 Torr).
HPD = Data measured at high driving pressure (> 1 Torr).
GT = Greater than
LT = Less than
E ± XX = x $10^{\pm XX}$.

gradient = 60°K, (3) upstream tritium pressure = 10^{-10} torr, and (4) downstream tritium pressure = 0 torr. Based on the assumption[11] that tritium releases from a fusion power plant similar to the base plant should not exceed 10 Ci/day, only the molybdenum and lower limit vanadium data give acceptable permeation rates at temperatures up to 1000°K. Most of the conventional austenitic and nickel-base alloys require at least a 10-fold barrier in the 800 to 1000°K range. As was pointed out in the previous progress report,[7] increasing the effective upstream tritium pressure to say 10^{-8} torr (a more reasonably attainable value) would increase all the rates in Table I-4 by another order of magnitude.

---

[11] F. N. Flakus, "Fusion Power and the Environment," Atomic Energy Review, 13, 587 (1975).

D. Dosimetry and Damage Analysis Group

1. Service Dosimetry

R. R. Heinrich and L. R. Greenwood, Chemical Engineering Division

Dosimetry analysis for neutron flux and spectrum of a LASL irradiation of refractory ceramic material in EBR-II has recently been completed. Two dosimeter capsules each containing eleven different foil materials were positioned 4.7 cm and 11.7 cm below the reactor midplane in row 8 at a 8D4 position. The irradiation was during EBR-II Run 80B for an exposure of 2532 MWD.

Summarized in Table I-5 are the neutron fluences obtained from the dosimetry analysis for each of the reactor positions. Figure I-11 illustrates the SAND-II unfolded neutron spectrum for capsule D-2 located at 11.7 cm below reactor mid-plane. This illustrates good dosimeter foil coverage and redundancy for the entire neutron energy range of interest, namely above 10^{-4} MeV.

Table I-5. Neutron Fluence for LASL Refractory Material Irradiation in EBR-II Row 8, Run 80B

Capsule	Axial Position cm	Neutron Fluence, $n/cm^2 \times 10^{20}$		
		Total	> 0.1 MeV	> 1 MeV
D-1	- 4.7	38.7	29.4	7.86
D-2	-11.7	35.6	26.5	7.01

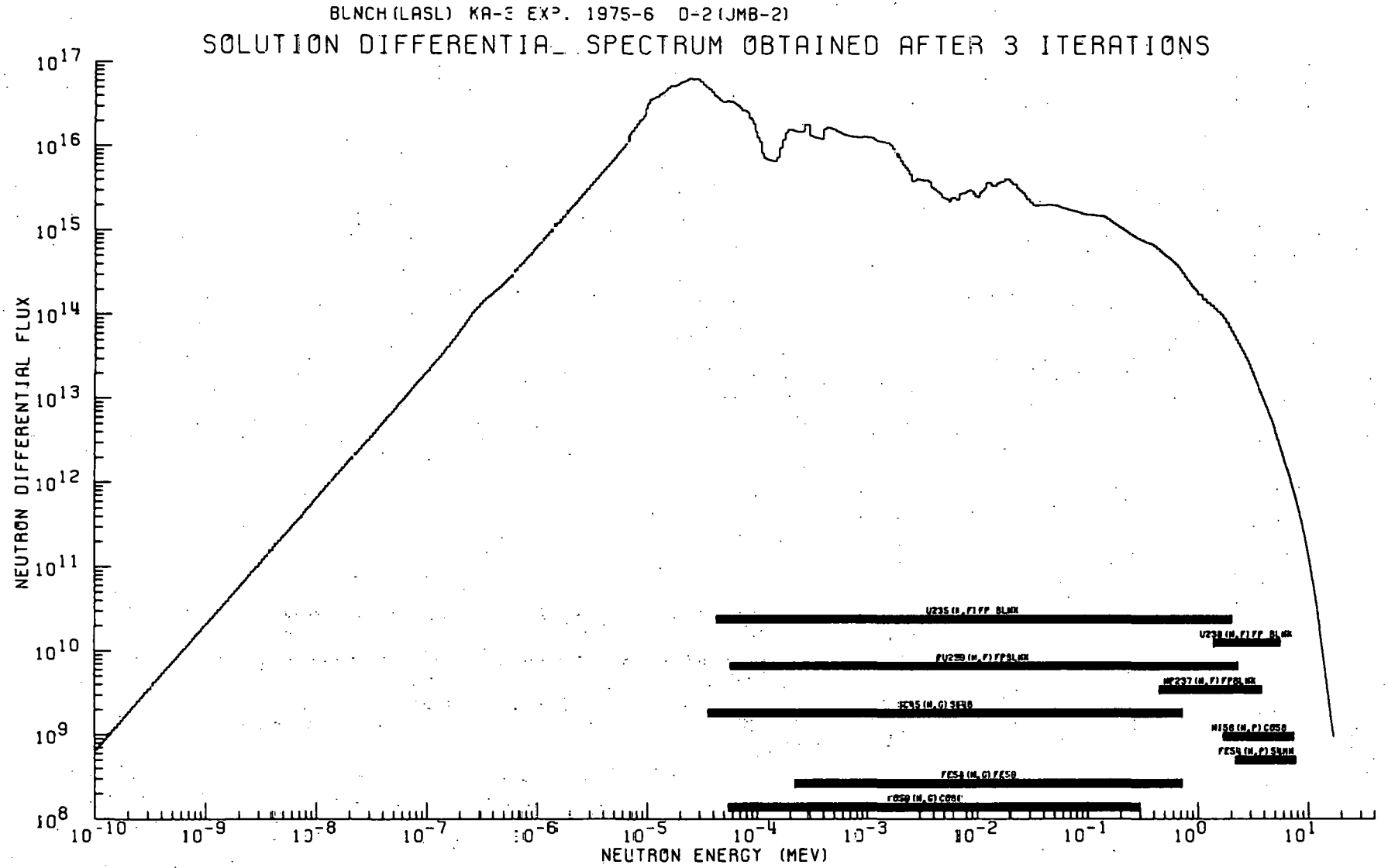

Figure I-11. Differential neutron spectrum of LASL refractory irradiation in EBR-II row 8, run 80B.

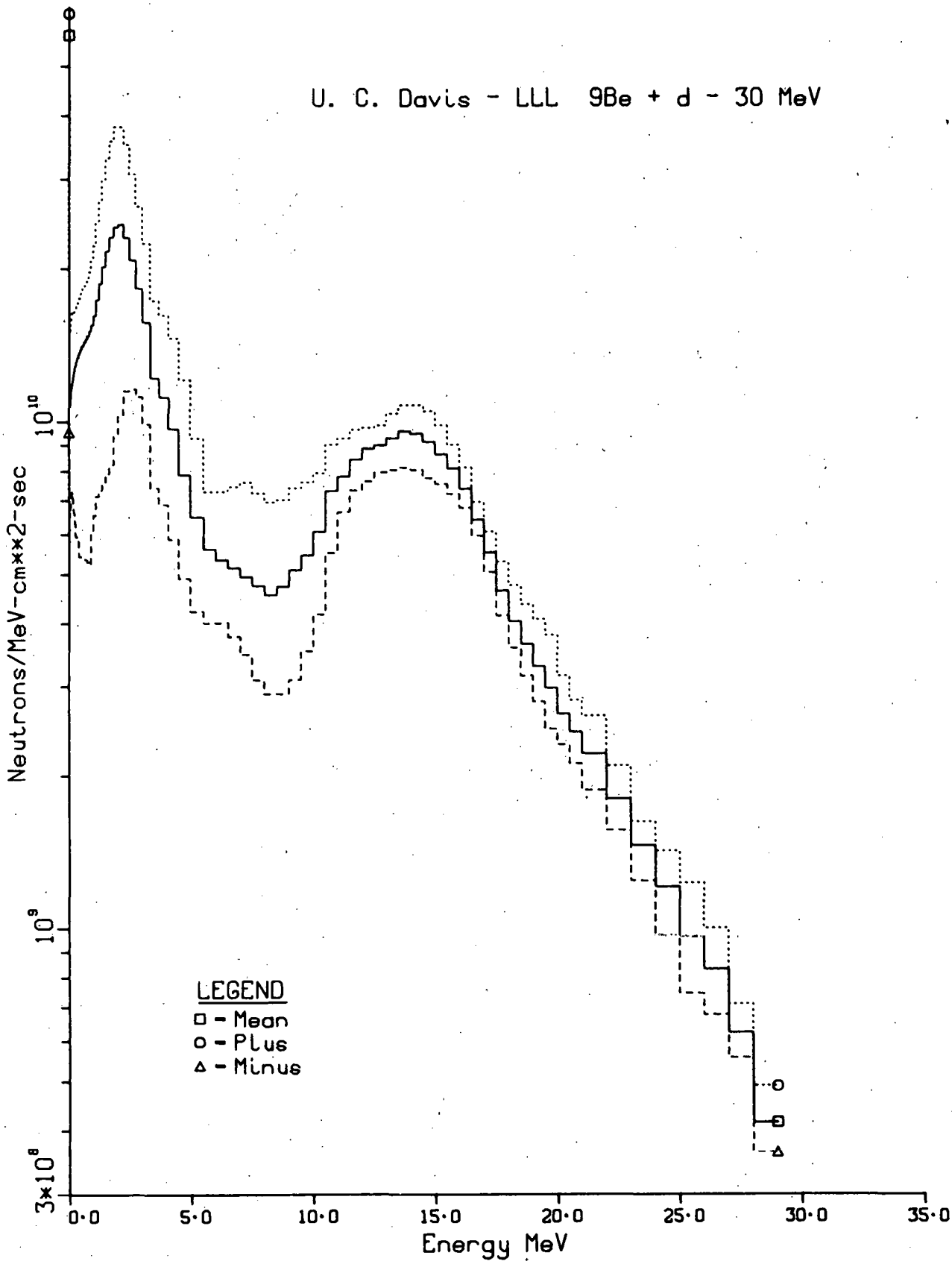

Figure I-12. Error analysis of differential neutron spectrum from 30 MeV $^{9}Be(d,n)$ irradiation at University of California - Davis.

2. Damage Analysis

L. R. Greenwood, G. R. Odette* and R. R. Heinrich, Chemical Engineering Division

A modified version of the SAND-II code which provides an error analysis of the unfolded differential neutron spectrum is now available for use. The code, SANDANL, examines by a Monte Carlo procedure the error in the unfolded spectra due to uncertainties in cross sections, foil activities, and the input trial function.

Sample output of the code is shown in Figure I-12 for a 30 MeV $^{9}Be(d,n)$ irradiation at the University of California - Davis accelerator. The solid line is the mean solution for 30 variations and the dashed lines represent the standard deviations in the unfolded flux. Whereas the absolute errors are somewhat uncertain because of unreliable cross section uncertainties, the relative errors are considered to be quite reliable. The large uncertainties at low energies are due to lack of both foil coverage and low energy input spectral data.

The use of the SANDANL code now gives us a rapid and systematic appraisal of the reliability of the unfolded neutron spectra and it is anticipated that when reliable parameter uncertainties are established, a routine error analysis will be part of the dosimetry analysis.

---

* Consultant, Department of Chemical and Nuclear Engineering, University of California, Santa Barbara, California.

E. Radiation Damage in Diagnostic Windows

J. H. Norem, Accelerator Research Facilities

A preliminary study of X-ray effects in optical windows has been completed. This study used synchrotron radiation from the 3.49 GeV electron beam in the storage ring at the Stanford Linear Accelerator Laboratory to duplicate the high energy X-ray spectra from plasma bremsstrahlung. Irradiations from 2 min to 16 hours were used to estimate the lifetime of optical windows in TFTR and EPR. Since the electron synchrotron radiation energy flux (in W/cm^2) is about 10 times the plasma bremsstrahlung flux in TFTR, which also has a low duty cycle, it was possible to roughly duplicate the lifetime dose of x-rays in optical windows on TFTR in the longer exposures. The results of the test, together with the radiation spectra, are shown in Figure II-2. The radiation damage in glass does not seem to be very stable. Bleaching with a 275 W sunlamp for 24 hours after irradiation increased the transmission in all glasses. A preliminary result of these tests is that fused quartz should maintain adequate transparency when exposed to TFTR X-ray fluxes for the lifetime of that machine. We have not been able to assess the affects of temperature, electron and ion losses to the window surface, UV and visible light and the timing of the damage and bleaching. These effects should alter the X-ray induced transmission loss.

II. EXPERIMENTAL POWER REACTOR

A. Revised EPR Design

W. Stacey, Jr., et al., EPR Project

The previous EPR designs were reviewed and a new design point was developed. This new design point is described in a separate report.[1]

---

[1] W. M. Stacey, et al., "A Revised Design for the Tokamak Experimental Power Reactor," Argonne National Laboratory, ANL/FPP/TM-77, March, 1977.

B. Power Requirements for Ignition and Beam Driven Burn

J. H. Norem, EPR Project

The power required for heating a plasma to ignition or operating a reactor in a beam driven mode can be calculated from the sum of the power required to heat the plasma at a given rate and the power required to replace losses at a given temperature and density. The required power is primarily a function of the plasma temperature and density profiles, and the confinement time of the machine for conduction losses, $\tau_E^{(cond)}$. The analysis shown in Figure II-1 can be used to roughly determine (1) the power required to heat to ignition; (2) the power required to operate in a beam driven mode; (3) the levels of "high grade" heating (capable of heating the plasma core) which would be required to heat to ignition if "low" grade heating would not be capable of penetrating to the plasma core. Increasingly high power levels are required as the assumed operating temperature and density are increased, strongly affecting the cost and complexity of beam heating systems for driven reactors or high grade heating (such as high energy neutral beams $E \sim 500$ keV). The results presented refer to flat profiles. Profile effects are the largest uncertainty.

C. EPR Magnet Systems

L. R. Turner and S-T. Wang, EPR Project

1. Toroidal Field Coils

As part of the revised EPR design, the toroidal field (TF) coils were redesigned. The reduced peak field (9 T) and major radius (5 m) of the 1977 EPR plus the increased allowable strain on the conductor (0.2%) permit a smaller, thinner coil. Relative to the 1976 design, the amount of copper stabilizer is reduced 66%, the amount of stainless steel support is reduced 90%, and the stored energy is reduced 62%. Because the 1976 coils were designed to operate at 3.0 K and the 1977 at 4.2 K, the amount of superconductor is increased 41%.

$$P_{Req} = P_{(increase\ T)} + P_{(losses)}(T, \tau_E(cond))$$

$$P_{(losses)} \approx P_{Brems}(T) + \frac{E_{thermal}}{\tau_E(cond)} - P_{\alpha}(T,n)$$

$$P_{(increase\ T)} = \frac{3}{2}\int n\left(\frac{dT_e}{dt} + \frac{dT_i}{dt}\right)d^3x$$

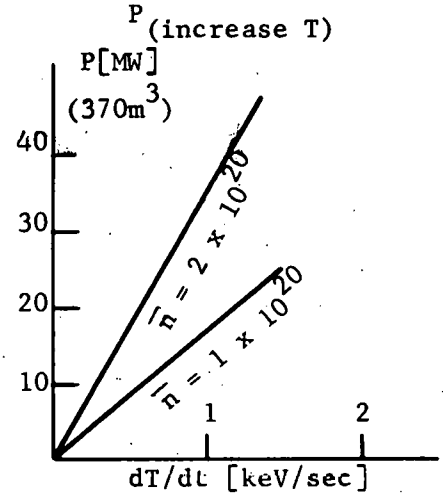

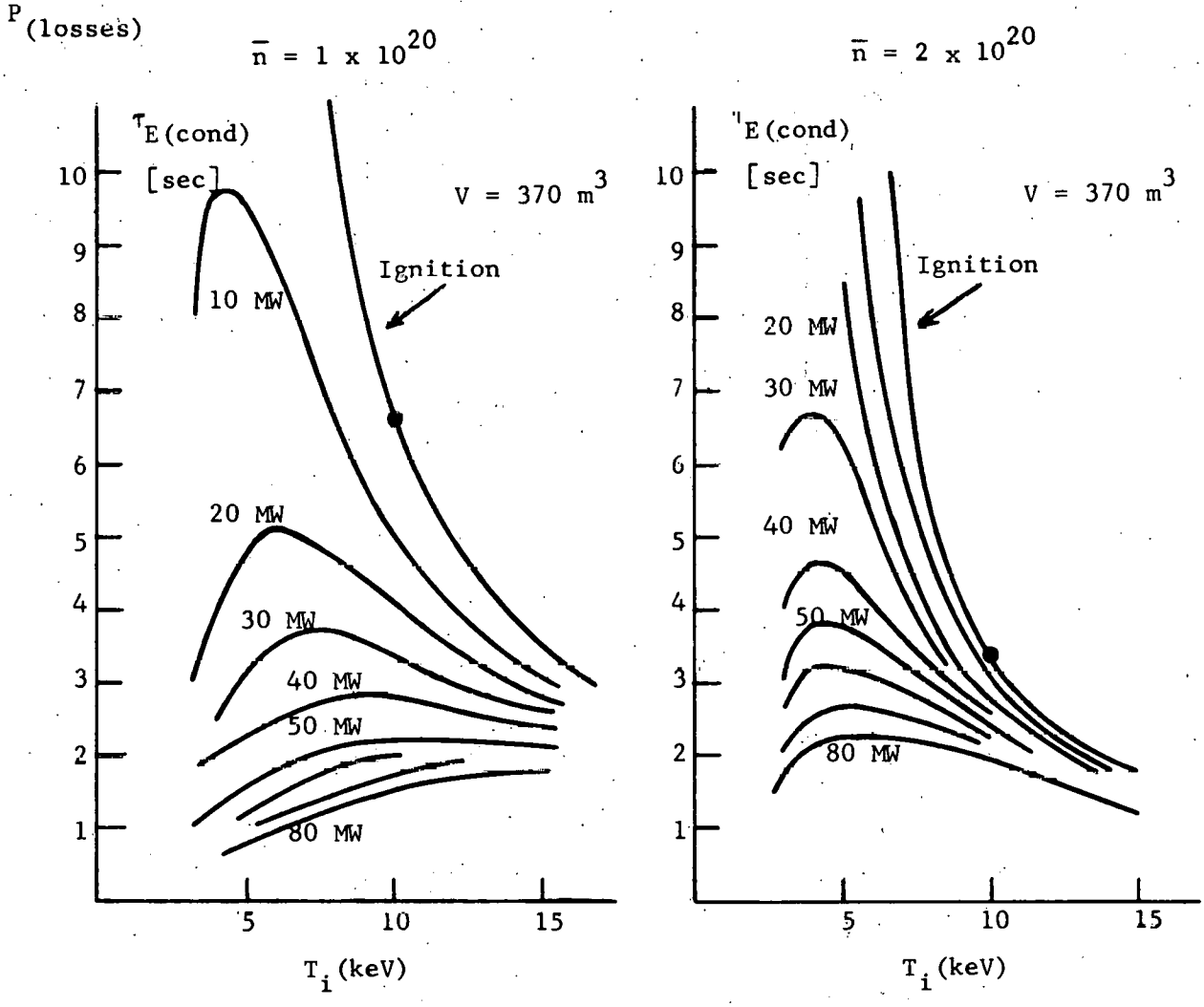

Figure II-1. Power Requirements as a Function of Heating Rates and Losses

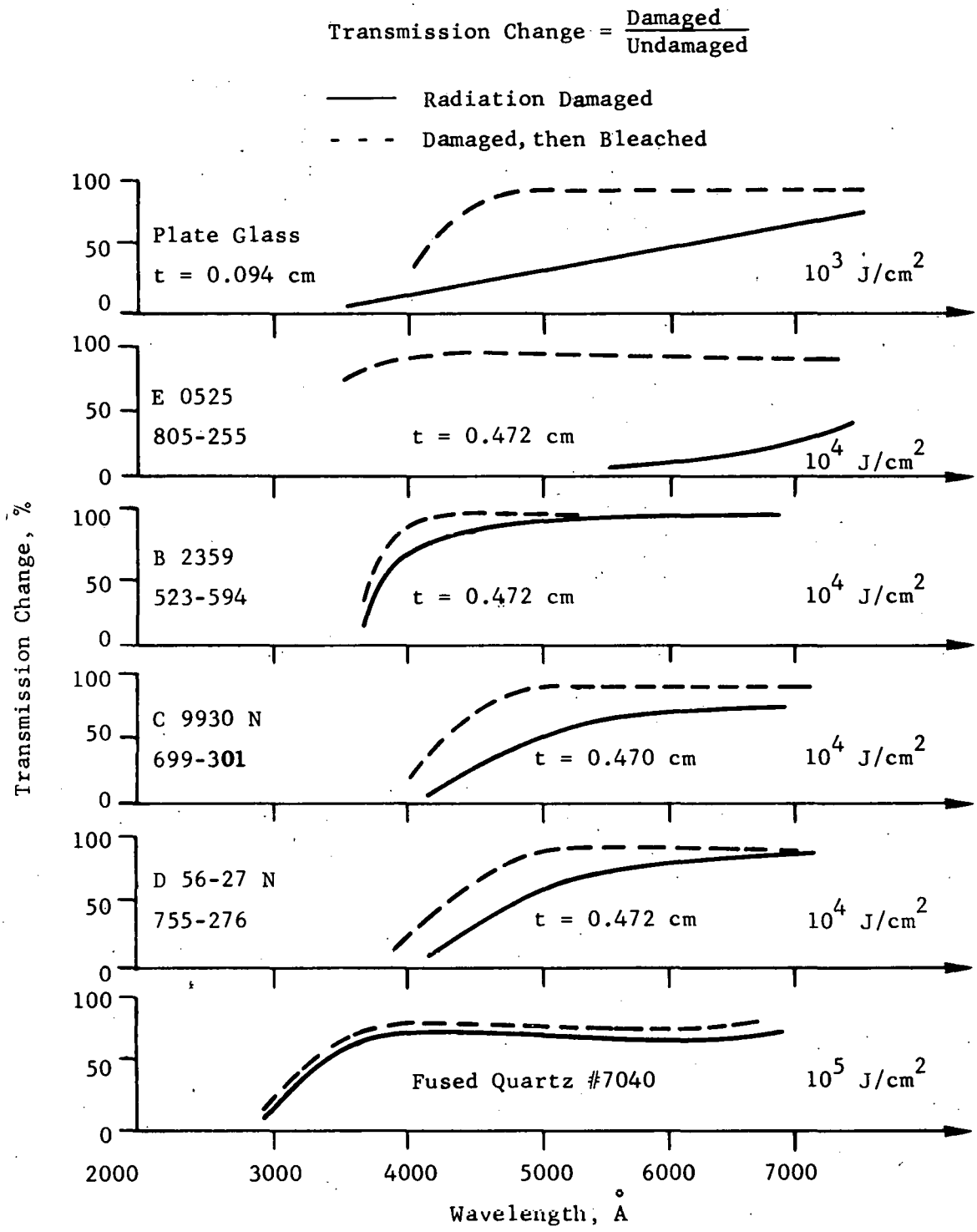

Figure II-2. Radiation Damage in Quartz and Various Glasses due to X Radiation.

2. Ohmic Heating Coils

The ohmic heating coils were also redesigned. A central solenoid plus ten other coils provide up to 55 V-s, but with a low field over the region of the plasma ($< 10^{-3}$ T) and TF coil (< 0.1 T).

3. Protecting the OH and EF Coils and Power Supplies from a Plasma Current Quench

In the event of a sudden plasma current quench, the plasma current can be transferred inductively to a suitably designed first wall. Afterwards, the current in the first wall will decay slowly, and the OH and EF system will be undamaged. This study is described in more detail in the safety section of this report.

D. Vacuum Systems

J. Moenich, EPR Project

There is a possibility that the expected neutron flux in the neutral beam injectors may result in prohibitively high thermal loading on cryopumping panels.

Zirconium-aluminum getter is another mode of pumping which shows promise for pumping the neutral beam injectors. It develops high pumping speeds for active gases and especially for H_2. The getter panels provide a well defined trapping volume of the gas which is important in handling tritium and they can be located as near the gas source as possible. Operating experience with a zirconium-aluminum pump in the vicinity of a fission-reactor core for 3 years[2] shows satisfactory operation in neutron flux densities greater than expected in the vicinity of the neutral beams. Furthermore, thermal loading should have no adverse effects on performance since zirconium-aluminum pumps are normally run at temperatures of the order of 400°C to maintain active and efficient pumping surfaces in the presence of contaminants. Their disadvantages include the inability to desorb the active gases other than hydrogen when reactivated; extremely low pumping capacity for methane; and inability to pump the inert gases.

---

[2] R. Dobrozemsky, "Operating Experience with an UHV System in the Vicinity of Fission-Reactor Core," J. Vac. Sci. Technol., Vol. 13, No. 1, January, 1976.

In Table II-1 below is given some comparative data per injector for the cryo and zirconium-aluminum pumping panel options under an EPR duty factor of 0.80 and plant factor of 0.5. Lifetime, regeneration and reactivation are based on a 5 second injection period during each cycle.

Table II-1. Neutral Beam Pumping Requirements per Injector

	Chamber I	Chamber II
Gas Load (Tℓ/s)	49.4	11.9
Required Pumping Speed (ℓ/s)	2×10^6	2×10^6
Pumping Panel Area for D_2 (M^2)		
cryopanel area	40	40
Zr-Al panel area	30	30
Regeneration (30°K) or Reactivation (973°K) frequency (days)		
cryo regeneration	6	24.9
Zr-Al reactivation ($P_{eq} - 1 \times 10^{-5}$)	9	
Zr-Al reactivation ($P_{eq} - 5 \times 10^{-6}$)		24.9
Panel Lifetime		
cryopanel	Life of Reactor	
Zr-Al panel (yrs)		
1% O_2 contamination	4.52	18.6
1% Co, N_2 contamination	0.90	3.72

The lifetime of the zirconium-aluminum panels is given in terms of either O_2 contamination or CO, N_2 contamination. The gas load will most probably contain a combination of these contaminants and lifetime will fall somewhere between the two limits.

The periodic regeneration (cryo) or reactivation (Zr-Al) of pumping panels would interrupt neutral beam operation. One way to avoid this would be to double the required amount of pumping panel and provide a means for isolating each half in turn when regeneration or reactivation is necessary. The problem of providing reasonably vacuum tight valving to isolate hundreds of meters of pumping panels appears staggering both in cost and complexity. If space is available, a very promising solution would be to provide one or two more injectors than is necessary. The spare injectors provide the means for rotating each injector in turn through the regeneration or reactivation phase and thus eliminate the need for double paneling and panel isolation. Placing this required activity on a rotational basis will also minimize the pumping requirements, both in hardware and capacity, and the additional injectors will provide redundancy for online failures during an experiment.

E. Thermal Hydraulic Analyses

B. Misra, Chemical Engineering Division

This section describes recent progress in studies that are presently underway to evaluate the thermal hydraulic performance of the ANL/EPR first wall/blanket/shield region. The current design concept for the ANL/EPR blanket system involves an assembly of modular stainless steel blocks with gun-bored cooling channels. The thermal hydraulic analyses presented below are based on a single modular block that is 28-cm-thick and 1.5 m in length in the plane parallel to the first wall. (The dimension in the poloidal direction is immaterial to the present analytical model for thermal hydraulic performance.) Cooling with either pressurized water or steam flowing in the channels parallel to the first wall has been considered. To simplify the geometric model (see Figure II-3), inline coolant channels with graded cross-sectional areas have been selected for initial analysis, recognizing that a more staggered arrangement would probably be eventually selected in order to reduce the total number of channels required per block.

A section of the blanket block shown in Figure II-3 (X = 0.28 m, Y = 0.05 m and Z = 1.5 m) was divided into 380 nodes with 6 coolant channels as indicated in the figure. The inlet temperatures of the coolants were assumed to be 240°C (464°F) for water and 260°C (500°F) for steam. The selection of these temperatures is based on assumptions that the operating pressures for water and steam are, respectively, 2200 and 700 psia. In addition, it was assumed that the maximum temperature at any node must not exceed 550°C for stainless steel.

An existing computer code (THT-B) was selected for the thermal analysis. THT-B is a three-dimensional time dependent code which solves the heat transfer equations by a finite difference method based on an assumed initial (time = 0) temperature distribution. It takes into account the dependencies of the physical, thermodynamic and heat transport related properties of the structural materials and coolants as well as the coolant inlet temperature and the heat

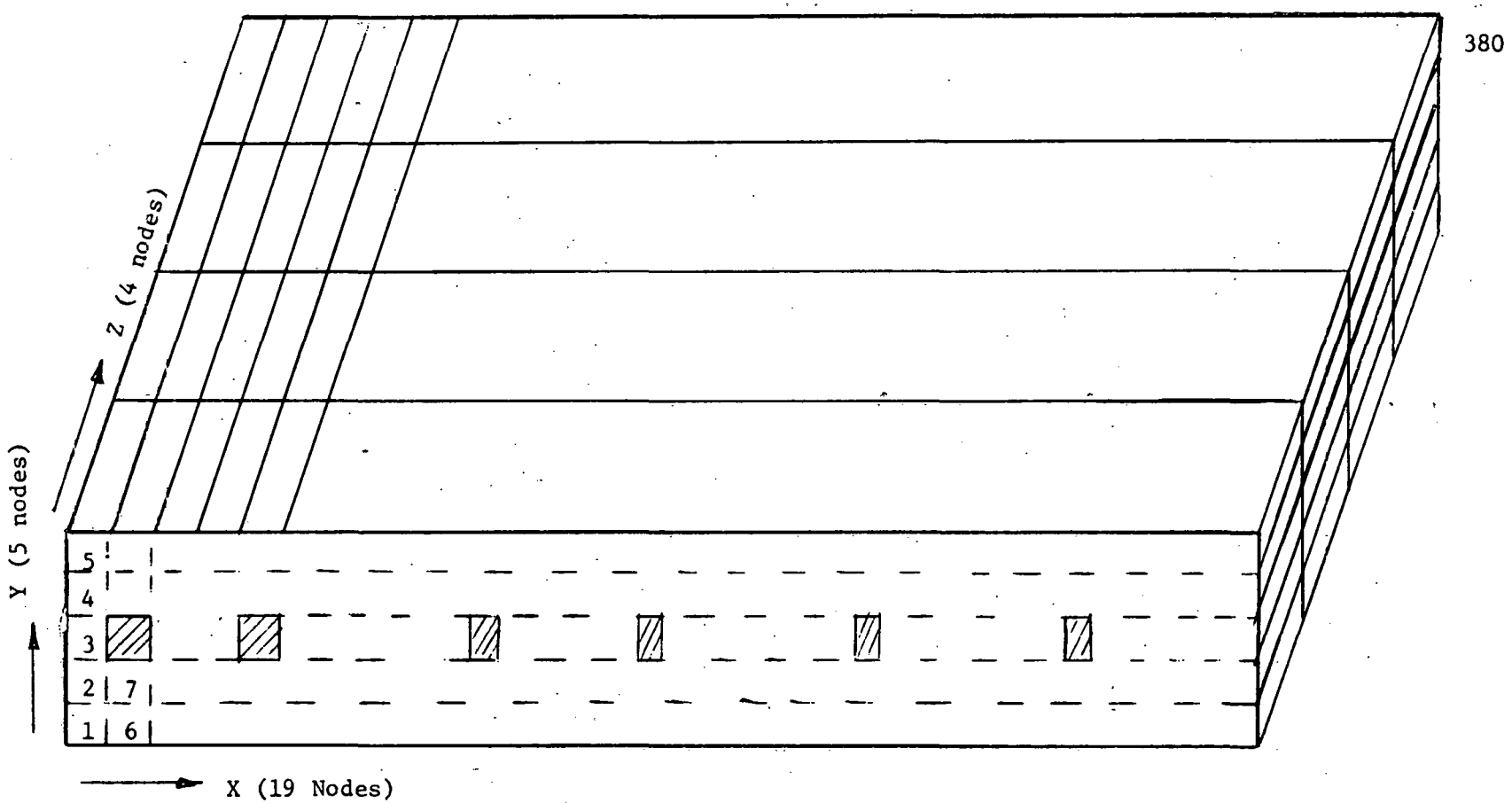

Figure II-3. Schematic of a blanket section showing coolant channel and node designations.

transfer coefficient associated with the chosen channel geometry. Figure II-4 shows the EPR-type power profile that was used in the thermal analyses. The transient temperature for a typical solid node (Node No. 315) and a typical coolant node (Node No. 293) during the reference burn cycle are plotted in Figure II-5. The coolant temperatures corresponding to the exit nodes (Nodes 293, 308, 323, 338, 353, and 363 from left to right in Figure II-3) for the six channels are summarized in Table II-2. Because of the rather large thermal inertia of the blanket block, many ($\sim$ 20) burn cycles are required before a quasi steady state is reached. For the same reason, the coolant outlet temperatures from each node do not attain their maximum temperature at the same time (see Table II-2). The results in Figure II-5 for pressurized water and steam are based on the same coolant channel geometry. The higher material temperatures for the steam system are due in part to the higher coolant inlet temperature (260°C for steam versus 240°C for pressurized water) and in part to the lower heat transfer coefficient associated with steam cooling. The temperature difference between the coolant and the blanket is higher with steam cooling for the same reasons. Because of the relatively short passage lengths used in these analyses, the estimated pressure drop across the coolant channels is less than 1 psi.

The results of these analyses indicate that a typical EPR-type blanket block could be adequately cooled with either pressurized water or steam. Studies are in progress to determine the implications of these results in terms of overall thermodynamic efficiency achievable with alternate coolants (pressurized water, steam, helium and others).

Table II-2. Coolant Node Temperatures as a Function of Location and Time for the Reference Burn Cycle, Using Pressurized Water and Steam

	Node Temperatures, °C			
	Time[c] = 1100 s		Time[c] = 1200 s	
Node Number	Water	Steam	Water	Steam
293[a]	327	357	314	342
308	331	359	322	349
323	342	364	336	358
338	340	372	337	370
353	336	358	335	358
368[b]	342	342	344	344

[a] Cooling channel nearest first wall

[b] Cooling channel nearest outer surface of blanket

[c] Time after start of repetitive burn cycles -- cycle time equals 65 seconds.

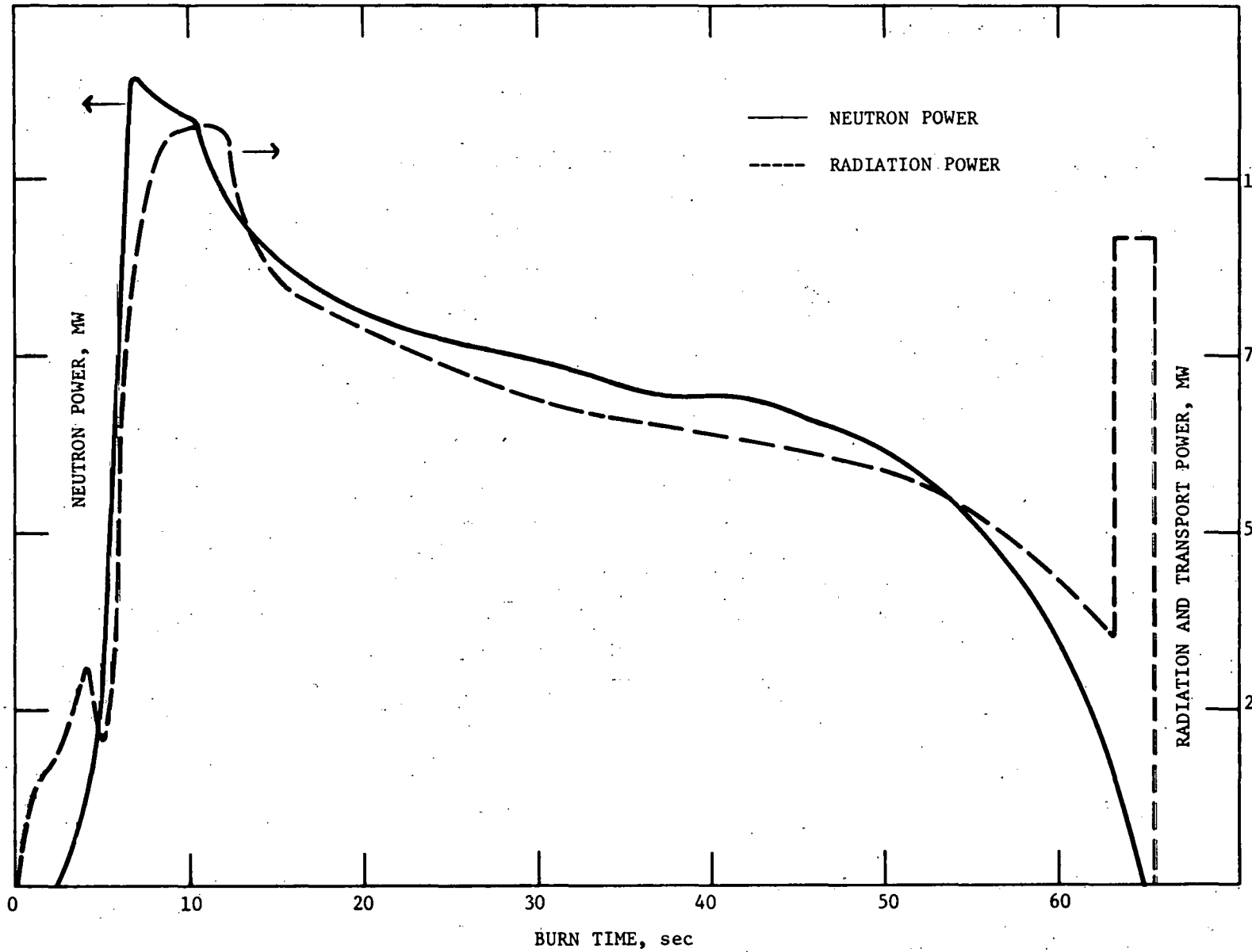

Figure II-4. Neutron and Radiation Power During a Typical Burn Cycle.

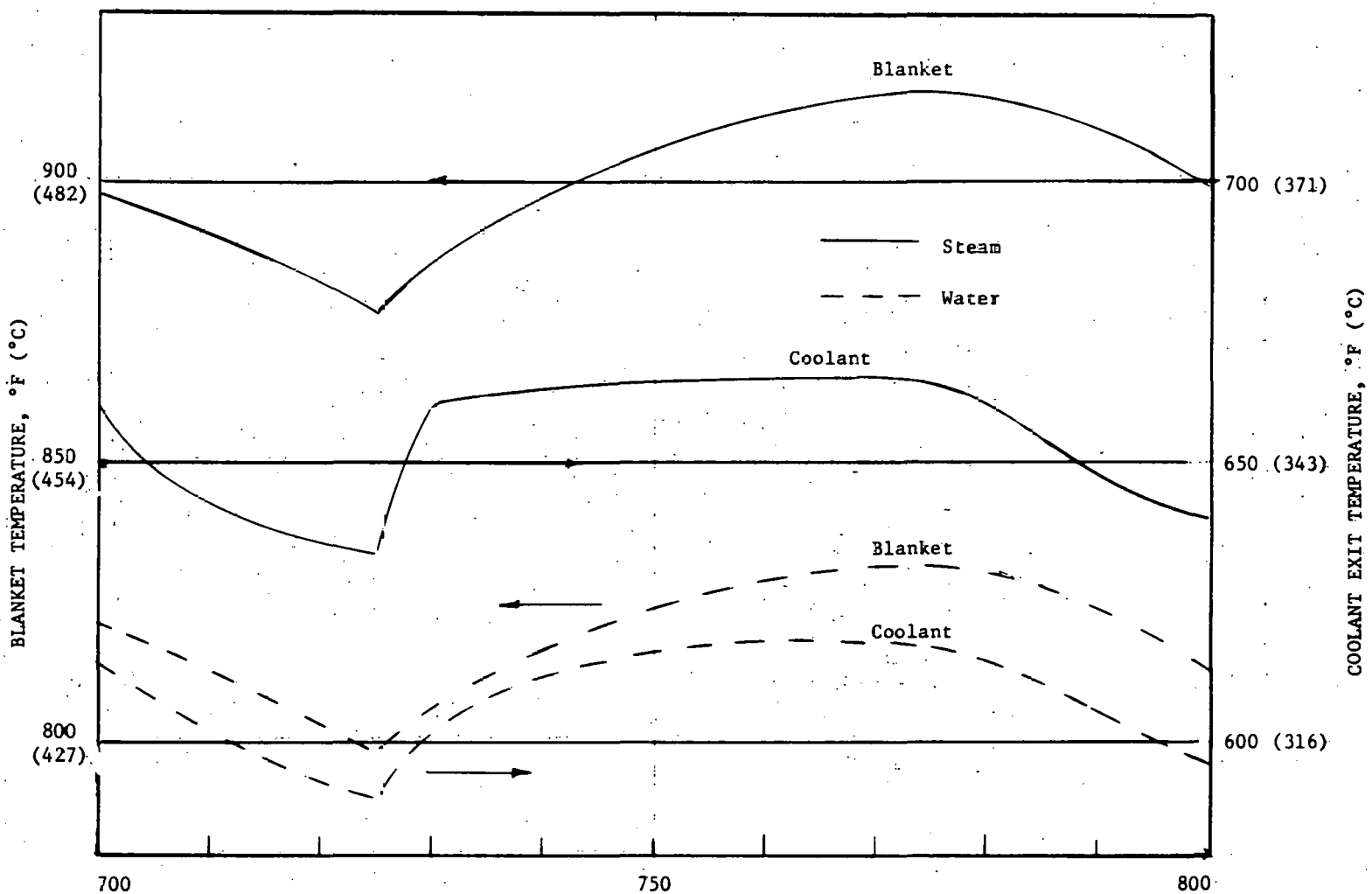

Figure II-5. Variation of Blanket and coolant temperature during a burn cycle.

III. TNS PROJECT

A. OH Magnet Coil System

K. Thompson, TNS Project

In the design of the OH coil for the TNS magnet system under study through a collaborative effort between ANL and General Atomics, it has become desirable to develop a coil which has 20 effective turns. Since about 56 x 10^6 ampere turns are required for this coil, it is necessary to divide the coil into a number of 20 turn sections and connect these electrically in parallel. The present proposed geometry consists of 56 such coils.

Unless the impedances of all of these coils are matched, which is very difficult to achieve, there will be unequal currents flowing in these coils during that part of the excitation pulse when the current is changing. The problem then is to determine what these currents are.

To calculate these currents a computer code was developed. This code, INDUCT-S, is based on a calculation of self and mutual inductances for thin solenoid coils. This is used to determine the self inductance of each coil and the mutual inductances between each coil and every other coil in the entire geometry. These calculated inductances are then used to establish a set of equations, one for each coil in the parallel connected circuit. The simultaneous solution of this set of equations is then used to establish the ampere turns in each coil.

During the application of this code, it became apparent that it would be useful to allow for series connected groups of coils that could be connected in parallel with the remaining coils. This provision has now been successfully implemented.

B. Neutral Beam Injectors

J. Fasolo, TNS Project

Using data provided by GA on fringe magnetic fields due to toroidal field coils, a preliminary layout of a beam line has been made. A diverging beam will be extracted from a convex plasma sheath and accelerated to an energy of 150 keV. A double-focussing bending magnet between the source and the neutralizer will remove molecular ions from the beam entering the neutralizer. The neutralizer entrance will be a distance S = 0.3 m from the exit face of the bending magnet; the neutralizer exit will be at S = 4.3 m. If the distance from the exit face of the magnet to the first wall is S = 10.7 m, the field at the neutralizer exit will be 0.102 T. Increasing this distance to 11.0 m reduces the field at the neutralizer exit to 0.067 T. In either case, the field at the neutralizer entrance due to the toroidal field coils will be of the order of 10 G.

Beam transport calculations for D^+ and for D^o derived from D^+ have been done for 50 MW of 150 keV D^o from 24 sources for various values of the double-focussing magnet bending angle θ. For a convex plasma sheath and an accelerator exit-grid radius of curvature of R = 2.225 m, the beam size at the first wall is a minimum for $\theta = 72°$.

For $\theta = 72°$, a rectangular beam with a cross section of 0.402 m x 0.012 m at the source exit grid has a cross section of 0.296 m x 0.322 m at 10.7 m, 0.304 m x 0.330 m at S = 11.0 m and 0.334 m x 0.360 m at S = 12 m. The variation of beam size with θ is shown in Table III-1.

Table III-1. Beam Size at S = 11.0 m vs θ

θ (deg)	56.6	60	65	72	77	85	90
Horizontal Beam Size (m)	0.666	0.552	0.406	0.304	0.360	0.582	0.750
Vertical Beam Size (m)	0.362	0.350	0.336	0.330	0.336	0.356	0.376

There is a trade-off, not apparent from the data presented here, between beam size at the first wall and neutralizer gas load, which is substantially larger for $\theta = 72°$ than it is for $\theta = 90°$. It is obvious from Table III-1 that for a D^+ bending angle of 72° there is no advantage to limiting the initial vertical beam size to 0.012 m, insofar as beam size at the first wall is concerned.

The transverse emittances used to calculate the beam sizes shown in Table III-1 were assumed to be given by expressions of the form ε = phase space area/$\pi = W_o\omega_o$, where W_o is the initial horizontal or vertical beam half width and ω_o is the maximum initial beamlet half-angle divergence; the expression is correct if the phase space area is bounded by an ellipse. More recently, beam transport calculations have been done for a drifting beam expanding from a waist at the source exit, a simple case in which the size of the drifting beam can be calculated from geometrical considerations and the result compared with the size obtained from the transport equations. The comparison shows that the phase space area is bounded by a rectangle or a parallelogram rather than an ellipse. The correct expression for the emittance is thus given by $\varepsilon = 4/\pi\ W_o\omega_o$.

Beam transport, power flow and gas flow calculations have been done for two 60 MW, 150 keV neutral injector systems. In the first system (the reference design) there are 6 injectors, with 2 beam lines per injector (one of each lobe of the doublet). In the second, 12 injectors and 24 beam lines are used. Total gas flow per injector is $\sim$ 250 torr·ℓ/s for 6 injectors and $\sim$ 100 torr·ℓ/s for 12. The disadvantage of the higher gas load for 6 injectors is offset by several advantages, including a higher beam power density at the first wall and the possibility of adding more injectors to increase the neutral beam power. If the extra injectors are not used to increase the total beam power, they can be used to provide beam while other injectors are shut down for regeneration of cryopanels.

C. Vacuum Systems

J. Moenich, TNS Project

No matter which mode of pumping, cryo or zirconium-aluminum, will be used for the neutral beams, operating efficiency will depend on a design to minimize down time.

Periodically, the pumping panels must be regenerated (cryo) or reactivated (Zr-Al). One way to do this without interrupting neutral beam operation, would be to double the required amount of pumping panel and provide a means for isolating each half in turn when regeneration or reactivation is necessary. The problem of providing reasonably vacuum tight valving to isolate hundreds of meters of pumping panels appears staggering both in cost and complexity. If space is available, a very promising solution would be to provide one or two more injectors than is necessary. The spare injectors provide the means for rotating the injectors through the regeneration or reactivation phase and eliminate the need for double paneling and panel isolation. Regeneration and reactivation on a rotational basis will also minimize the pumping requirements, both in hardware and capacity for this activity and the additional injectors will provide redundancy when one on line fails during an experiment.

In Table III-2 below is given some comparative data per injector for the two different pumping panel options under a TNS duty factor of 0.10. Lifetime, regeneration and reactivations are based on a 4 second injection period during each cycle.

The lifetime of the zirconium-aluminum panels is given in terms of either O_2 contamination or CO, N_2 contamination. The gas load will most probably contain a combination of these contaminants and lifetime will fall somewhere between the two limits.

Regeneration or reactivation of panels will be more often than required, due to safety or inventory requirements. The figures given however, show the minimum requirement and thus the flexibility available for the injector rotation mode for handling this necessary activity.

As duty factor increases, the lifetime of the zirconium-aluminum panels drops rapidly. For a 50% duty factor for instance, lifetime for acceptance of CO and N_2 contamination could reduce to $\sim$ six months. If, however, thermal loading of cryopanels would prohibit their use, lifetime of zirconium-aluminum pumping for D_2 may be extended by increasing panel area and providing ports for appendage pumps to exhaust the contaminants when they are no longer absorbed by the zirconium-aluminum panels.

D. RF Heating

A. Moretti, TNS Project

Lower-hybrid (LH) and Ion Cyclotron Resonance Heating (ICRH) systems have been under study for supplying 60 MW of supplementary heating to the plasma. A "Grill", a phased array of waveguides has been selected as the launcher for LH heating and a single-ridged waveguide as the launcher ICRH.

Table III-2. TNS Neutral Beam Pumping Requirements per Injector

	6 Injector Design	12 Injector Design
Chamber I		
Gas Load (Tℓ/s)	181.0	75.3
Required Pumping Speed (ℓ/s)	4.30×10^6	2.25×10^6
Pumping Panel Area for D_2 (M^2)		
cryopanel area	86	45
zirconium-aluminum area	64.5	34
Regeneration or Reactivation frequency (days)		
cryo regeneration	16.5	20.0
Zr-Al reactivation ($P_{eq} - 1 \times 10^5$)	43.5	72.6
Panel Lifetime		
cryopanel	Life of Reactor	
Zr-Al panel (yrs)		
1% O_2 contamination	10.9	18.3
1% CO, N_2 contamination	2.2	3.6
Chamber II		
Gas Load (Tℓ/s)	71	31
Required Pumping Speed (ℓ/s)	4.35×10^6	3.15×10^6
Pumping Panel Area for D_2 (M^2)		
cryopanel area	87	63
zirconium-aluminum area	65.3	47.3
Regeneration or Reactivation frequency (days)		
cryo regeneration	42.5	70.5
Zr-Al reactivation ($P_{eq} - 1 \times 10^5$)	63.9	106
Panel Lifetime		
cryopanel	Life of Reactor	
Zr-Al panel (yrs)		
1% O_2 contamination	16.1	26.5
1% CO, N_2 contamination	3.2	5.3

The "Grill" structure selected as the launcher for LH heating in TNS is shown in Figure III-1. It consists of 40 narrow-height WR-430 waveguides forming a rectangular array, 4 waveguides high and 10 waveguides wide. The narrow dimension of the guide, the E-field direction, is parallel to the toroidal magnetic field direction. The array is 0.437-m high by 0.223-m wide. As it leaves the shield area it makes a right-angle bend upward. In order to reduce the probability of electrical breakdown and reduce the cost of the feed waveguide system, a ceramic (Al_2O_3, BeO or some other radiation-hardened material) dielectric window is placed above the bend as shown in Figure III-1. In addition, a dc break, as shown, is required in the feed waveguide either before or after the window to prevent possible ground loops and protection of personnel and equipment from possible ground faults. Not shown and to be incorporated in the design is a mechanism composed of flexible waveguide and bellows for adjusting the position of the face of the "Grill" with respect to plasma and a vacuum pumping system between the window and the face of the "Grill" to achieve a safe pressure of 10^{-6} torr at turn-on of the rf.

The single ridged waveguide, Figure III-2, has been selected as the primary launcher for ICRH in TNS. The use of ridged waveguide offers the possibility of mounting the launcher flush with the first wall with all the attendant advantages of not having any part of the launcher between the first wall and the plasma edge. The questions still to be addressed both theoretically and experimentally are the coupling of the launcher to the plasma and the mode structure for optimum coupling and heating. Therefore, alternates to the ridged guides, such as the dielectric loaded ridged guide with all its attendant radiation problems and loops, are under study.

E. Tritium Facility Design Analysis

J. M. Mintz,* R. G. Clemmer, J. Davis, B. Misra and V. A. Maroni,
TNS Project

Work on the design of the tritium handling facility for TNS, TNS-upgrade (initial operating scenario) and TNS-upgrade has continued. The computer code (TCODE) developed to compute tritium facility parameters has been used to conduct a wide range of trade-off studies on the differences between the TNS and the upgraded versions. The key results of these studies are summarized in Table III-3. Major differences in design requirements are found in the parameters associated with duct diameter, required pump capacity, required effective duct speed, and tritium throughput. A study of the impurities anticipated in the plasma exhaust has been completed, with the finding that carbon (probably in the form of low molecular weight hydrocarbons) could be a major exhaust impurity (possibly as high as one atom %) if carbon or silicon carbide are used as liner or limiter materials. The need and optimum location for a debris separator in the vicinity of the torus evacuation system is being investigated.

---

* Visiting scientist from General Atomic Company.

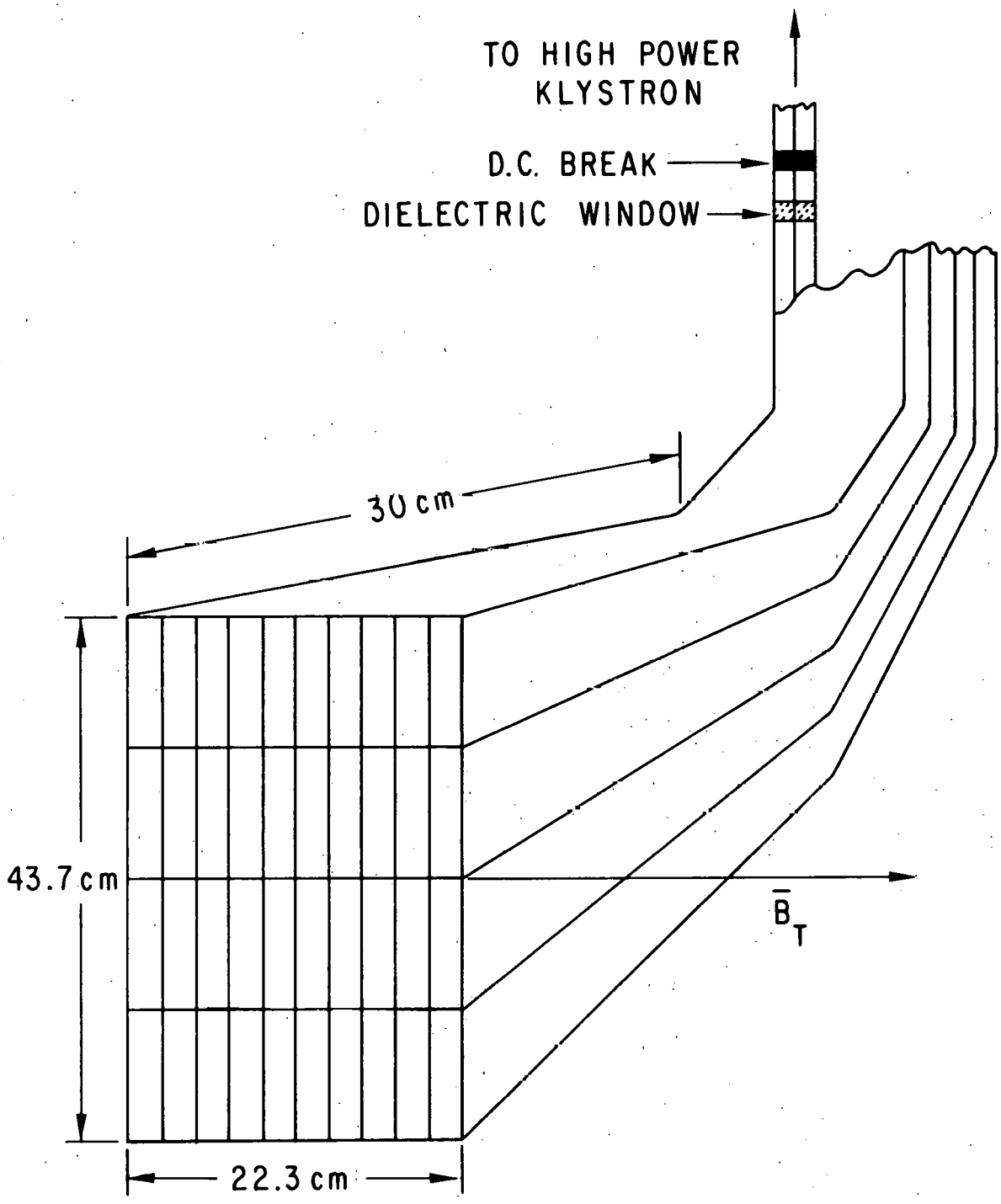

Figure III-1. The Grill Launcher for LH Heating

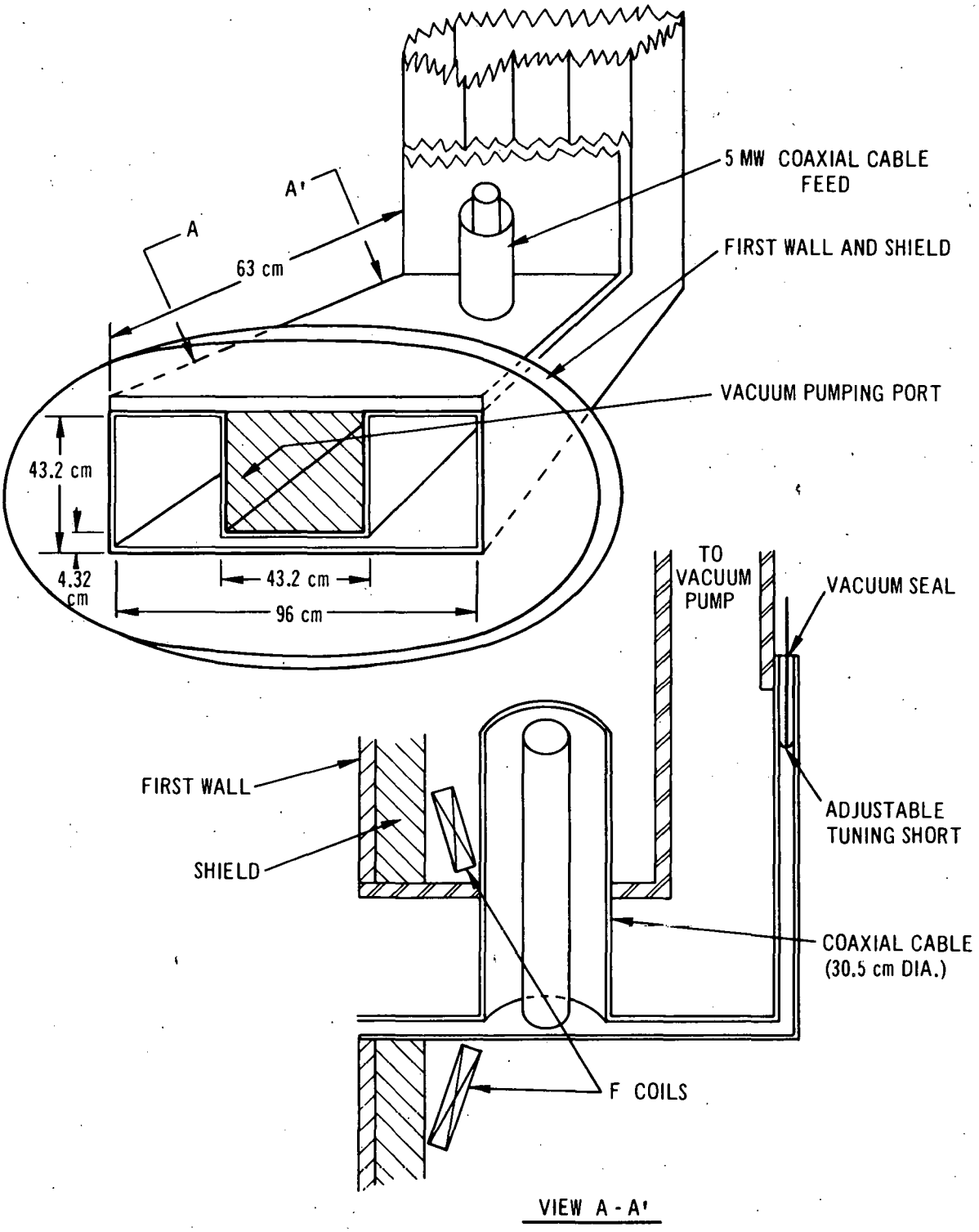

Figure III-2. The Single Ridged Waveguide Launcher for ICRH.

Table III-3. Comparative Analysis of Vacuum/Plasma Interface Parameters for TNS and TNS-Upgrade

Parameter	TNS-ITR η = 0.1	TNS-Upgrade (initial) η = 0.1	TNS-Upgrade η = 0.5	TNS-Upgrade η = 0.75	TNS-UG (R = 0.75) TNS-ITR
Burntime, s	30	30	90	90	3
Dwell time, s	270	270	90	30	0.11
Fractional burnup, %	9.8	10.6	17.3	17.3	1.8
Cycle Avg. Power, MW	29	40	200	300	10
Tritium Burnup/hr, g	0.2	0.3	1.3	1.9	9.5
Tritium Input/hr, g	1.9	2.4	7.3	11.0	5.8
Tritium Exhaust/hr, g	1.7	2.1	6.0	9.1	5.3
Post burn gas temp., °C	100	100	400	400	4
Post burn pressure, torr	3.5×10^{-3}	3.5×10^{-3}	1.1×10^{-2}	1.1×10^{-2}	3.1
Speed required at torus, ℓ/s	6160	7910	29,700	89,100	14
Number of active ducts	2 3	1 2	12	12	4-6
Pump speed, ℓ/s/duct	10^4-3.5×10^3	6.2×10^4-10^4	25,000	62,000	6.2 - 18
Duct Diameter, cm	45	70	70	70	1.6
Pump Tritium Inventory, g					
turbo	0	--	--	--	--
cryo	4.0	5.1	14	21	5.2

Three options for the torus evacuation system employing various types of cryo-based pumps and turbomolecular pumps are being evaluated. Results to date indicate that turbopumps might suffice for the TNS, but the upgraded versions of TNS will more than likely require cryo-based pumps. Intermediate (transition region) compression of the fuel from pressures in the range 10^{-2} to 10^{-3} torr up to pressures around 1 to 10 torr has been identified as a major research and development item. A fluidless, fully weld sealed, high speed pump would be desirable. Options for this transition pumping operation (or for ways of circumventing it) are under study. Two concepts for non-metallic element impurity removal -- one based on hot rare earth/refractory metal gettering and the other based on cryochemical separations (i.e. of the type presently under study by the LASL/TSTA team) -- are being analyzed. The gettering method appears to be less complex and potentially more flexible in terms of broad spectrum impurity removal but has the disadvantages of generating upwards of 0.1 m^3 of solid low-level tritiated waste per year. The cryo-chemical method seems to be inherently complicated and unexpected impurity species could plug up the column or create other operational problems if the system is not carefully designed. It does, however, result in only small amounts of dischargeable gaseous waste (mostly CO and N_2). The removal of helium and any argon (or other inert gases) in the fuel stream will be done by a set of cryogenic stripping columns that are presently under design.

A four column cryogenic distillation cascade scenario is being developed for the enrichment step. The feeds to the cascade include: (1) the main fuel recycle stream (2 to 10% protium with the remainder deuterium and tritium); (2) the neutral injector recycle stream ($\sim$ 98% D, $\sim$ 1% T, and $\sim$ 1% H), and (3) high level tritium-containing strippings from secondary cleanup systems. The outputs of the cascade are: (1) a protium-free fuel stream with T/D > 1.5; (2) an HD with negligible tritium content; and (3) a 99 + % D stream for the neutral injector feed. Results of a sensitivity study involving reflux ratio, column operating pressure, and a number of theoretical stages has resulted in a preliminary design point of 100 stages, 1000 torr, and a reflux ratio of 15 for the first column. This column gives a bottom product with T/D $\simeq$ 2.25 and H < 10^{-5} atm %. Additional studies (see Table III-4) have shown that this column could take up to 10 atm % H in the feed stream without significant change in the bottom product. Such a capability allows use of the system for tritium extraction from waste water. A dynamic column model is being developed to analyze transient effects on column operation.

In other areas of study, the nature and magnitude of source terms from protium to the fuel cycle and for tritium leakage from the fuel cycle have been examined. The rates of tritium and protium buildup in the neutral injector recycle are estimated at 0.15 and 0.05 atm %/day, respectively. It appears that pressurized water-cooled, first-wall designs operating at > 300°C will necessitate an $\sim$ 100-X permeation barrier on the first wall surface to hold protium insertion to the plasma chamber at acceptable levels. Other source terms for protium (e.g., leakage, outgassing, (n,p) reactions, D-D fusion) appear to be tolerable. Tritium permeation to the first-wall coolant should present no unmanageable problems, even if the coolant is water -- particularly if a barrier of 100-X effectiveness can be maintained.

Analysis of the atmospheric detritiation system requirements for the TNS and upgraded versions show that a 10^4 cfm system (cost $\sim$ \$2 M) should be adequate for all credible release scenarios. The maximum tritium inventory in the

Table III-4. Multicomponent Isotopic Separation Single Column Sensitivity Study

Variation in Feed Composition*

Number of Stages = 100
Column Pressure = 1000
Reflux Ratio = 15

	Top Product			Bottom Product		
	APH	APD	APT	APH	APD	APT
Feed 1						
APH = 2.10 APD = 48.95 APT = 48.95	6.88	90.27	2.96	10^{-7}	30.79	69.19
Feed 2						
APH = 3.75 APD = 48.12 APT = 48.12	12.49	82.83	4.73	10^{-7}	33.25	66.75
Feed 3						
APH = 7.50 APD = 46.25 APT = 46.25	23.35	72.66	4.06	10^{-7}	33.76	66.22

* APH = Atom Percent Protium
APD = Atom Percent Deuterium
APT = Atom Percent Tritium

reactor hall is $\sim$ 4 gm for TNS and $\sim$ 20 grams for TNS-upgrade. The bulk of tritium is located in a separate doubly-contained, glove-box facility in a building adjacent to a reactor hall.

Several meaningful and productive interactions have been made with the LASL/TSTA team, more of these interactions are planned during the coming months.

F. Penetration Shielding for TNS

J. Jung and M. Abdou, TNS Project

Nuclear analysis on the major penetrations for TNS has continued in two areas: (1) scoping study on shielding requirement for various penetration types and sizes; and (2) penetration shielding requirement for the specific design criteria of TNS and TNS upgrade.

The objective of the scoping study is to develop the necessary information base required to perform meaningful trade-off studies of the conflicting requirements on the penetrations and their special shields. The dependence of radiation streaming on the penetration sizes was carried out for the range of d = 0.2 -- 1.0 m, and ℓ = 2 -- 5 m, where d is the duct opening diameter at the first wall and ℓ is the duct length from the first wall to the front surface of the beam injectors. In the following, we present some of the scoping study results for the nuclear effects of the neutral beam ducts. These effects are examined in four regions: (1) components located inside the beam injector; (2) the superconducting B-coils; (3) bulk shield regions in the vicinity of the beam ducts; and (4) the F-coils.

Figure III-3 shows the maximum nuclear heating in the walls of the beam injectors as a function of duct diameter d, at several values of the duct length, ℓ. These results show that radiation streaming to the beam injector is a strong function of the penetration size. For small penetrations ($d \lesssim 40$ cm), the heating rate varies much more strongly with both length and diameter of the duct than it does for larger size penetrations ($d \gtrsim 60$ cm). For example, the heating in the walls of the injector is reduced by only an order of magnitude when ℓ is increased from 2 to 5 m for d $\sim$ 1 m, while a difference of 1 m in duct length results in reduction in the injector heating of more than a factor of 10 for d $\sim$ 0.2 m.

The vacuum pumping panels in the beam injector will be located at the immediate interior of the injector walls. If the material compositions of the cryopanels is substituted by SS, then the heating in the pumping panels is similar to that shown in Figure III-3. Nuclear heating in cryopanels must be limited to much less than $\sim$ 0.01 W/cm^3 in order to provide for a practical low-temperature cooling capability. Figure III-3 shows that for a beam duct that is 4 m long, nuclear heating in cryopanels is < 0.01 W/cm^3 only if the beam duct diameter is < 0.5 m. Zirconium-aluminum vacuum pumping panels can be successfully operated for the lifetime of the machine with duct sizes as large as one meter in diameter.

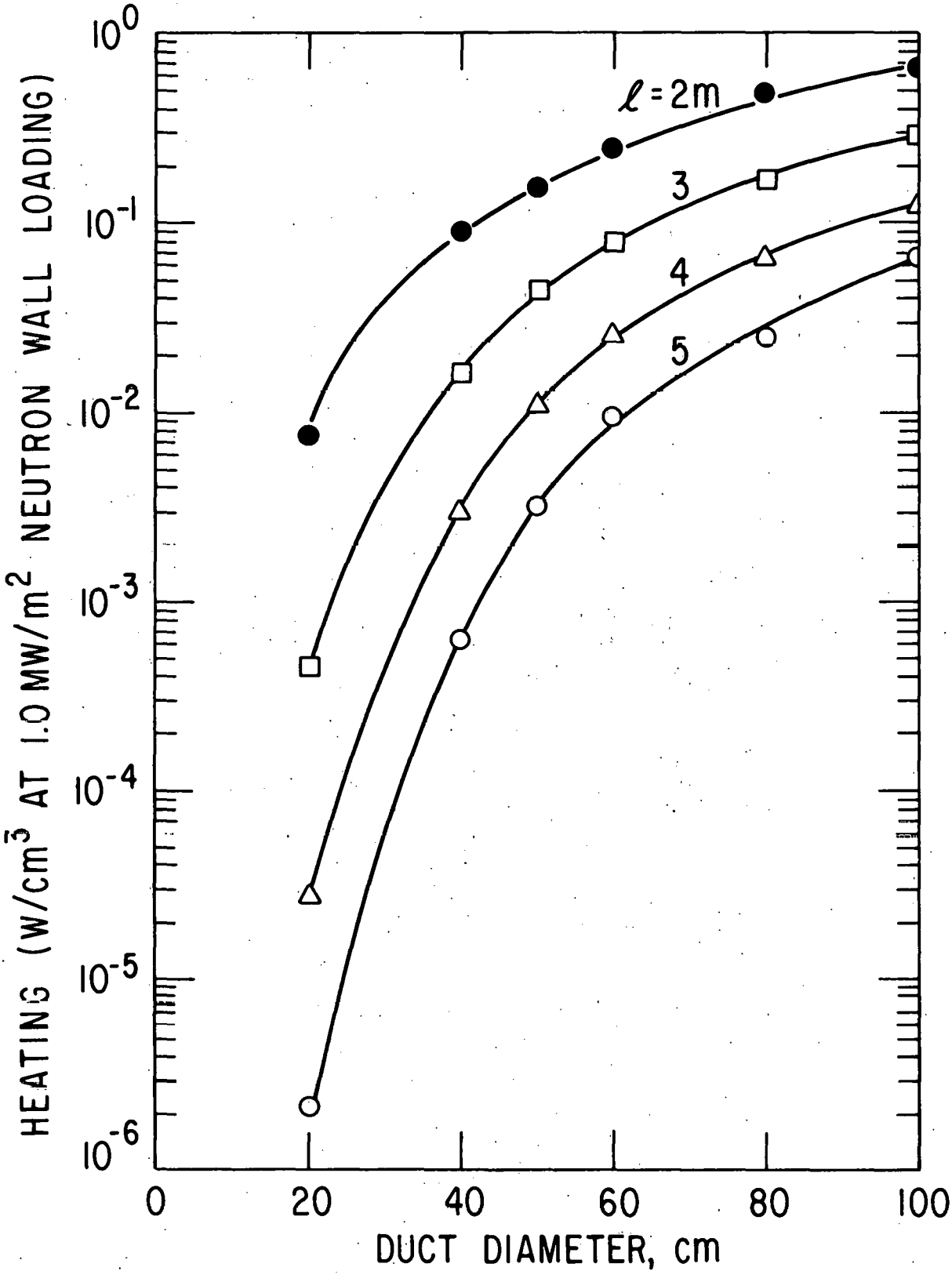

Figure III-3. Maximum nuclear heating in the beam injector wall for several values of the duct length, ℓ, as a function of duct diameter.

Some results of the nuclear radiation damage relevant to the B-coil characteristics are discussed. Figure III-4 shows the dose in epoxy-base insulators as a function of the beam duct diameter and the thickness, η, of the local exterior beam duct shield. The parameter ξ is defined as the ratio of the beam duct shield thickness to the beam duct diameter, i.e., $\xi = \eta/d$. The radiation levels in the figure are those for an integral neutron wall loading of 1 MW-yr/m^2. The figure can be used, however, to derive results at any integral neutron wall loading since the radiation level varies linearly with this quantity. It is seen, from the results of Figure III-3, that for a beam duct diameter in the range of 0.4 to 0.6 m, the shielding ratio, ξ, should be $\sim$ 0.3 for TNS (low duty factor) and $\sim$ 0.5 for TNS upgrade (higher duty factor). These observations are based on that; (a) dose limit in epoxy resin insulator is $\sim 10^9$ rad, and (b) maximum integral neutron wall loading is $\sim$ 0.1 and 1.0 MW-yr/m^2 for TNS and TNS upgrade, respectively. Note that if mylar is used instead of epoxy, the minimum allowable ξ has to be increased from 0.5 to 0.8 for TNS upgrade.

Table III-5 shows the radiation dose in a typical inorganic (Al_2O_3) insulator in the F-coil as a function of t_1 and t_2 where t_1 is the stainless steel shield thickness between the F-coil and the neutral beam duct wall and t_2 is the shield thickness between the first wall and the F-coil. For TNS (0.1 MW•yr/m^2) if the lifetime dose limit for the insulator is $\sim 10^{12}$ then no shielding of the F-coils is ncessary. For TNS upgrade (1 MW•yr/m^2) the F-coils have to be shielded away from the first wall and the beam duct. Effective shielding requires simultaneous increase of t_1 and t_2.

Table III-5. Maximum Dose in F-Coil Insulator (Al_2O_3) vs Shield Thickness

t_1 \ t_2	0	5	10	15
	Maximum Dose (Rad/MW-yr/m^2) x 10^{-12}			
0	6.7	4.9	3.8	3.0
5	6.2	4.0	2.7	1.9
10	6.1	3.7	2.3	1.5
15	6.1	3.6	2.1	1.4

t_1: Shield thickness between duct and F-coil.

t_2: Shield thickness between first wall and F-coil.

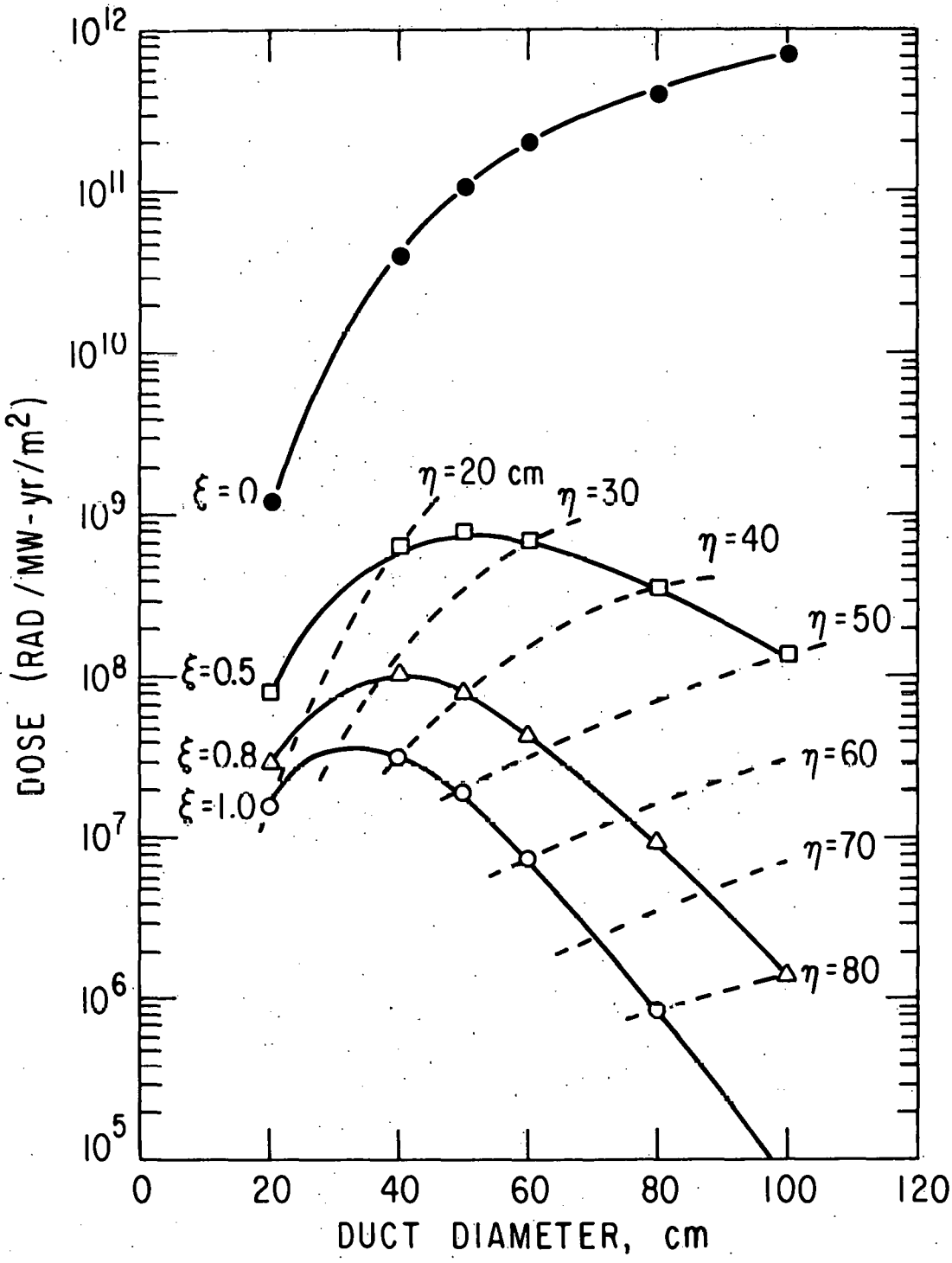

Figure III-4. Maximum nuclear dose in epoxy insulators of the B-coil as a function of duct diameter, d, and penetration shield thickness, η, ($\xi = \eta/d$).

IV. FUSION SYSTEMS ENGINEERING

A. Fusion Reactor Systems Studies

M. A. Abdou and W. M. Stacey, Jr., Applied Physics Division

Systems studies for tokamak power plants have continued in both areas of detailed subsystems analysis and global reactor system parametric analysis. The primary energy conversion subsystem study evaluated the thermomechanical performance of the first wall/blanket subsystems to determine the range of operating conditions obtainable with possible combinations of coolants and structural materials. The plasma analysis examined a wide range of MHD equilibria. The interaction of the plasma model with the system code was improved to allow investigation of a wider range of options for the major design parameters. A burn cycle analysis for a representative commercial power reactor was completed.

A study was initiated to provide an input to the definition of goals for MFE alloy development program. The study is focused primarily on the thermal stress and the creep-fatigue requirements and the target goals for neutron wall loading and material lifetime.

Among the problems examined in the global parametric analysis are the trade-offs in the plasma β_t and toroidal magnetic field strength for a fixed power and the economic dependence on the reactor thermal power.

A summary of the work carried out and sample results obtained in the systems studies is given below.

1. Trade-offs in β_t, Magnetic Field, and Reactor Power

M. A. Abdou, C. Dennis, D. Ehst, and W. M. Stacey, Jr., Applied Physics Division

One convenient way to examine the trade-offs in β_t and the maximum strength of the toroidal magnetic field, B_m, is to compare the economics of the various size reactors obtainable with different combinations of β_t and B_m for a fixed thermal power. Figure IV-1 shows the size of a 3000 MW_t as a function of B_m and β_t with other parameters fixed as indicated in the figure caption. Figure IV-2 shows the cost of energy (in mills/kwh) as a function of B_m for various values of β_t at a fixed reactor thermal power of 3000 MW_t. The reactor is lithium-cooled and employs an advanced vanadium-alloy structural material.

Several interesting trends are evident in Figure IV-2. At low magnetic fields the cost is quite sensitive to β_t -- increasing β_t from 6% to 14% for B_{TFC} = 6 T reduces the major radius of the reactor from 11.4 m to 7.5 m, and the cost is reduced by $\sim$ 30%. However, at higher magnetic fields the economic incentive of increasing β_t diminishes, and at sufficiently high fields there is an economic penalty associated with increasing β_t. For any given value of β_t, the minimum costs are obtained for toroidal field strengths in the range $8\ T \leq B_{TFC} \leq 9\ T$, which is achievable with NbTi superconductor.

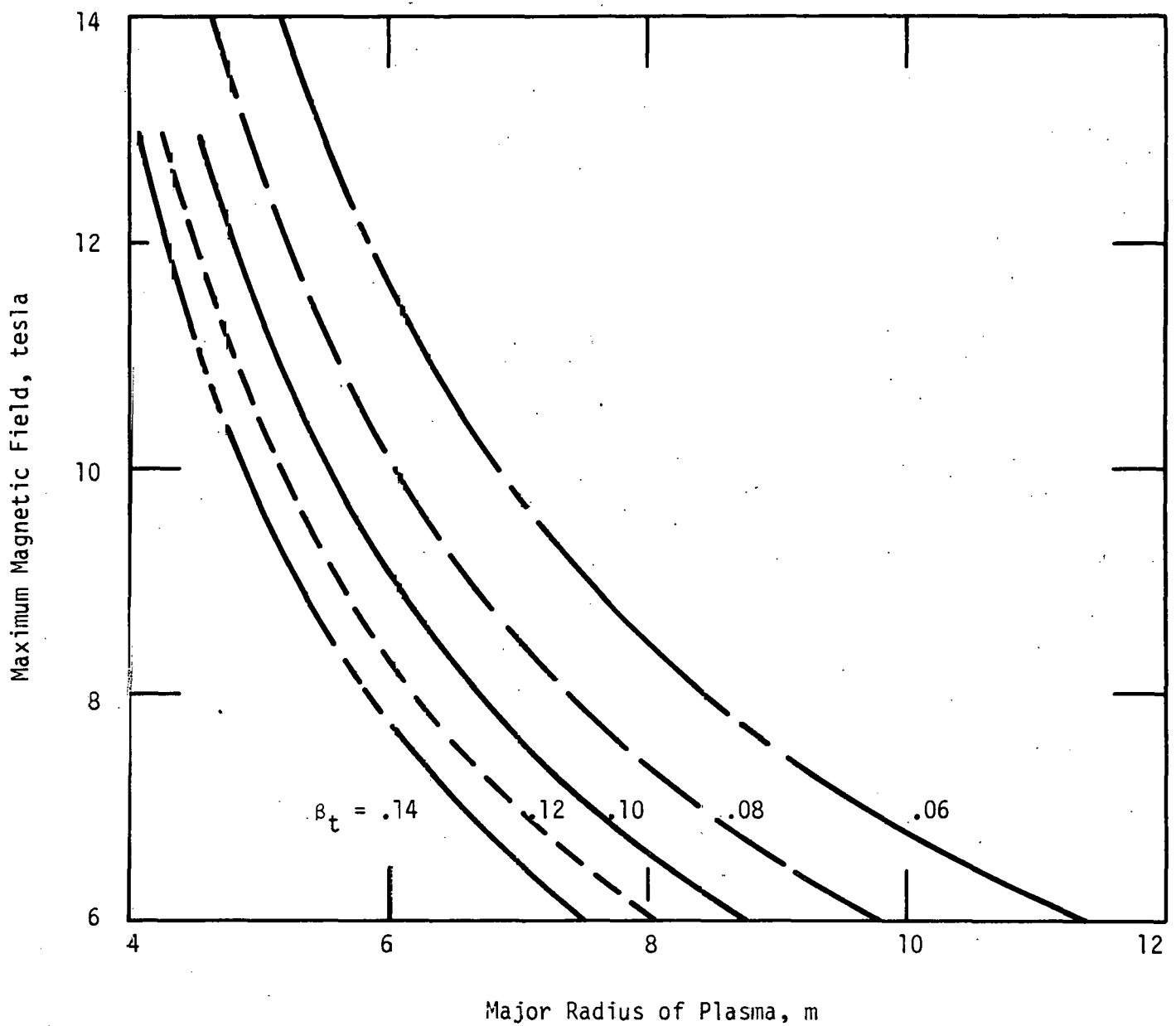

Figure IV-1. Effect of Toroidal Magnetic Field Strength and Plasma β_t on the Size of a Tokamak Reactor for a Fixed Thermal Power Output of 3000 MW(t). (Aspect ratio = 3, plasma D elongation = 1.65, plasma safety factor = 3, inner blanket/shield thickness = 1 m)

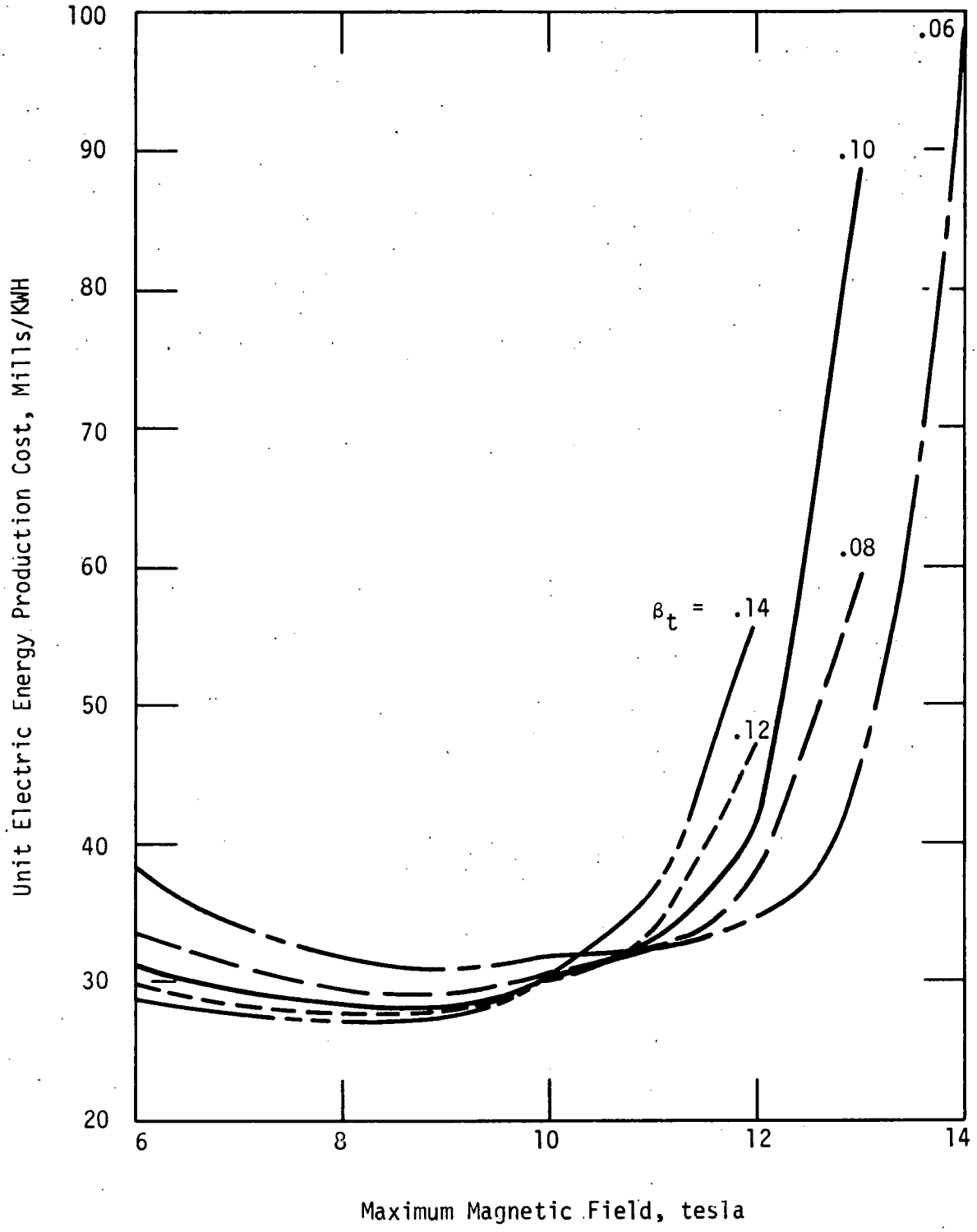

Figure IV-2. Effect of Toroidal Magnetic Field Strength and Plasma β_t on the Cost of Energy Production for a Fixed Thermal Power Output of 3000 MW(t) in a Lithium-cooled Tokamak Reactor with Vanadium-alloy Structural Material. (Aspect ratio = 3, plasma D elongation = 1.65, plasma safety factor = 3, inner blanket/shield thickness = 1 m, maximum structural temperature = 650°C, first-wall lifetime = 34 MW•yr/m^2, electrical power output ≈ 1060 MW(e))

The rather dramatic increase in costs at high field are primarily due to power supply costs for the pulsed ohmic-heating (OH) coils. These costs roughly scale as the transferred energy, which is proportional to the field squared. In the conventional reactor design concept considered in these studies, with a solenoid OH coil located inside the central core formed by the inner leg of the toroidal-field coils, the field in the OH coil increases as the central flux core decreases -- the magnetic flux is the product of the field and the flux core area. An increase in toroidal field strength reduces the flux core area in two ways: (1) the major radius decreases; and (2) the thickness of the toroidal-field coils increase -- this problem is exacerbated by the necessity of reducing the strain level for the higher-field (B_{TFC} > 9 T is this study) magnets that use Nb_3Sn superconductor. Other design concepts for the OH system, which would ameliorate this particular problem with high-field tokamak reactors, have been suggested. However, the present studies indicate that costs tend to increase at high field even when power supply costs are factored out, albeit not so dramatically as shown in Figure IV-2.

The cost of energy in mills/KWh as a function of the reactor thermal power is shown in Figure IV-3 for B_m = 9 T and two values of β_t (8% and 14%). The results are shown for both stainless steel and vanadium alloy structure.

Reduction in the cost of energy with increasing reactor thermal power, "economy of scaling", is clear in Figure IV-3. The neutronal wall loading increases with the reactor thermal power. Therefore, greater benefits of increasing the reactor power are obtainable in reactors with an advanced structural alloy (lifetime $\sim$ 34 MW•yr/m^2) than in reactors with stainless steel (lifetime $\sim$ 3.1 MW•yr/m^2) because of the more frequent wall and blanket structure replacement associated with the latter.

2. Thermal Hydraulic and Power Cycle Subsystems Analyses

B. Misra, H. C. Stevens, and V. A. Maroni, Fusion Power Program

In order to shed some light on the question of optimum power cycle concepts for commercial fusion plants, we have initiated a series of studies to evaluate and compare alternative breeding/heat-transfer/power-conversion systems.[1,2] The objectives of these studies are to (a) determine the range of operating conditions achievable with existing materials, (b) determine

---

[1] W. M. Stacey, Jr., et al., Fusion Power Program Quarterly Progress Report, October-December, 1976, Argonne National Laboratory, ANL/FPP-76-6, (1977).

[2] B. Misra, H. C. Stevens, and V. A. Maroni, "Thermal Hydraulic and Power Cycle Analysis of Liquid Lithium Blanket Designs," Proceedings of the 1977 National Heat Transfer Conference, August 15-17, 1977, Salt Lake City, Utah.

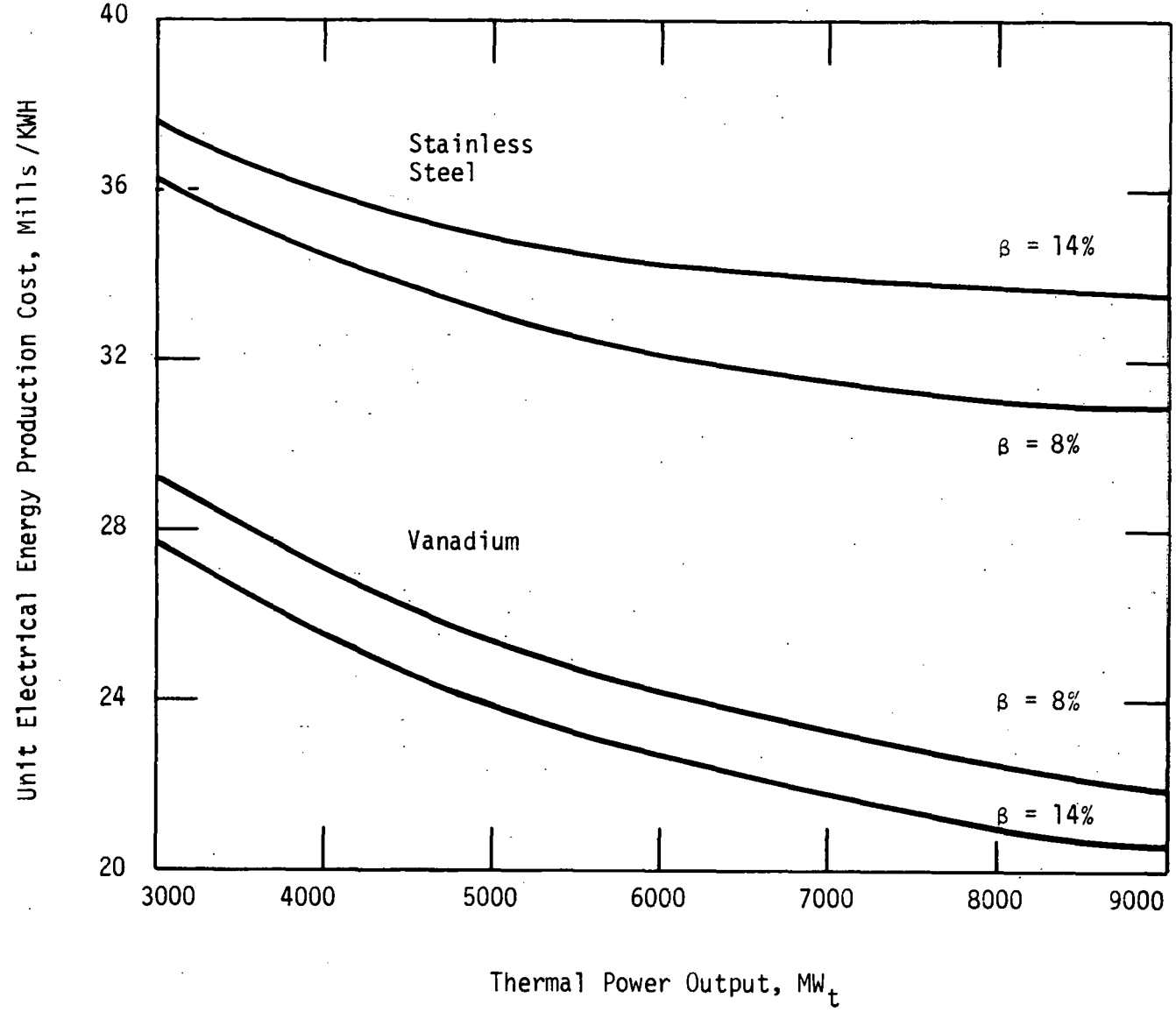

Figure IV-3. Effect of Plant Thermal Power Output on the Cost of Energy Production in a Lithium-cooled Tokamak Reactor. (Aspect ratio = 3, plasma D elongation = 1.65, plasma safety factor = 3, inner blanket/shield thickness = 1 m, maximum structural temperature = 500°C for stainless steel and 650°C for vanadium alloy, first-wall lifetime = 3.1 MW•yr/m^2 for stainless steel and 34 MW•yr/m^2 for vanadium alloy, maximum toroidal field strength = 9 T)

the materials properties required to accommodate specified regimes of wall loading and operating temperature, (c) develop a basis for predicting material response and lifetime limits in commercial reactor environments, (d) develop the formalisms required to evaluate thermal-hydraulic and thermomechanical performance of first-wall/blanket systems, (e) develop reliable algorithms for predicting the cost of fabricating and maintaining heat transfer and energy conversion systems, and (f) integrate the above menthodology into the ANL systems analysis in order to make comprehensive and meaningful assessments of commercial tokamak reactor energy conversion systems.

Analyses to date have been limited to cooling by flowing lithium, which serves both as the breeding blanket and energy transfer medium. Instead of basing the analyses on materials about which little is known regarding behavior in the anticipated harsh radiation environment and compatibility with the proposed coolants, solution-annealed type 316 stainless steel and vanadium-base alloys were selected for initial study as there is relatively more data available to define life-limiting properties under currently conceived fusion reactor operating conditions.

A number of reactor studies have addressed the question of optimum flow geometry for liquid lithium in tokamak reactors, and the blanket cell configuration depicted in Figure IV-4 is generally representative of the type of design solution normally employed. These blanket cells may be thought of as a variation of bayonet coolers with coolant entering through a duplex inlet pipe with an electrically insulated interface and then returning through the annulus. Several such cells are assumed to be connected in parallel through common inlet and outlet headers.

a. General Plant Description and Costs

For purposes of comparing stainless steel and vanadium alloys as structural materials, two base-case plants that were equivalent with respect to reactor size, wall loading and power output were considered in this part of the power cycle analyses. The two plants differ only in temperature (and, hence, thermal efficiency) and in the steam cycle pressure as major costing factors. The power plant descriptions may be listed in outline form as shown in Table IV-1. Details of the cost analyses for the two systems are presented in Reference 2. The results of the cost analyses are summarized in Table IV-2. The cost per unit power is slightly lower for the lithium-vanadium system compared with the lithium-stainless system. The spread is very small and is easily masked within the accuracy of the estimates. Table IV-2 also gives the major cost categories and highlights the more prominent sources for the cost differential between systems. In viewing the primary loop, the largest differential found is that attributable to the higher material cost of vanadium compared to that of stainless steel ($440/kg vs $12/kg). The cost differential for the two intermediate sodium loops is explained by lower ΔT of the stainless steel system requiring higher flow rates to transport the same quantity of heat. The thermal storage system, which must also be increased in size for the stainless steel system, is a major cost differential item between the two designs. The turbine plant differences reflect the higher pressure of the vanadium system, 12,400 kPa, the greater system capacity, 1223 versus 1054 MW(e) in the turbogenerator set, plus a small penalty for a large, high pressure 60 r/s turbine. The

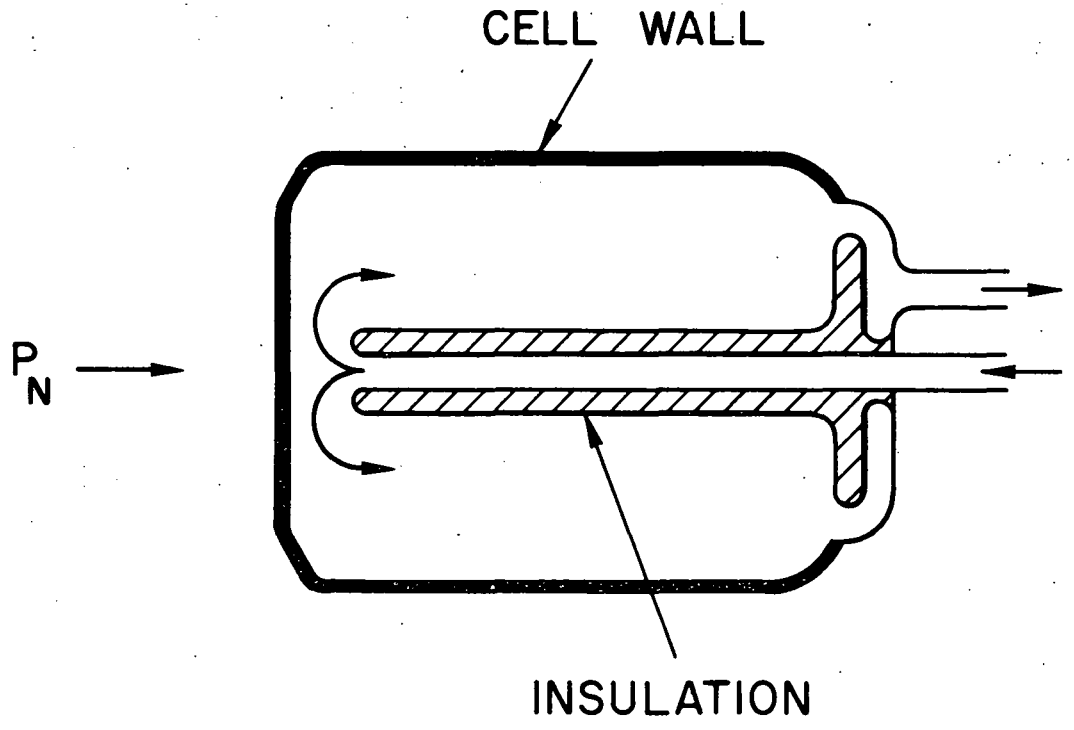

Figure IV-4. Simplified model of lithium blanket cell used in thermal hydraulic analyses.

Table IV-1. Summary of Plant Parameters for the Lithium/Stainless Steel and Lithium/Vanadium Alloy Systems

Parameter	Li-V System	Li-SS System
Neutron Wall Loading	2.8 MW/m^2	2.8 MW/m^2
Plasma Duty Factor	95%	95%
Steady-State Power Output	2850 MW(th)	2850 MW(th)
Number of Loops	3	3
Rating per Loop	950 MW(th)	950 MW(th)
Primary Coolant Loop	Lithium	Lithium
Reactor Outlet Temp.	620°C	490°C
Reactor Inlet Temp.	380°C	250°C
System Pressure	2758 kPa	2758 kPa
Flow Rate	2.1 m^3/s	2.1 m^3/s
Materials	Vanadium Alloy	Stainless Steel type 316
Intermediate Coolant Loop	Sodium	Sodium
Sodium Inlet	600°C	445°C
Sodium Outlet	360°C	240°C
Flow Rate	3.3 m^3/s	4.3 m^3/s
System Pressure	$\leq$ 2758 kPa	$\leq$ 2758 kPa
Thermal Storage Dwell	90 s	90 s
Thermal Storage Vol.	416 m^3	681 m^3
Materials	SS and ferritic steel	SS and ferritic steel
Major Components	Pumps, piping, evaporator, superheater, and thermal storage	Pumps, piping, and once-through steam generator
Ancillaries	Purification, emergency heat removal, inert gas, etc.	Purification, emergency heat removal, inert gas, I&C, etc.
Steam Generator System	Superheated steam	Superheated steam
Steam Temperature	510°C	400°C
Steam Pressure	12,400 kPa	8,620 kPa
Feedwater Temp.	250°C	195°C
Condenser	5 kPa	5 kPa
Gross Electrical Output	1223 MW(e) (gross)	1054 MW(e) (gross)
Efficiency	~ 43%	~ 37%
Steam System	Evaporator, recirculating type, using a steam drum separator and recirculating pumps	Steam reheat system for high pressure turbine section

Table IV-2. Preliminary Cost Comparisons for Energy Conversion Systems[a]

(In Thousands of $)

Acct.	System	Lithium Vanadium	Lithium Stainless Steel	PLBR[1] LMFBR	LWR[2]	UWMAK-III[3]
21	Structures & Improvements	~150,000	150,000	120,000	52,000	568,000
22[a]	Primary Coolant Loop Lithium	93,662	52,050	149,500	18,000	-
	Intermediate Coolant Loop	99,614	111,800	193,800	39,500	-
23	Turbine Plant	134,180	110,217	156,614	93,518	-
24	Electric Plant	25,539	22,010	45,090	21,702	-
25	Miscellaneous Plant	7,134	6,148	-	6,330	-
	Total	510,129	452,225	665,000	231,000	1,808,000*
	Gross Electric Output, MW(e)	1223	1054	1096	1065	1985 (Net)
	Partial Direct Cost in $/kWe	417	429	606	216	910

[a] Only partial direct costs relevant to the comparison.

* Total includes applicable cost from UWMAK-III estimate.

[1] M. Shackelford, Argonne National Laboratory, personal communication.

[2] WASH-1230, Volume 1 (1972).

[3] See reference 3.

The electric plant differential is strictly due to the efficiency/capacity ratio as is the miscellaneous plant item. It is interesting to note that in many cases it was considered impractical to take full advantage of the high strength of the vanadium alloy due to fabrication restrictions. Ignorance of this factor would have made the vanadium system even more attractive.

Although the cost per unit power is approximately the same for the vanadium and stainless steel system, additional parametric analysis[3] show that vanadium systems result in significantly lower cost of energy production (mills/Kwh) than that for the stainless steel systems. This is due to the expected longer lifetime with the vanadium base alloys.

b. Thermal Hydraulic Analyses

Typical results of thermal hydraulic analyses for four reference cases (stainless steel with and without a divertor and vanadium alloy with and without a divertor) are presented in Tables IV-3, IV-4 and IV-5 and Figures IV-5 and IV-6. In Figures IV-5 and IV-6 the maximum allowable neutron wall loading, coolant inlet and exit temperatures, thermal stress, coolant inlet velocity and pumping power to thermal power ratio, are plotted as a function of blanket cell wall thickness based on (a) the thermal-hydraulic model described above, (b) a maximum toroidal field of 8 T, and (c) the materials criteria listed in the upper half of Table IV-3. For stainless steel (with or without a divertor) the maximum neutron wall loading generally occurs at relatively low wall thicknesses and is limited by the thermal stress criterion (maximum thermal stress = material yield strength). For vanadium alloys this maximum occurs at somewhat larger wall thickness values and is limited by the minimum coolant inlet temperature criterion. The values of the maximum allowable neutron wall loading for 8, 10, and 12 T maximum toroidal fields are listed in the lower half of Table IV-3. The total pressure drops were nominally in the range from 3 to 6 MPa (including the safety factor of 2.0 on all calculated pressure losses).

Early trade-off studies on the coolant temperature rise showed that the values in Table IV-3 (i.e. 225°C for stainless steel and 325°C for vanadium alloy) are near to optimum for each material based on the thermal-hydraulic model and maximum structural temperature limits used herein. Also, the pumping power to thermal power ratio (based on geometrically averaged values of actual magnetic field strength inside the reactor) was found to be < 1.0, < 1.5 and $< 2.0\%$ for maximum toroidal fields of 8, 10 and 12 T, respectively. There is some doubt as to whether the fluid inlet velocities for the stainless steel case (Figure IV-5) are high enough to avoid stagnation effects near the first-wall surface of the cell, however, more detailed fluid dynamic studies would be needed to fully resolve this question.

Several cases were analyzed for effect of varying the size of the inlet piping to the blanket module while keeping the blanket cell size constant (e.g. cell diameter = 0.5 m). The thermal hydraulic results were found to be rather insensitive to small changes in inlet tube diameter since only the

---

[3] M. A. Abdou, et al., "Impact of Major Design Parameters on Economics of Tokamak Power Plants," Trans. Am., Nucl. Soc., 25 (June, 1977).

Table IV-3. Results of Wall Loading Trade Studies for Lithium-Cooled Stainless Steel and Vanadium-Alloy Blanket Systems[a]

Criteria		Li-Cooled V Alloy	Li-Cooled SS
Maximum Allowable Temp., °C		650	500
Maximum Thermal Stress, MPa		351	117
Minimum Wall Thickness, mm		2.5	2.5
Maximum Wall Thickness, mm		8.0	8.0
Minimum Coolant Inlet Temp., °C		235	235
Coolant Temperature Rise, °C		325	225
Maximum Neutron Wall Loading, MW/m^2			
$F^b = 0.10$	8 Tesla	11.2[c]	3.8[d]
	10 Tesla	7.5[e]	3.2[d]
	12 Tesla	5.3[e]	2.8[d]
$F^b = 0.25$	8 Tesla	8.0[c]	2.0[d]
	10 Tesla	6.2[c]	1.9[d]
	12 Tesla	4.6[c]	1.7[d]

a. For a cell diameter of 0.5 m and an inlet tube diameter of 0.1 m.

b. F = Fractional power loading on first wall surface due to particle and radiation effects.

c. Limited by minimum coolant inlet temperature criterion.

d. Limited by maximum thermal stress criterion.

e. Limited by MHD pressure stress criterion (i.e. maximum cell wall thickness insufficient to support higher coolant velocity).

Table IV-4. Summary of Trade Studies[a] on Materials Limitations for Lithium-Cooled Stainless Steel Blanket Cells

Parameter	With Divertor			Without Divertor		
Maximum Structural Temperature, °C	500	500	600	500	500	600
Thermal Stress Limit, MPa	117	234	234	117	234	234
Maximum Neutron Wall Loading, MW/m^2	3.8	7.5	7.5	2.0	4.0	4.1
Cell Wall Thickness, mm	3.0	2.5	2.5	2.5	2.5	2.5
Coolant Exit Temperature, °C	485	476	577	493	487	572
Pumping Power/Thermal Power, % 0.2	0.3	0.3	0.3	0.1	0.2	0.3
Coolant Velocity, m/s	0.3	0.5	0.5	0.2	0.3	0.3

a. Criteria: Coolant Inlet Temperature $\geq$ 235°C
Coolant Temperature Rise = 225°C
Safety Factor = 2.0

Table IV-5. Summary of Trade Studies[a] on Materials Limitations for Lithium-Cooled Vanadium Alloy Blanket Cells

Parameter	With Divertor		Without Divertor	
Maximum Structural Temperature, °C	650	750	650	750
Maximum Neutron Wall Loading, MW/m^2	11.2	13.6	8.0	10.3
Corresponding Cell Wall Thickness, mm	5.5	6.0	3.0	3.0
Thermal Stress, MPa	186	248	152	193
Coolant Exit Temperature, °C	567	571	556	564
Pumping Power/Thermal Power, %	0.9	0.8	0.5	0.4
Coolant Velocity, m/s	0.6	0.7	0.4	0.6

a. Criteria: Coolant Inlet Temperature $\geq$ 235°C
Coolant Temperature Rise = 325°C
Cell Wall Thermal Stress $\leq$ 351 MPa
Safety Factor = 2.0

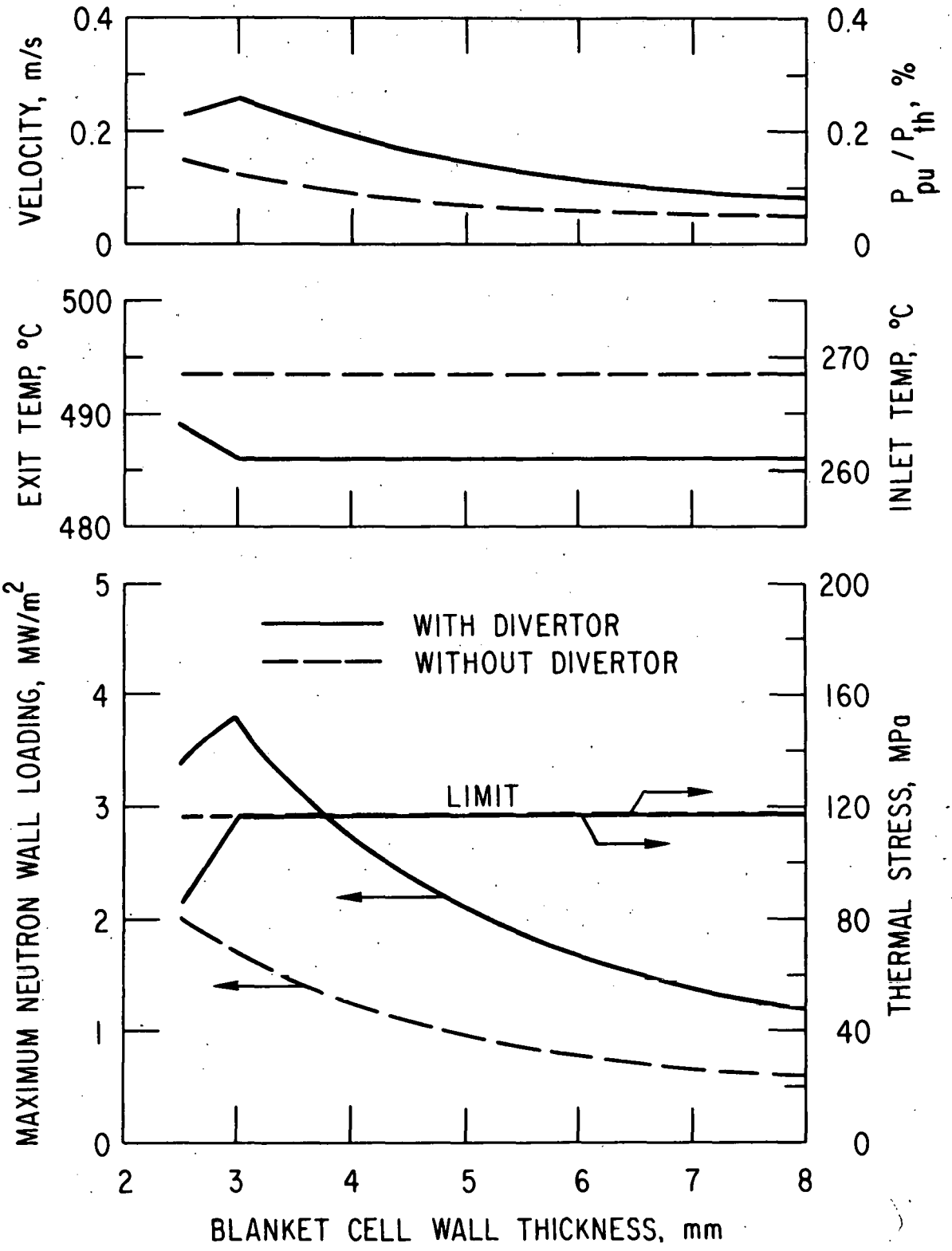

Figure IV-5. Lithium-cooled stainless steel blanket cells (cell diameter = 0.5 m, inlet tube diameter = 0.1 m).

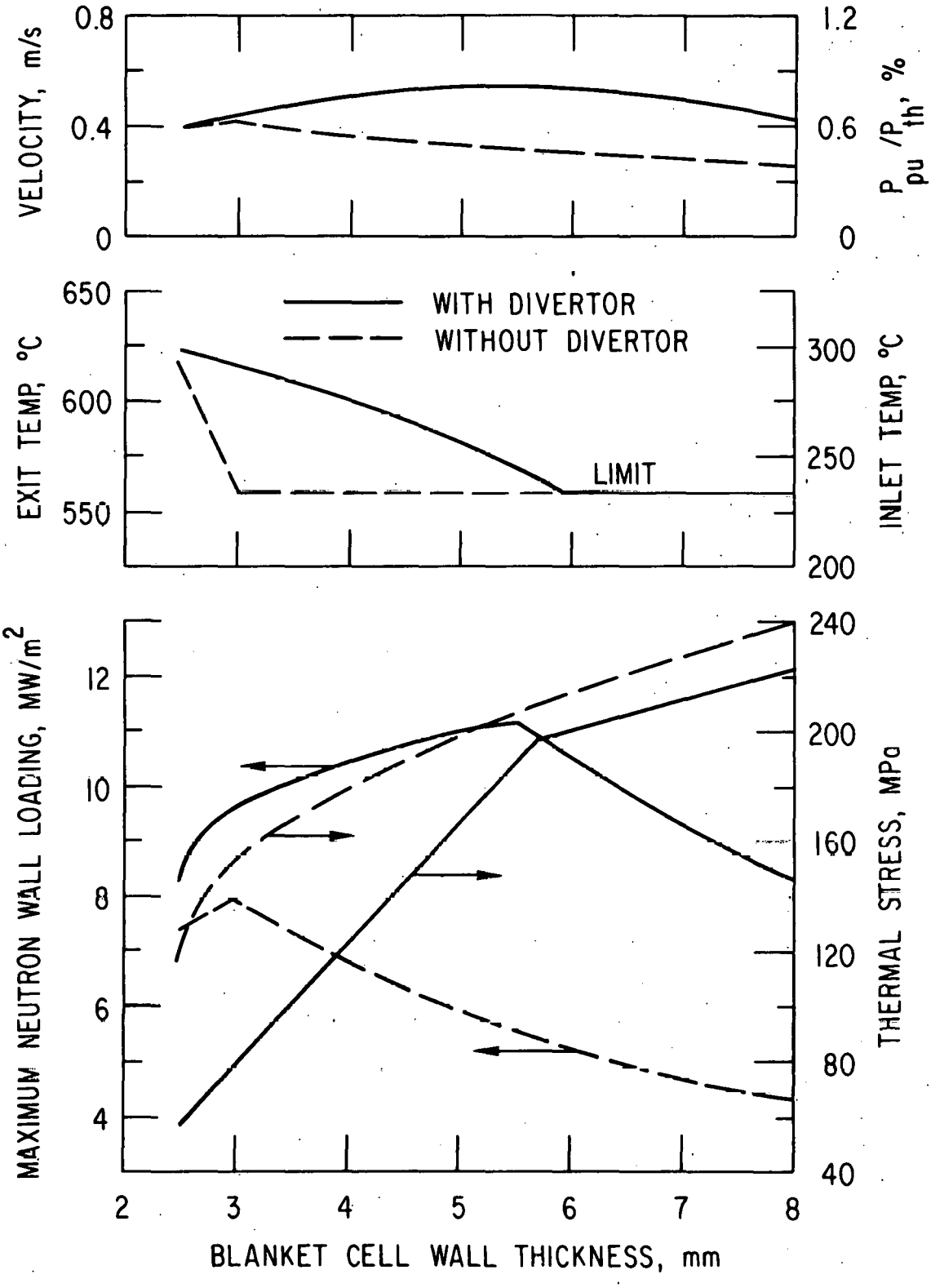

Figure IV-6. Lithium-cooled vanadium alloy blanket cells (cell diameter = 0.5 m, inlet tube diameter = 0.1 m).

pressure drop in the inlet tube is affected by this parameter. It can be easily shown that the size of the blanket cell cannot be varied over a wide range, although a cell diameter of 0.5 m is not necessarily the optimum. Increasing the cell diameter in order to reduce the number of modules required leads to larger cell wall thicknesses with resultant higher thermal stresses and lower coolant exit temperatures. A reduced cell size has the beneficial effect of lower wall thickness and lower thermal stresses, however, it increases the number of cells required for a given geometry. It may be noted that for the reactor size selected for this analysis, more than 5000 of the 0.5-m diameter cells would be needed. Since this is already a very large number, there is little incentive to go to a larger number of smaller modular units.

Tables IV-4 and IV-5 show the effect on overall thermal-hydraulic performance of increasing the limiting materials criteria for both stainless steel and vanadium alloy. For stainless steel, which is usually found to be thermal stress limited, doubling the thermal stress limit tends to double the maximum allowable neutron wall loading and raising the upper operating temperature limit by 100°C increases the coolant exit temperature by an approximately equal increment. Increasing the upper operating temperature for vanadium by 100°C increases the maximum allowable wall loading but has little apparent effect on the coolant exit temperature. However, for a given wall loading, it is possible to achieve a higher coolant exit temperature with the higher upper operating temperature value. It should be noted here that the same coolant temperature rise values were used for all cases in Tables IV-4 and IV-5, although it is known that the coolant temperature rise corresponding to optimum thermal-hydraulic performance is indeed sensitive to and increases with peak allowable structural temperature.

Details of the thermal hydraulic analyses described above are presented in Reference 2.

3. Plasma Subsystem Analysis

D. Ehst, K. Evans, E. Goldstick and C. Dennis, Applied Physics Division

The plasma subroutine has been upgraded to survey a larger variety of MHD equilibria and plasma conditions and to allow greater flexibility in calculating reactor characteristics. A library was generated for a wide range of ideal MHD equilibria, resulting in a substantial savings in computing time. The MHD variables, which specify a unique equilibrium, are:

- A = aspect ratio
- κ = plasma elongation
- d = plasma triangularity
- α = pressure profile
- q = safety factor at limiter
- β_t = average toroidal beta.

If an equilibrium is not found in the library for the given inputs, the code must be given two other parameters:

β = diamagnetic function profile
α_J = diamagnetic magnitude.

With this information an equilibrium is computed for the given A, κ, d, and α, and the associated q, β_t, $\psi(r,z)$, and plasma current are stored in the library for future use.

The survey of MHD equilibria has been enlarged to determine sensitivity to all six MHD inputs, probing the following parameter ranges:

A = 2.5 - 4.0
κ = 1.0 - 2.0
d = -0.5 - 0.75
α = 1.0 - 2.0
q = 2.0 - 4.0
β_t = 0.04 - 0.18

Results will be described below.

The power balance sensitivity has also been examined in detail by calculating both $n\tau$ and thermal power P for various plasma conditions. Since actual thermal power is a function of geometry, the reactor dimensions were fixed and P values are in relative units for this particular study. The plasma parameters, which were independently varied, are:

$\overline{T}_e$ = average electron temperature

Z_{eff} = effective ion charge state; a 50% D-T fuel mix with alpha particles, 0.5% oxygen density, and variable iron-ion density were considered

α = pressure profile

α_n = density profile

impurity quality: for fixed Z_{eff} (= 1.7) beryllium was substituted for iron to observe low-Z effects.

The ranges surveyed are:

$\overline{T}_c$ = 4 - 40 keV
Z_{eff} = 1.3 - 3.8
α = 1.0 - 2.0
α_n = 0.1 - 2.0.

These results are also discussed below.

The interface of the plasma calculational subroutines with the rest of the systems analysis code has been greatly improved to allow a considerable degree of flexibility in selecting any specific scenario for deriving a consistent set of major reactor design parameters.

A summary of the trends among reactor design variations will now be presented. The MHD survey independently varied the five parameters A, κ, d, α, and q and found numerous equilibria at various β_t values at each point. The plasma current, I_p, normalized to the TFC magnet current, was considered a figure of merit.

1. Equilibria insensitive to triangularity: I_p/I_{TFC} increases slightly with d at fixed β_t. Thus circular or reversed D plasmas, with large volumes and relatively small currents, are slightly more attractive than highly-D shaped cross sections. Surely the stability differences between positive and negative triangularity will dominate these effects.

2. Equilibria improve mildly for broad pressure profiles ($\alpha \to 1$): rotational transform and current density become questionable for peaked profiles ($\alpha \to 2$). The pressure profile has a negligible effect on I_p/I_{TFC}.

3. Equilibria improve with smaller safety factor: rotational transform and current density remain smooth to higher values of β_t when q = 2.0 than when q = 4.0. Of course, lower q values require larger plasma currents; also, the lower limit on q from the stability point of view is an unsettled question.

4. Equilibria improve with smaller aspect ratio: higher β_t values obtain for A = 2.5 than for A = 4.0. Likewise volume is larger for smaller A. Disadvantages of low A are higher plasma currents and smaller average magnetic fields for a given B field at the TFC. The important observation is that $\overline{B^4}$ x (torus volume) actually decreases with smaller A, so β_t^2 must increase substantially with smaller A to favor low aspect ratio reactors. This factor coupled with associated engineering difficulties may diminish the importance of achieving small A.

5. Equilibria improve substantially with elongation: higher β_t values and larger volumes are found with large κ. Of course, the larger plasma volumes associated with large κ require larger plasma currents.

6. Power balance ($n\tau$ and P) insensitive to relative widths of temperature and density profiles.

7. Thermal power P insensitive to Z_{eff} except ignition impossible ($n\tau \to \infty$) at large Z_{eff}.

8. Ignited iron impurity plasma with $Z_{eff} = 1.7$ has moderately higher power P than beryllium plasma with the same $Z_{eff} = 1.7$.

9. Temperature for maximum thermal power reduced significantly for peaked pressure profiles compared to flat profiles ($\bar{T}_e \to 8$ keV for $\alpha \gtrsim 1$ compared to $\bar{T}_e \gtrsim 13$ keV for $\alpha = 0$).

10. At fixed β_t power improves mildly for narrow pressure profiles ($\alpha \to 2$).

Based on the results of these surveys, future plasma subsystem studies will concentrate on the following reactor parameter subspace:

$\alpha = 1.4$
$\alpha_n = 0.3$
$\underline{q} = 3.0$
$\bar{T}_e = 8$ keV
$Z_{eff} = 1.7$

4. Reactor Plasma Driving Subsystems Analysis

J. N. Brooks, Applied Physics Division

An initial study of the plasma driving system requirements for a commercial tokamak reactor has been completed. This study examined the effect of different types of hardware and operating modes on the driving system and burn cycle of a typical, 8 M major radius, 1000 MW_e fusion reactor (see last progress report). The reactor was assumed to have a superconducting central OH coil and a superconducting EF coil located outside the blanket and shield, and external to the TF coils. The plasma is moderately non-circular ($\kappa = 1.3$) and has a maximum beta of 8%. The results of the analysis for this reactor should be valid, in a qualitative sense, for a wide class of reactor designs with a similar coil configuration and reasonably similar plasma parameters. The principal conclusions of this study are as follows:

1. The startup of a large commercial reactor will take about the same time ($\lesssim 10$ s) as an EPR.

2. $\dot{B}$ requirements become smaller than for an EPR sized device, basically because the OH coil radius is much larger. The resistive volt-second consumption during startup becomes a smaller fraction of the total volt-seconds and therefore becomes less critical.

3. On the other hand, the EF reactive power requirements becomes large; minimizing the EF power supply cost will probably dictate the choice of an operating mode. The best operating mode, in general, is a relatively slow OH reversal ($\gtrsim 3$ s) with the neutral beam turned on after the reversal, not during it.

4. A homopolar generator appears quite feasible (cost and technology) as a transfer device for the OH system. The energy storage requirements for a homopolar are much the same as for an EPR. A typical operating mode and driving system requirements for this reactor are: OH reversal time = 3 s, beam turn on time = 3 s, homopolar energy storage = 1460 MJ, EF supply reactive power = 1500 MVA, $\dot{B}^{MAX}_{OH} = 2.5$ T/s. The OH and EF supply costs would be \$93 M for this case.

5. A single resistor or a switchable combination of resistors, probably 3 or more, also looks feasible and perhaps better than a homopolar, particularly if the burn time is to be maximized. A dump resistor is fairly cheap, and allows full use of the available flux swing of the OH coil, but its use is restricted to reactor designs where the flux swing in only one direction is sufficient for startup.

6. A rectifier type power supply (SCR type) involves about the same EF requirements and enables a small reduction in $\dot{B}_{OH}$ but the cost of the supply is much higher than a homopolar generator or a resistor. A rectifier power supply, therefore, appears to be completely uneconomic as the OH transfer device though it will have to be used to drive the EF coils.

7. A preliminary analysis of the shutdown period indicates that some means of controlling (spoiling) the energy confinement time in the plasma will probably be needed so that the plasma thermal energy can be removed in an orderly way. The alternative scheme of injecting a high-Z impurity such as argon to increase radiation losses may impose very high voltage requirements on the EF supply (because the plasma cools too quickly below $\bar{T}_i \lesssim 4$ keV). Assuming that an adequate control scheme could be obtained, then the driving system requirements for shutdown will probably not exceed those set by the startup. A separate detailed analysis of shutdown is needed to resolve these questions.

B. Development of Blanket Processing Technology for Fusion Reactors

W. F. Calaway, J. R. Weston, and V. A. Maroni, Chemical Engineering Division

The program underway at the Argonne National Laboratory to initiate the development of processing technology for liquid lithium-breeder blankets is continuing. Progress during the second quarter of FY-1977 is summarized below.

1. Lithium Processing Test Loop (LPTL)

Work on the LPTL[4-6] is proceeding on schedule. All of the support structures and vessels (reservoir tank, dump tank, salt tank, lithium transfer carboy, salt transfer carboy, getter-trap, cold-trap, and two hydrogen meters) have been received from the fabricator

---

[4] W. M. Stacey, et al., Fusion Power Program Quarterly Progress Report, October-December, 1976, Argonne National Laboratory, ANL/FPP-76-6, (1977).

[5] W. M. Stacey, et al., Fusion Power Program Quarterly Progress Report, July-September, 1976, Argonne National Laboratory, ANL/FPP-76-5, (January, 1977).

[6] W. F. Calaway, et al., "Review of the ANL Program on Liquid Lithium Processing and Tritium Control Technology," Proceedings of the Second ANS Topical Meeting on the Technology of Controlled Nuclear Fusion, Richland, Washington, September 21-23, 1976, CONF-760935-P3 (1976).

and are presently undergoing acceptance tests at ANL. The instrumentation platform and electronic consoles have been assembled, and installation of some of the control circuits has been completed. Fabrication of the piping sections is proceeding on schedule for delivery in early May. An order has been placed for 50 gallons of lithium, which will be delivered to ANL in the specially constructed lithium transfer carboy. The ingredients of the molten salt to be used in initial salt extraction tests on the LPTL (i.e., LiF-LiCl-LiBr) have been received and plans are being formulated for the preparation of ∿ 15 gal of the low-melting (450°C) solid solution phase and the loading of this salt into the salt transfer carboy. Design and procurement of hardware for gas handling systems, the multipurpose sampler for the reservoir tank, and the electrochemical processing units for the salt tank are proceeding in pace with the main fabrication and assembly efforts.

2. Molten Salt Reprocessing

Bench scale studies to verify and refine the salt processing step in the molten salt extraction scheme for recovering hydrogen isotopes from liquid lithium have been brought to a close so that more time can be devoted to the assembly of the lithium processing test loop (LPTL). The sparged electrode salt-cleanup method described in the previous progress report[4] has been selected for adaptation to the LPTL salt tank.[5] With regard to the studies[4] of recovery efficiencies for elements other than hydrogen, more definitive tests of the capability of this clean-up method to remove carbon, nitrogen and other impurities will be carried out when the LPTL is operational.

During the second quarter of FY-1977, the apparatus used to conduct the bench scale processing tests was dismantled and portions of the stirrer and electrode assemblies that were in contact with the lithium-saturated salt (LiF-LiCl-LiBr) for extended periods of time (∿ 2000 hours) at temperatures near 500°C were submitted for metallographic examination. A porous zone of approximately 4 μm thickness was observed on the surface of all pieces as was evidence of intergranular attack to depths of ∿ 35 μm. In reflecting on the implications of these results, several additional factors bear mentioning.

1. On several occasions all of the examined pieces were removed from the bench scale apparatus, cleaned (by soaking in water), and reused.

2. Each piece was exposed to temperatures in excess of 600°C for short time periods (several hours) while it was immersed in the molten salt.

3. Each piece was either in motion (stirrer) or electrochemically active (electrodes) while it was in the salt.

4. On the other hand, all of the pieces were in a totally unstressed condition at all times during their use in the salt pot.

While the observed corrosion could have been abetted by any of or all of the first three conditions outlined above, and although the extrapolated corrosion rate does not portend serious consequences to the LPTL salt tank,

the potential for long-term corrosion, particularly in stressed components as indicated by these results, needs further study in better defined and controlled environments.

In another area of work, a half-scale glass mock up of the salt tank to be used on the LPTL has been received and is now being adapted to permit tests of the microprocessor driven control circuit developed for the salt tank. An aqueous and an organic phase appropriately matched in specific gravity ratio and viscosity will be used to simulate the lithium and salt phases in these tests.

3. Lithium Mini Test Loop (LMTL) Studies

The LMTL described in previous progress reports,[4,5] has continued to operate through 4000 hours. The two Nupro bellows sealed valves (typical of the type to be used on the LPTL) remain intact even though one of these valves has been subjected to over 130 operating cycles (opened and closed). Time-temperature histories for the primary loop and the thermally regenerative getter trap are shown in Figure IV-7. Also shown in Figure IV-7 are the results of periodic analyses for nitrogen, zirconium, nickel, iron, and chromium. (The nitrogen analyses were performed by a micro-Kjeldahl method; iron, chromium and nickel were analyzed by atomic absorption, and zirconium was analyzed by a colorimetric method.) The apparent rise in nitrogen level after 1200 hours may be indicating that the effectiveness of zirconium to getter nitrogen at temperatures in the 500 to 550°C range has been used up. An increase in getter temperature to 650°C is planned in order to determine whether the nitrogen trapping capability of the zirconium can be revitalized, i.e., by increasing the rate of diffusion of nitrogen into the bulk zirconium. The possibility that at least part of the dissolved nitrogen is present as either zirconium or chromium nitrides is also being investigated.

The nickel and iron concentrations appear to have leveled off at values of 900 to 150 wppm, respectively, which may represent the saturation values for each element at the loop operating temperature ($\sim$ 475°C). These values are in reasonably good agreement with earlier solubility studies by Sand[7] ($\sim$ 100 wppm iron at 500°C) and by Bagley and Montgomery[8] ($\sim$ 760 wppm nickel at 500°C). The fluctuations in the chromium and zirconium levels could be due at least in part to analytical uncertainties. Other plausible reasons for the apparent peaking of the concentration of these elements near 1800 hours are being considered.

---

[7] J. J. Sand, "Solubility of Iron in Liquid Lithium," Olin Mathieson Chemical Corporation Report OMCC-HEF-166 (August, 1968).

[8] K. Q. Bagley and K. R. Montgomery, "The Solubility of Nickel in Lithium," UKAEA Report IGR-TN/C-250 (September, 1955).

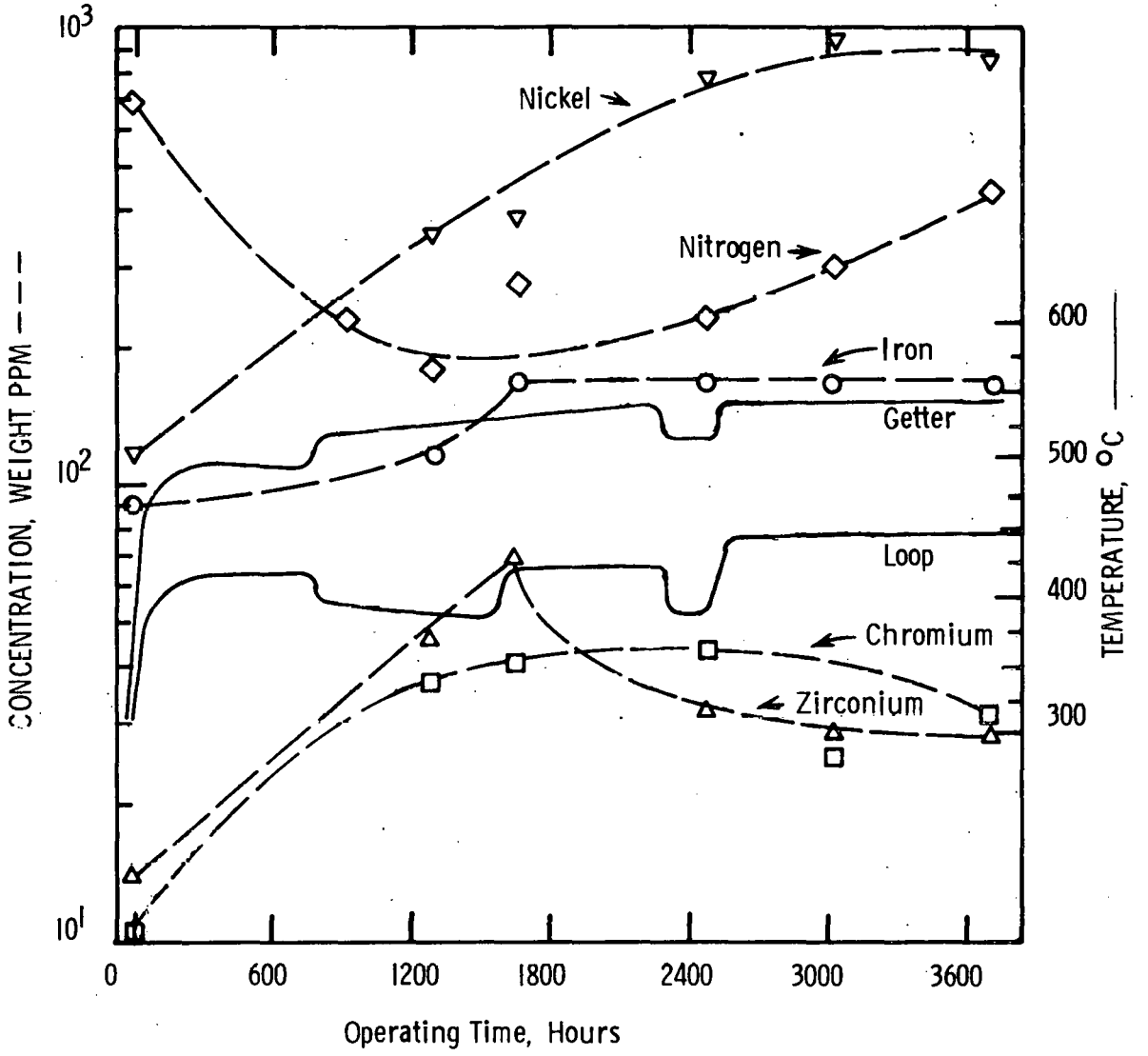

Figure IV-7. LMTL Getter Bed and Loop Temperature Histories and Impurity Concentration vs. Time Curves

C. Plasma Systems Engineering

K. Evans, Jr.,and E. Goldstick, Applied Physics Division

Until recently, the limits on plasma magnetohydrodynamic (MHD) equilibrium have largely been determined by the low β, high aspect ratio formulas[9]

$$q(a) = \frac{a\ell B_T}{RB_p} = \frac{2\pi a^2 \ell^2 B_T}{RI} \tag{1}$$

$$\beta_p = \frac{2\mu\bar{p}}{B_p^2} = \frac{8\pi^2 a^2 \ell^2 \bar{p}}{\mu I^2} \tag{2}$$

with assumed limits of $q(a) \gtrsim 2.5$ (based on experimental results) and $\beta_p \lesssim A/2$ (Shafranov limit).[10] (Operation at q = 2.5 has been accompanied by degraded energy confinement, so that q = 3 is perhaps more realistic as a lower limit, especially in view of the fact that experiments are usually operated with q nearer to 4-5.) The Shafranov limit is based on a skin current model. The elongation factor ℓ in Equations 1 and 2 indicates elongated cross sections may be desirable.

In order to more completely assess the limits on MHD equilibria in a tokamak, a survey of equilibria with a variety of cross sectional shapes, aspect ratios, and pressure and diamagnetic effect ($F \equiv RB_t$) profiles has been undertaken. The equilibria are calculated numerically from the MHD equilibrium equation

$$\Delta^*\psi = \nabla\cdot\left(\frac{\nabla\psi}{R^2}\right) = -4\pi^2\mu\frac{dp}{d\psi} - \frac{4\pi^2 F}{R^2}\frac{dF}{d\psi} \tag{3}$$

for prescribed $p(\psi)$, $F(\psi)$, A, and plasma boundary defined by

$$R = R_o + \frac{R_o}{A}\cos(\theta + d\sin\theta) \tag{4}$$

$$Z = \frac{\kappa R_o}{A}\sin\theta\ . \tag{5}$$

The plasma elongation is determined by κ, and the D-shapedness, by d. The pressure and diamagnetic function profiles are taken to be of the form

$$P = P_o\,\hat{\psi}^{\alpha} \tag{6}$$

$$F^2 = F_o^2\,(1 - \delta\hat{\psi}^{\beta}) \tag{7}$$

---

[9] S. O. Dean, et al., "Status and Objectives of Tokamak Systems for Fusion Research," WASH-1295 (1974).

[10] V. S. Mukhovatov and V. D. Shafranov, Nucl. Fusion 11, 605 (1971).

with

$$\hat{\psi} = \frac{\psi_\ell - \psi}{\psi_\ell - \psi_m} \quad . \tag{8}$$

($\psi = \psi_\ell$ at the limiter and $\psi = \psi_m$ at the magnetic axis.) By varying α and β one can obtain a variety of profiles from flat to sharply peaked. The parameter

$$\alpha_J = \frac{2\alpha\delta P_o \mu R_o^2}{\beta F_o^2} \tag{9}$$

is more convenient than δ.

The quantity P_o is determined by the requirement that $q(0) = 1$ (Kruskal-Shafranov limit). The equilibria do not depend significantly on R_o and F_o, so that equilibria with different values of these quantities can be obtained by simple scaling. In particular, β_t, β_p, and q are independent of R_o and F_o. The following ranges of the remaining parameters have been included in the following survey:

$$\begin{aligned} &1 \le \alpha < 2 \\ &\alpha - 0.2 \le \beta \le \alpha + 0.8 \\ &2.5 \le A \le 4.0 \\ &1 \le \kappa \le 2 \\ &-0.50 \le d \le 0.75 \\ &0 \le \alpha_J \le \text{code convergence limit } (\approx 1.4) \end{aligned} \tag{10}$$

These include most of the plasmas expected in a tokamak reactor with the exception of doublet-type cross sections.

It is found that it is possible to find equilibria which significantly exceed the Shafranov limit and which seem otherwise reasonable. For currents which approach a skin current distribution; however, the Shafranov limit does not appear to be exceeded. Figure IV-8 shows a graph of β_t vs β_p for several definitions of β_p which appear in the literature[10-12] along with the corresponding relation derived from Equations 1-2. It can be seen that: (1) the old formulas underestimate β_t for a given β_p, and (2) the definitions of β_p differ significantly for high β equilibria, although they agree for $\beta_p \le 1$, which is the upper limit of current experiments. (In this work

$$\beta_p = \left(\frac{2\mu\bar{p}}{\frac{\oint B_p^2 d\ell}{\oint d\ell}} \right)^2$$

$$\beta_t = \frac{2\mu\bar{p}}{B_{to}^2}$$

---

[11] L. E. Zakharov and V. D. Shafranov, Sov. Phys. Tech. Phys. 18, 151 (1973).

[12] J. D. Callen and R. A. Dory, Phys. Fluids, 15, 1523 (1972).

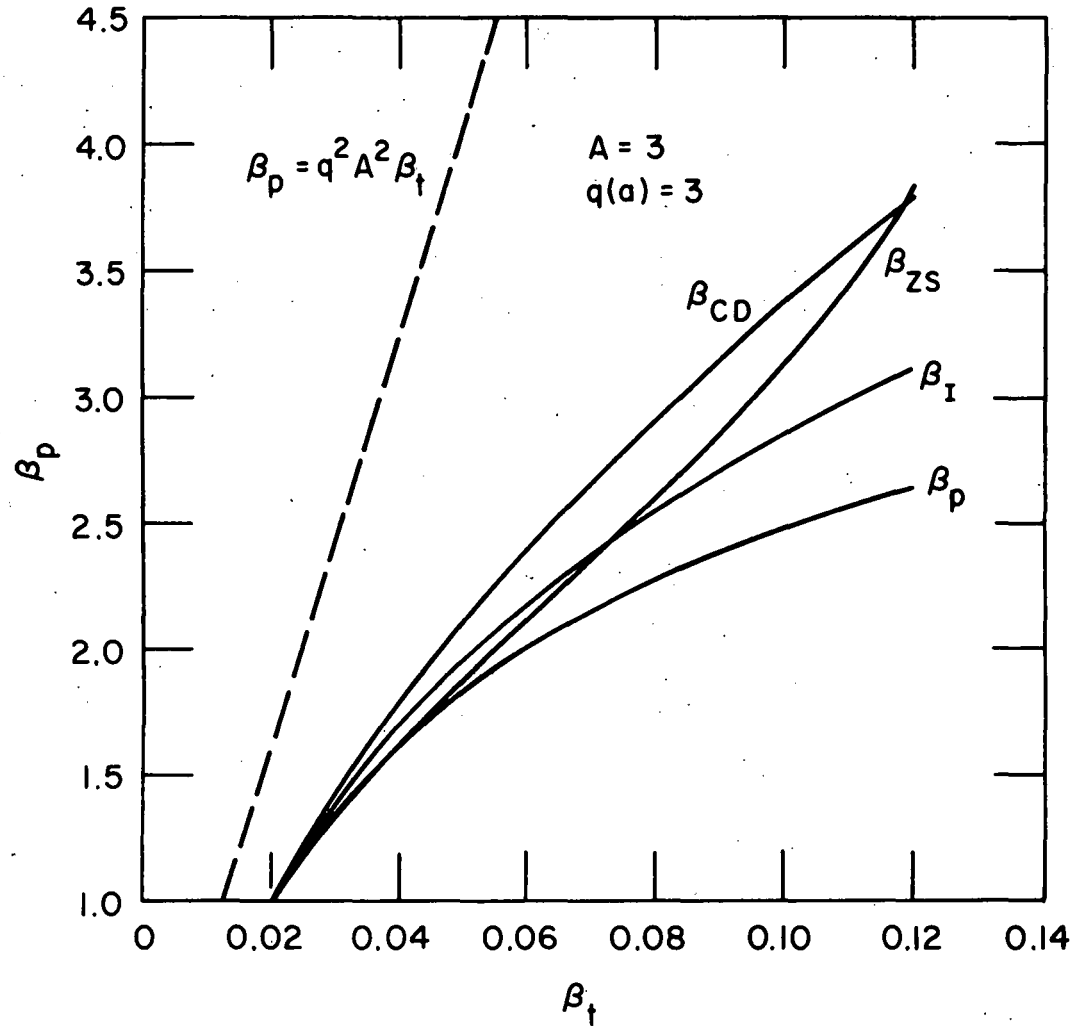

Figure IV-8. Comparison of several common definitions of β_p and the low β, high aspect ratio value.

where $\oint$ is the integral around the boundary contour ($\psi = \psi_\ell$), and B_{to} is the vacuum ($\delta = 0$) field at R_o.)

Figure IV-9 shows q(a) vs β_t for a typical circular case. It can be seen that β_t is limited in two ways: (1) for values of $\beta \approx \alpha$, β_t reaches a maximum, then decreases as q(a) (or alternatively α_J) increases. The decrease in β_t is associated with J_t becoming negative on the inside edge of the cross section; (2) for sufficiently high values of β_t, the code does not converge. This limit, which can be extended by decreasing the grid spacing, is associated with the axis being pushed very close to the outer edge of the plasma, with $q(\psi)$ becoming irregular, and with the onset of current reversal near the inside edge of the plasma and the development of a skin current profile (see Figure IV-10).

It can be seen that high values of β_t are associated with low values of q so that the β_t limit depends how low q(a) can be made in a well behaved plasma. Present experiments indicate this level may be on the order of three; and the plasma current and q profiles are shown in Figure IV-11 for this value of q for a typical circular cross section case. For this case the $\beta_t = 8\%$ cases seem reasonable, but the 12% cases do not, indicating $\beta_t \approx 10\%$ is the upper limit for a circular, A = 3 configuration, more or less independent of pressure profile.

Further, it is found that the upper limit on β_t:

1. decreases with A (for the circular case $\beta_t \approx 12\%$ for A = 2.5, and $\beta_t \approx 6\%$ for A = 4.0),

2. increases with κ (for $\kappa = 1.3$, $\beta_t \approx 10\%$; for $\kappa = 1.6$, $\beta_t \approx 12\%$, and for $\kappa = 2.0$, β_t 18%),

3. is relatively independent of α, and

4. is relatively independent of d.

(Notice that the remaining parameters β and α_J are determined by specifying β_t and q(a).) The actual values of β_t given above, of course, depend on what one considers to be "reasonable". In particular, the bumps in q can potentially be eliminated by tailoring the F or P profiles. Stability considerations will most likely limit β_t to values lower than those given above in any event.

D. Safety Studies of Fusion Reactor Concepts

I. Charak, Reactor Analysis and Safety Division

Work continued this quarter in all three major areas of investigation. In the first wall/blanket safety area, an analysis was performed to estimate the containment building pressurization resulting from a blowdown of the pressurized water primary coolant system. Also, the first wall has been modeled in preparation for transient analyses. Finally, a conservative model, formerly employed in analyzing sodium-spray fires, has been applied to the

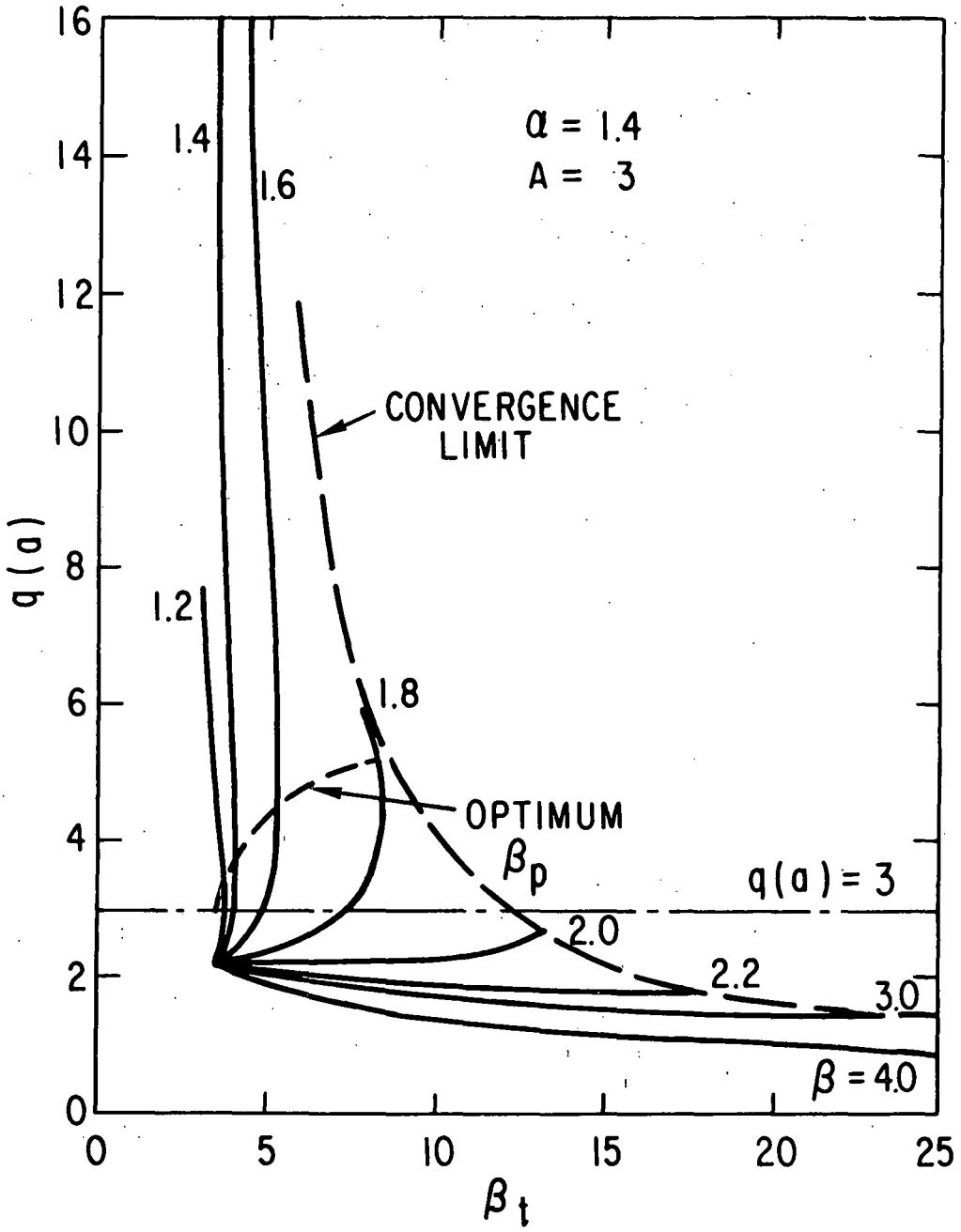

Figure IV-9. The relation between a and β_t for a series of typical, circular equilibria. The curves correspond to different values of β and α_J increases along each curve. (The curves meet at $\alpha_J = 0$.) The "optimum" curve is where β_t peaks for each value of β. The code does not converge for α_J greater than the "convergence limit".

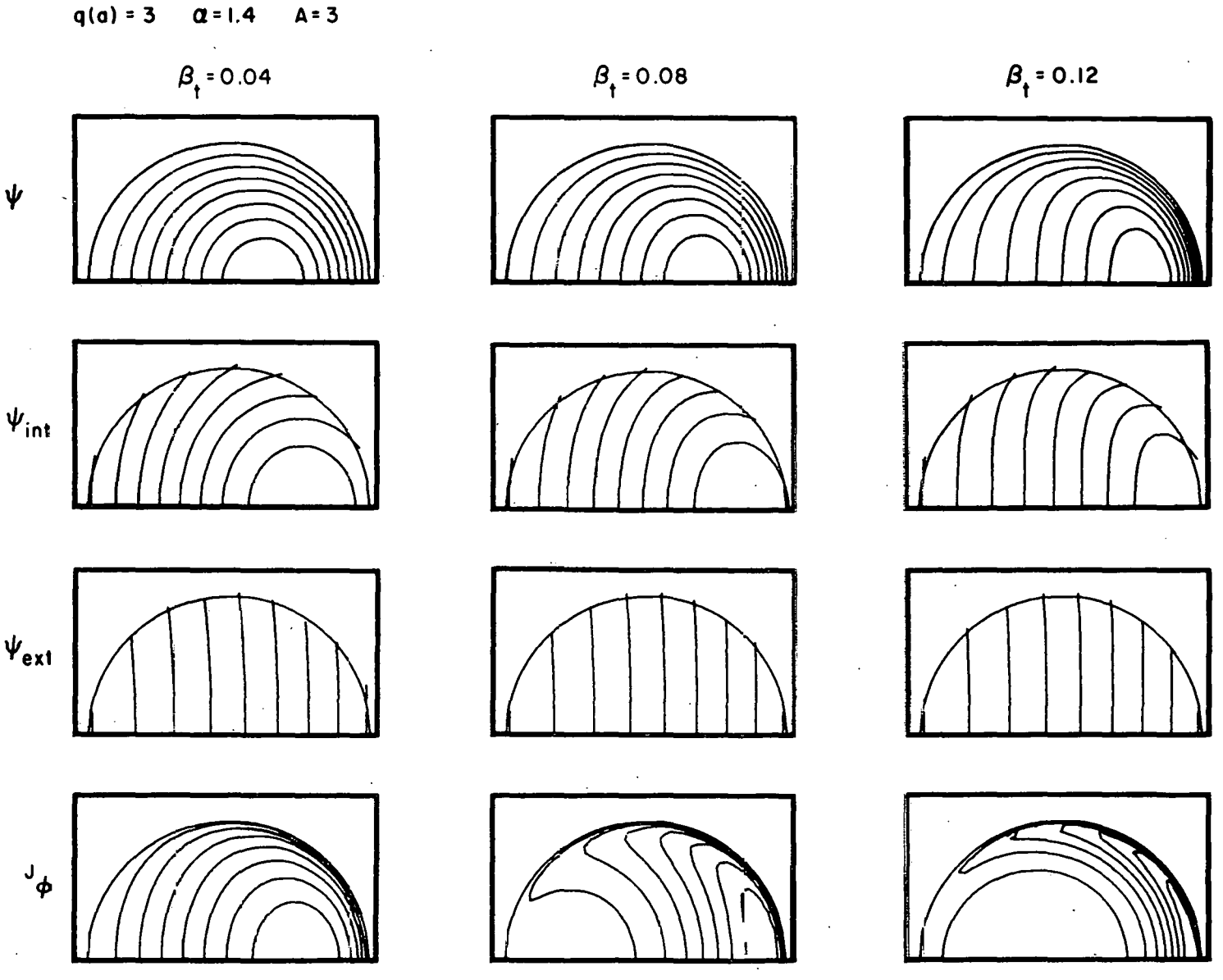

Figure IV-10. The flux surfaces, internal flux surfaces (due to plasma current alone), required external field flux surfaces, and current density profiles for fixed $\varepsilon(a)$ and β_t approaching the "convergence limit".

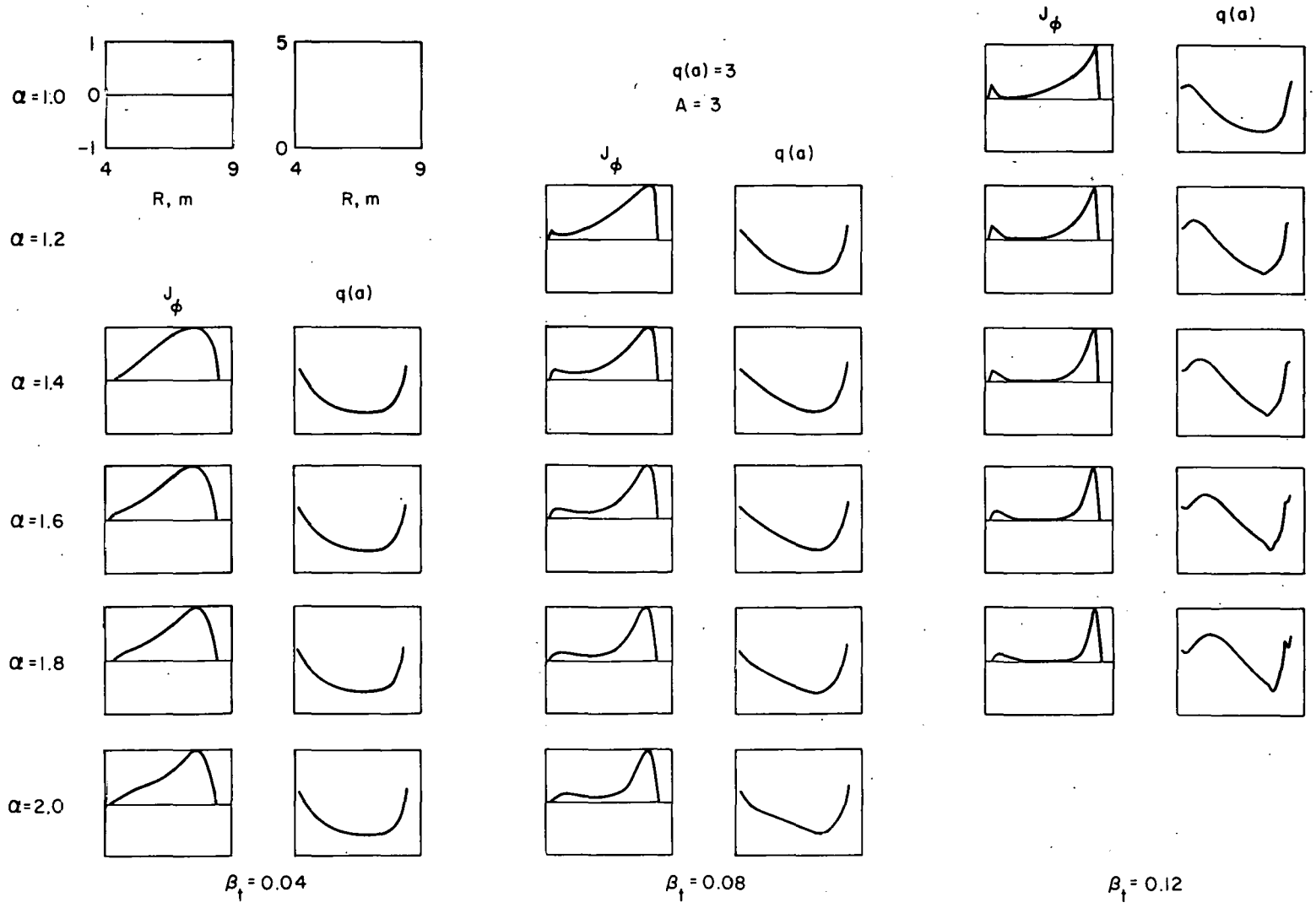

Figure IV-11. Current density and ε along the midplane for a typical circular case as β_t increases. Low values of α correspond to broad pressure profiles, and high values, the sharp ones.

calculation of lithium fire consequences. In tritium safety, analyses of containment building atmosphere detritiation were continued and expanded. Under the magnet safety task, the effect of a rapid plasma quench on the PF coils and power supplies was studied.

1. EPR Containment Building Overpressure Resulting from Rupture of Pressurized Water System

A possible source of pressurization of the EPR containment building is the steam which would result from the blowdown of the first-wall pressurized water coolant system in the event of a system rupture. This pressurization has two effects: loading the building itself and loading the torus and other vessels externally. An analysis of the resulting overpressure has been performed in order to provide the system designers with appropriate design information.

The basic equation used in this analysis simply equates the system internal energy before and after the blowdown. Ignoring heat losses and assuming perfect mixing of the air and steam, we have

$$\frac{Ma}{Mw} C_v T_{a,1} + U_1 = \frac{Ma}{Mw} C_v T_2 + U_{f,2} + xU_{fg,2} \qquad (1)$$

where
- Ma = mass of air
- Mw = mass of water
- C_v = constant volume specific heat of air
- $T_{a,1}$ = initial air temperature
- U_1 = initial specific internal energy of water
- T_2 = final equilibrium temperature of steam-air mixture
- $U_{f,2}$ = specific internal energy of saturated water at T_2
- $U_{fg,2}$ = ΔU from saturated liquid to saturated vapor at T_2
- x = steam quality

Also,

$$x = \frac{\frac{V}{Mw} - v_{f,2}}{v_{fg,2}} \qquad (2)$$

where
- V = building volume
- $v_{f,2}$ = specific volume of water at T_2
- $v_{fg,2}$ = Δv from saturated liquid to saturated vapor at T_2.

Equation (1) is solved iteratively by first calculating the left-hand side which contains only known quantities. The right-hand side is then calculated by assuming a value of T_2, calculating x from Equation 2, and finally calculating the right-hand side of Equation 1. A new temperature is assumed and the procedure repeated until Equation 1 is satisfied. The final value of T_2 is then used in the perfect gas equation to calculate the partial pressure of the air, to which is then added the vapor pressure at T_2 to arrive at the total building overpressure.

The results of this calculation are given in Figure IV-12. The figure uses the ratio Ma/Mw as a parameter. For a building volume of 10^7 ft^3 (the 1976 EPR value) and a water inventory of 20,000 gal, Ma/Mw is about 8. Therefore, for a 2000 psia water system, the equilibrium overpressure is about 2.6 psi. Obviously, similar curves can be constructed covering any range of Ma/Mw.

2. Lithium Fire Analysis

In anticipation of the incorporation of at least one breeding module in the EPR, a preliminary analysis of the consequences of a lithium fire has been completed. The model is the conservative spray burning model used earlier in sodium fire calculations.[13] The reaction considered is

$$2\ Li + 1/2\ O_2 \rightarrow Li_2O + 142\ kcal \qquad (3)$$

The model assumes:

1. infinite reaction rate,
2. heat of reaction apportioned among the nitrogen and remaining oxygen,
3. no heat loss from the system.

Using Glassner's values of temperature-dependent specific heat,[14] a fourth-order polynomial in temperature results when the total heat of reaction is equated to the total available heat capacity. The roots of this equation are then determined using a KAPL code[15] and the resulting building overpressure is calculated using the perfect gas law. No further development of the model is planned at this time.

---

[13] I. Charak and L. W. Person, "SPOOL-FIRE -- An IBM 370/195 Code for the Analysis of Combined Spray and Pool Burning of Sodium," Proceedings of the International Meeting on Fast Reactor Safety and Related Physics, October 5-8, 1976 (to be published).

[14] Alvin Glassner, "The Thermochemical Properties of the Oxides, Fluorides, and Chlorides to 2500°K," ANL-5750 (undated).

[15] J. R. Schmid, et al., "ROPE - Roots of a Polynomial Evaluation," KAPL-M-6540 (April 1, 1966).

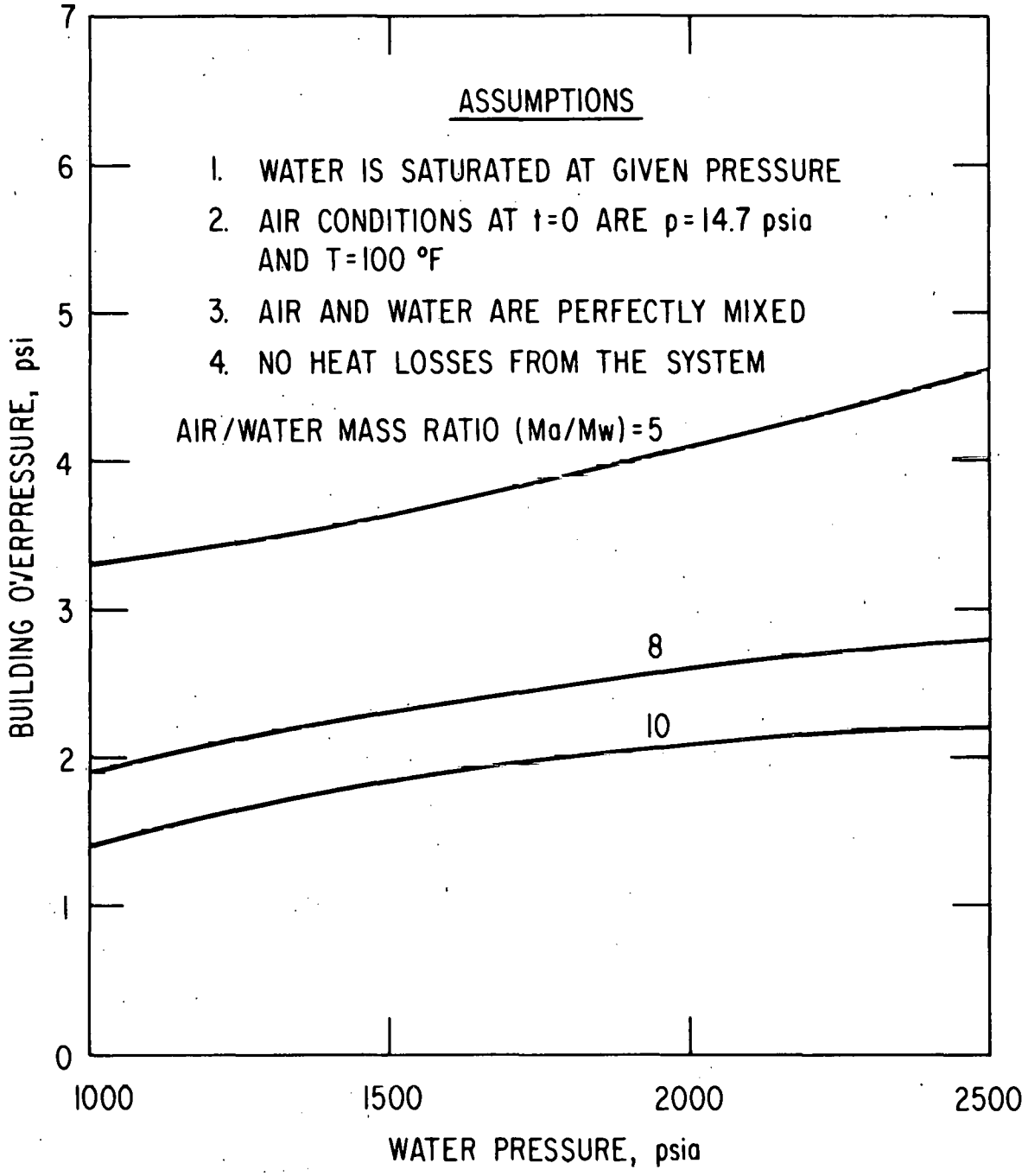

Figure IV-12. EPR containment building overpressure following primary coolant blowdown.

3. Analysis of Tritium Soaking Mechanisms

V. A. Maroni, and R. H. Land, Chemical Engineering Division

Development of the computer code to simulate reaction and soaking mechanisms following massive tritium releases to fusion reactor buildings has continued. The model described in the previous quarterly report[4] has been modified and upgraded to make better use of applicable data from the literature[16-19] and to incorporate mechanisms for return of "soaked" tritium to the reactor building atmosphere. This model now includes terms to account for the reaction of T_2 with moist and dry air in the presence or absence of catalytic surfaces. An option is built into the code to permit the use of (1) data sets such as those reported by Eakins and Hutchinson[16]; or (2) an empirical formalism developed by Galloway, et al.[17] Other features have been built into the model that approximate the rate of return of adsorbed HTO or T_2O and permeated T_2 or HT during, and in particular near the end of, the cleanup operation. The data of Kornacheva, et al.,[19] for the adsorption of water on oxidized and unoxidized iron surfaces have been used to estimate the sticking coefficients in the expressions for adsorption of tritiated water formed during cleanup of a massive tritium release.

Results of soaking calculations for a "base case" scenario involving the cleanup of tritium releases in the range 2 to 200 grams to a 5×10^6 cu ft. room by a 10^4 cfm recirculating air detritiation system are presented in Table IV-6. Also shown in Table IV-6 are the results obtained by varying selected "base case" parameters. As reported in the previous progress report,[4] the amount soaked and the cleanup time are most sensitive to air flow rate. However, inclusion of 20 m^2 of cold surface, which is simulated by a sticking probability near unity coupled with a somewhat higher long term release coefficient (+ 20 m^2 @ < 0° C in Table IV-6), led to the prediction of a considerably extended cleanup time due to the slow back release of adsorbed HTO. Graphical computer output for the "base case" and the case involving the simulated cold surface are given in Figures IV-13 and IV-14.

---

[16] J. D. Eakins and W. P. Hutchinson, "The Radiologic Hazard from the Conversion of Tritium to Tritiated Water in Air by Metal Catalysts," in Tritium, A. A. Moghissi and M. W. Carter, Eds., Messenger Graphics, Phoenix, Arizona, 1973.

[17] T. R. Galloway, A Containment and Recovery System for Fuel-Reprocessing Plants, Lawrence Livermore Laboratory, Report UCRL-78585 (August, 1976).

[18] L. F. Belovodskii, et al., "Oxidation of Tritium in Air Under the Action of Intrinsic Radiation," Atomnaya Energiya, 38, (1975).

[19] G. M. Kornacheva, et al., "The Adsorption of Water Vapor on Iron," Electrokhimiya, 9, 81 (1973).

Table IV-6. Selected Results of Air Cleanup Calculations

Base Case:

Room Volume	5×10^6 cu. ft.
Process Efficiency	1.0
Air Flow Rate	10^4 cfm
R $(T_2 + O_2)$[a]	1.5×10^{-12} $m^3/\mu Ci \cdot min$
R' $(T_2 + H_2O)$[a]	1.5×10^{-11} $m^3/\mu Ci \cdot min$
Stainless Steel at 300°K	2×10^4 m^2
ECPT[b]	50 $\mu Ci/m^3$
HTO, T_2O Adsorption Rate	$1.1 \times 10^{-8}/m^2 \cdot min$
HTO, T_2O Release Rate	10^{-5}/min

Conditions	Release Size (gm)	Amount Soaked (Ci)	Cleanup Time (Hours)
Base Case	200	5.5×10^{-1}	120
	20	7.2×10^{-3}	105
	2	3.8×10^{-4}	85
R = 10^{-11}	20	3.8×10^{-2}	105
R' = 10^{-10}	2	7.4×10^{-4}	85
ECPT[b] = 5 $\mu Ci/m^3$	20	7.2×10^{-3}	105
	2	4.1×10^{-4}	85
+ 20 m^2 @ 300°C	20	6.2×10^{-1}	105
	2	1.8×10^{-1}	85
+ 20 m^2 @ 0°C	20	1.0×10^{1}[c]	100
10^5 cfm	200	4.8×10^{-3}	12
	20	1.9×10^{-4}	11
	2	3.7×10^{-5}	9

a. Values of R and R' (the reaction rate constants for the indicated reaction) taken from Reference 16 are multiplied by a factor of 15 to account for effects of the radiation environment in the reactor building as suggested by Galloway.[17]

b. ECPT = Equivalent Concentration of Permeated Tritium.

c. Final value before oscillations in solver routine at ∿ 300 minutes.

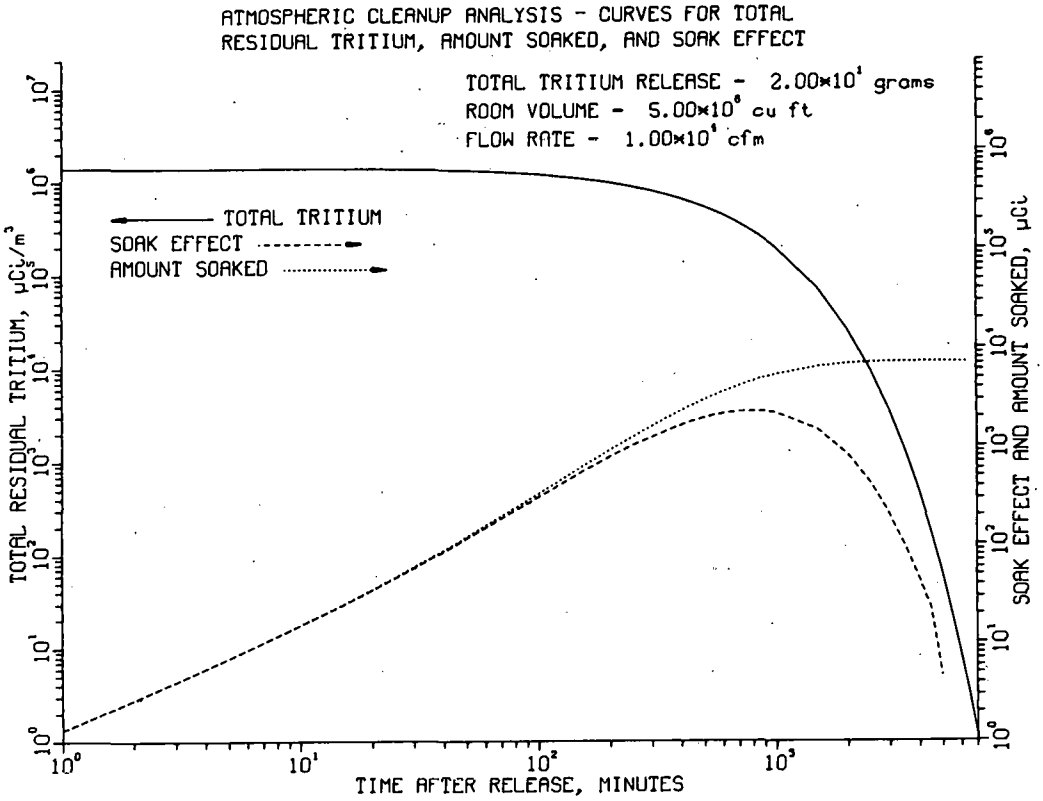

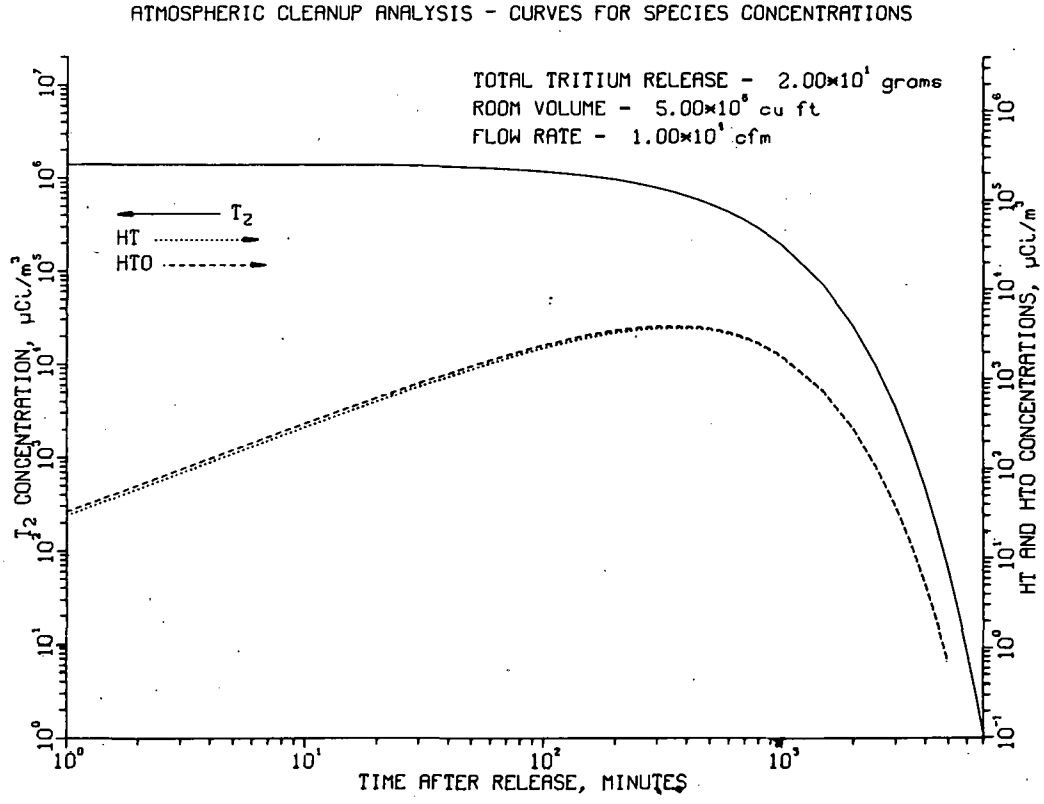

Figure IV-13. Graphical Data for the "base case" Cleanup Scenario (see text).

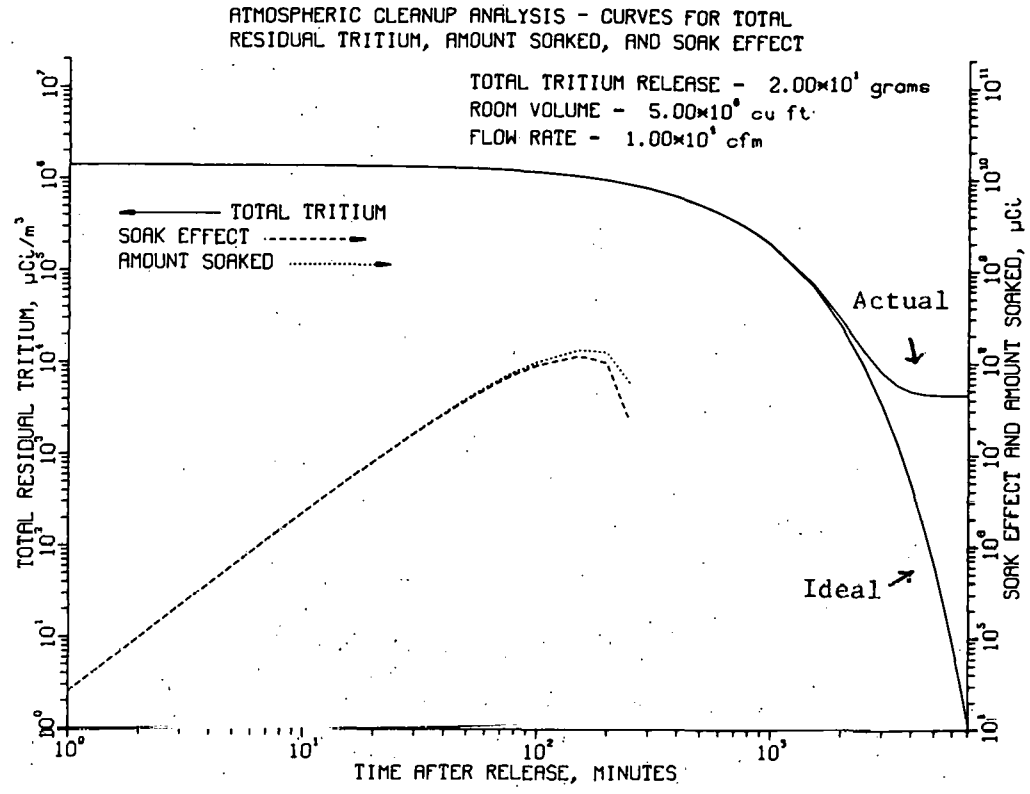

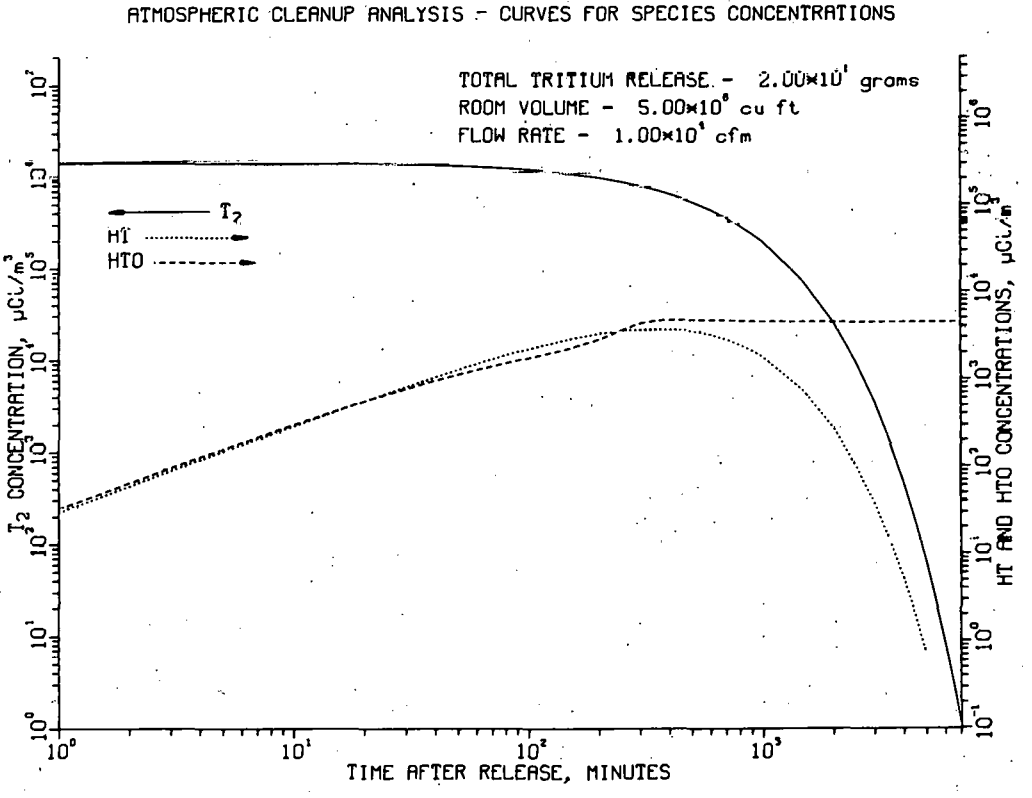

Figure IV-14. Graphical Data for the "base case" modified to include a 20 m^2 Condensing Surface.

The final phases of this study (now underway) will involve cross checking of the formalisms used in the model with the actual computer coded algorithm to verify consistency. We are also investigating the sources of occasional oscillations in the differential equation solver for the amount soaked and the soak effect[4] under certain types of input conditions.

Although the results of the soaking studies described above and in Reference 4 are still considered to be preliminary, several conclusions can be drawn from the work carried out to date. These results may be stated summarily as follows: (1) When the relative humidity is greater than a few percent, the total amount of adsorbed tritiated water is greatly reduced due to surface swamping by H_2O. (2) Exposed elevated temperature metal surfaces ($\gtrsim$ 200°C) represent a major soaking pathway. All thermally hot metal surfaces should be thermally insulated and preferably isolated from the building atmosphere. (3) Exposed low temperature surfaces (< 0°C) are also undesirable. Such surfaces (simulated by using sticking probabilities near unity) need not be large in area to condense large quantities of tritiated water. (4) For rooms in the range 10^6 to 10^7 cu. ft. a 10^5 cfm processor is desirable and 10^3 cfm is inadequate. With judicious selection of building materials, surface preparation procedures, and atmosphere operating parameters, a 10^4 cfm system (a near to state-of-the-art system) could be acceptable.

4. Effect of a Tokamak Plasma Quench on the EF and OH Coils and Power Supplies

L. Turner, Accelerator Research Facilities Division

Because of the inductive coupling between the plasma current and the equilibrium-field (EF) coils and ohmic-heating (OH) coils of a tokamak reactor, there is danger that a sudden disruption of the plasma current could induce currents or voltages in the EF and OH coils large enough to damage the coils or their power supplies. Moreover, because the plasma quench is initiated by plasma instabilities which are not completely understood and are difficult to model, predicting the effects on the coils seems difficult.

However, if there is a suitably designed first wall, the plasma current can be transferred to it. Afterwards, the current in the first wall will decay exponentially, and the OH and EF coils will respond as they would to any other decaying coupled LR circuit.

To be specific, we consider the Argonne 1976 design study for an Experimental Power Reactor (EPR).[20] Relevant parameters from that design appear in Table IV-7.

The first wall is made of stainless steel and is 2 cm thick. It incorporates two insulating current breakers, which prevent the OH coils from inducing eddy currents in the first wall. Such eddy currents would partially screen the plasma region from the flux change provided by the OH coils and would also add unnecessary power consumption. In operation, the current breakers must withstand a voltage of a hundred volts or so.

---

[20] W. M. Stacey, Jr., et al., "Tokamak Experimental Power Reactor Conceptual Design," Argonne National Laboratory, ANL/CTR-76-3 (August, 1976).

Table IV-7. Parameters from ANL 1976 EPR Design*

I_p	7.58 MA	The plasma current
I_{FWO}	7.58 MA	Initial value of I_{FW}, the current in the first wall; assumed equal to I_p
I_{OHO}	80 kA	Initial value of I_{OH}, the current in the OH coils
I_{EFO}	80 kA	Initial value of I_{EF}, the current in the EF coils
L_P	11.56 μH	Inductance of plasma
L_{FW}	11.56 μH	Inductance of first wall; assumed equal to L_p
L_{OH}	0.48 H	Inductance of OH coils
L_{EF}	0.52 H	Inductance of EF coils
$M_{OH-P} = M_{OH-FW}$	= 570 μH	Mutual inductance between OH coils and plasma (or first wall)
$M_{EF-P} = M_{EF-FW}$	= 629 μH	Mutual inductance between EF coils and plasma (or first wall)
M_{OH-EF}	= 7894 μH	Mutual inductance between OH and EF coils
R_{FW}	= 96 μΩ	Resistance of first wall; resistance of current breakers assumed negligible

* W. M. Stacey, Jr., et al., "Tokamak Experimental Power Reactor Conceptual Design," ANL/CTR-76-3 (1976).

However, if the plasma current quenches in, say, 10 ms or less, there will be 4000 V or more across each current breaker. Perhaps the breakers can be designed to accept that; but if they did, the voltage would show up across the coils or across the elements of the blanket and shield. If, instead, the current breakers are designed to break down under this high voltage to a resistance of a few micro-ohms, the entire plasma current can transfer to the first wall. Because the first wall closely surrounds the plasma, its coupling with the coils is the same as that of the plasma; and the currents and voltages in the coils will initially be unaffected by the quench.

Afterwards, the first wall and the coils will respond as three inductively coupled circuits. Using the values and definitions from Table IV-7, we find that if the power supplies were to hold I_{OH} and I_{EF} constant, the current in the first wall would decay as

$$I_{FW} = 7.58 \exp (-8.3\ t)\ MA$$

with time constant 1/8.30 = 0.12 s. That current would induce exponentially decaying voltages in the OH and EF coils with initial magnitudes of 36 kV and 40 kV, respectively.

The power supply protection circuits will prevent such large voltages developing. Instead, they will throw the coils into persistent mode, in which the flux through each coil remains constant. In that case the currents will be given by

$$I_{FW} = 7.58 \exp (-9.46\ t)\ MA,$$

$$I_{OH} = [71.1 + 8.9 \exp (-9.46\ t)]\ kA,$$

$$I_{EF} = [71.0 + 9.0 \exp (-9.46\ t)]\ kA.$$

Note that because of the negative coupling between the coils and the first wall, the currents I_{OH} and I_{EF} will actually decrease as I_{FW} decays.

The decay of the current heats the first wall by about 10°C in about 0.1 s.

Whether the current breakers must recover spontaneously after they break down or whether they should be replaced depends on how often a plasma quench is expected to happen.

If the plasma quench takes much longer than 10 ms, the current breakers will not break down; but over that long time interval the coils will respond to the plasma current as they otherwise would to the first-wall current.

In conclusion, the normal protection circuits for the OH and EF coils and power supplies will protect them from a plasma current quench if the current breakers of the first wall are designed to break down to a resistance of a few micro-ohms when they experience a few thousand volts potential difference. The design of such current breakers should be included in the design of the first wall of a tokamak reactor.

V. MAGNETIC SYSTEMS

A. Energy Storage and Transfer Program

R. Fuja, R. L. Kustom, R. P. Smith, R. Wehrle, Accelerator Research Facilities Division

An inductor-convertor (IC) bridge circuit has been proposed for the TEPR[1] EF coil supply and a novel cylindrical homopolar generator system for the OH coil supply. Experimental model devices for both of these systems are under development so that the utility of each for application to the TEPR can be experimentally assessed.

A three-phase IC bridge with a digital controller has been constructed to model the EF-coil power supply. Two superconducting solenoids were constructed (Figure V-1), one to function as the TEPR storage inductor and one as the EF coil. The two identical coils store 125 kJ each at 250 Amperes and are designed to permit charging at voltages corresponding to $\dot{B}$ = 1 T/s without degrading the ultimate quench limit of the superconductor. The coils each contain 6000 turns of a 1 mm diameter copper-stabilized filamentary NbTi conductor, and each coil reaches the short sample limit of 4.2 T when charged at 150 V. This charging voltage was the highest available during the magnet tests and corresponds to $\dot{B}$ = 0.6 T/s. The two 34 kilogram coils are each wound on an epoxy-fiberglass bobbin and are suspended with their axes mutually perpendicular in a single large cryostat for ease of cryogenic operations. The orientation of the coils ensures no inductive coupling, and a rigid aluminum frame resists the torque tending to align the coils when both carry current.

A three-phase IC bridge[2] was constructed (Figure V-2) to transfer energy from one model coil to the other. A digital control unit provides switching pulses for a set of six SCR's on the supply side of the bridge and six SCR's on the load side of the bridge. A valid switching sequence of the SCR's on the supply side of the circuit commutes the capacitors in such a way that a three-phase voltage is created across the supply coil. A similar switching sequence across the load SCR's, but differing in time by an overall phase ϕ creates a voltage across the load coil. Only a small fraction of the energy stored in the supply coil resides in the commuting capacitors at any one time. By varying the phase ϕ, the net rate at which energy is transferred from the supply coil to the load coil can be varied. The sign of ϕ governs the direction of energy flow. The model bridge permits a choice of ϕ, and suitable initial conditions of the inductors and capacitors, to be preset. The digital controller then switches the SCR's at a fixed frequency in a fixed sequence.

Observed voltage waveforms on the commuting capacitors and the inductors at the beginning of a discharge cycle agree with those calculated by a computer

---

[1] W. M. Stacey, Jr., et al., "Tokamak Experimental Power Reactor Conceptual Design," Argonne National Laboratory, ANL/CTR-76-3 (1976).

[2] R. L. Kustom, et al., "The Use of Multiphase Inductor - Convertor Bridges as Actively Controlled Power Supplies for Tokamak EF Coils," Argonne National Laboratory, ANL/FPP-TM-78 (1976).

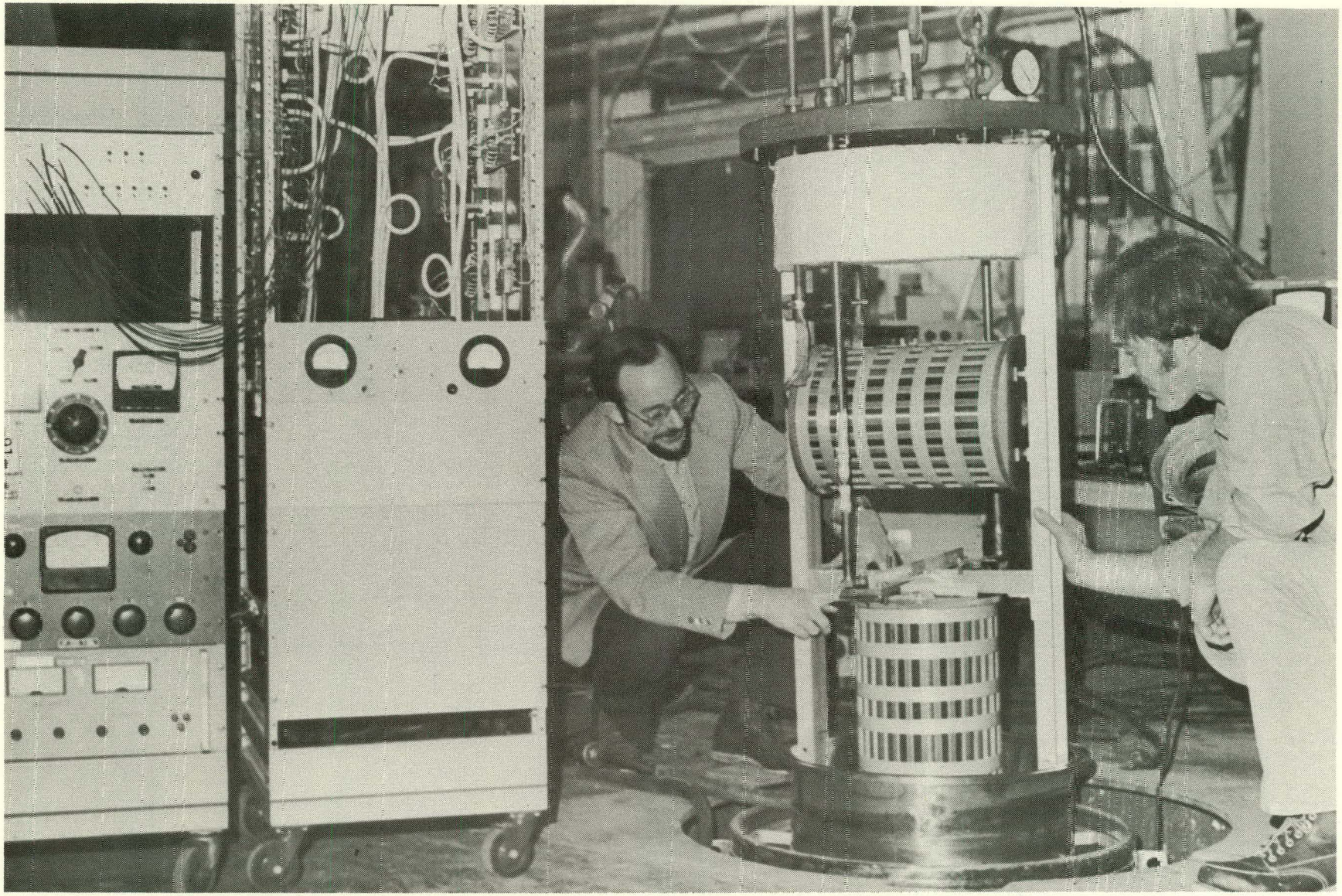

Fig. V-1. Photograph of an inductor-convertor model consisting of two 100 kilojoules coils, an array of 20 thyristors, and a digital controller.

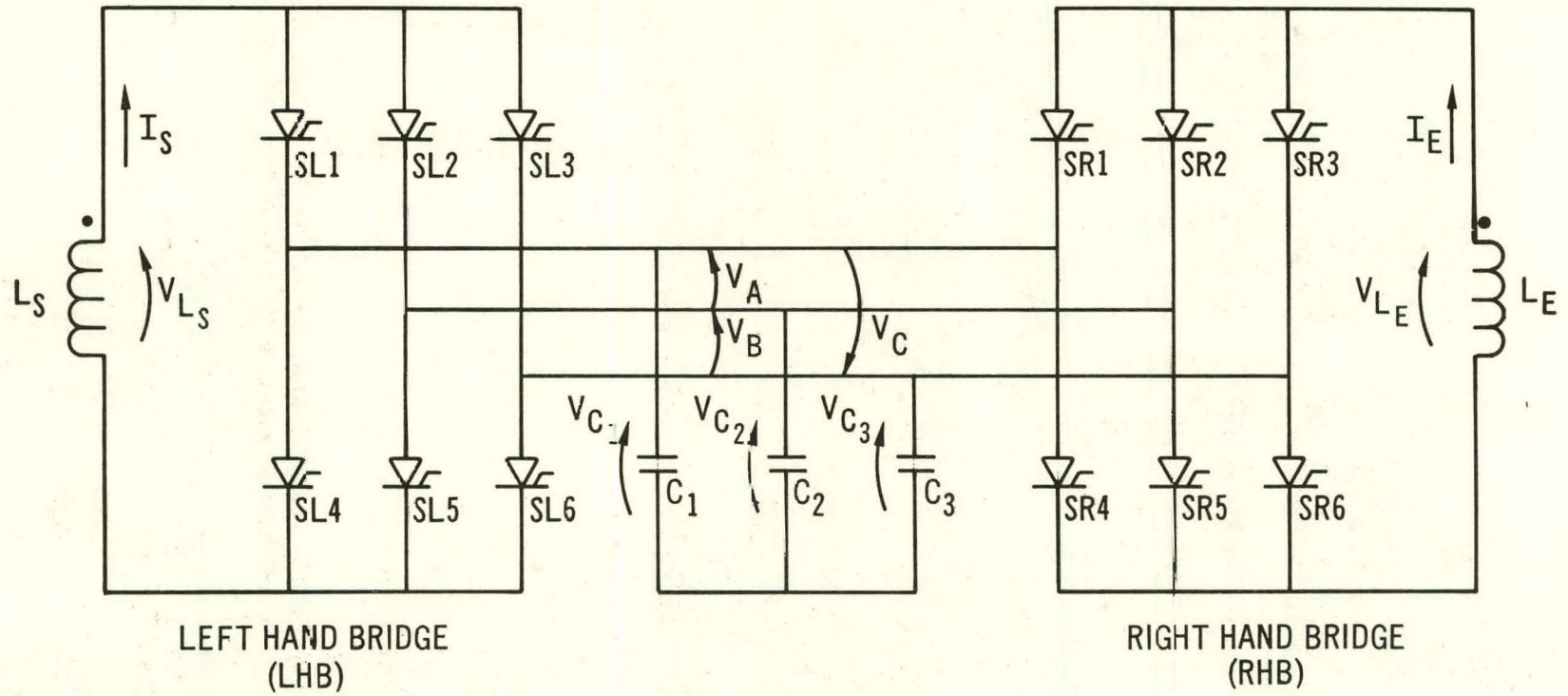

Fig. V-2. Three-Phase Inductor Convertor Bridge Circuit Diagram for the EF Coil System.

program which integrates the circuit equations forward in time and displays the desired voltages and currents. A fraction of the stored energy has been transferred to the load coil, and the behavior of the bridge with respect to various unbalances is under study. An on-line microprocessor is being interfaced to the circuit to permit fast data logging, and ultimately dynamic control of the phase d for optimum energy transfer throughout a complete transfer cycle. The detailed switching behavior of SCR's during turn-off is being studied and an equivalent circuit of an SCR is being created so that the losses in the IC bridge can be investigated in the experimental model.

A model homopolar generator (HOPE I) is under construction (Figure V-3) that will permit the study of the mechanical feasibility of a cylindrical rotor energy storage device. A single cylindrical drum rotating on a vertical axis, with dimensions scaled to the Counter Cyclonic Generator (CCG) of the TEPR OH-coil power supply will enable the study of air bearing operation in the presence of considerable radial expansion of the rotating cylinder. The model is made with an aluminum cylinder 0.132 m long with an inside diameter of 0.254 m and a wall thickness of 3.18×10^{-3} m. When the cylinder rotates with an angular velocity of $\omega = 2340$ radians per second it will store 40 kJ energy and there will be 2.58×10^{8} N/m^2 hoop stress in it.

A conventional magnet has been modified with special pole tips and a central support yoke to provide a radial field at the surface of the cylinder when the cylinder is mounted on an air bearing system fixed to the central support yoke. When the magnet is excited to 1.5 T, the cylinder will have a capacitance of 21.3 farads and will develop 61 volts at peak angular velocity. An inductor, representing the TEPR OH coil, has been obtained which has an inductance of 13.6 mH and can store 40 kJ at 2425 amperes. The single rotating cylinder is capable of reversing this current in the inductor in 1.7 seconds.

The air bearing system of HOPE I is potentially simpler than that required by a horizontal axis machine since the weight of the rotating drum acts only axially and need not be supported radially. Conventional copper-carbon brushes will bear on a copper surface plated onto the upper and lower edges of the aluminum cylinder. The brushes will be loaded against the cylinder with an air jet system for uniform electrical contact.

The assembly of the Hope I cylinder homopolar machine will be completed in the next few weeks and it is foreseen that meaningful results from the device will be available shortly thereafter.

B. Ion Sources

A substantial negative ion source development program is in progress under DPR support. Because of the relevance of this work to neutral beam injections for fusion, progress will be reported in this document from time to time.

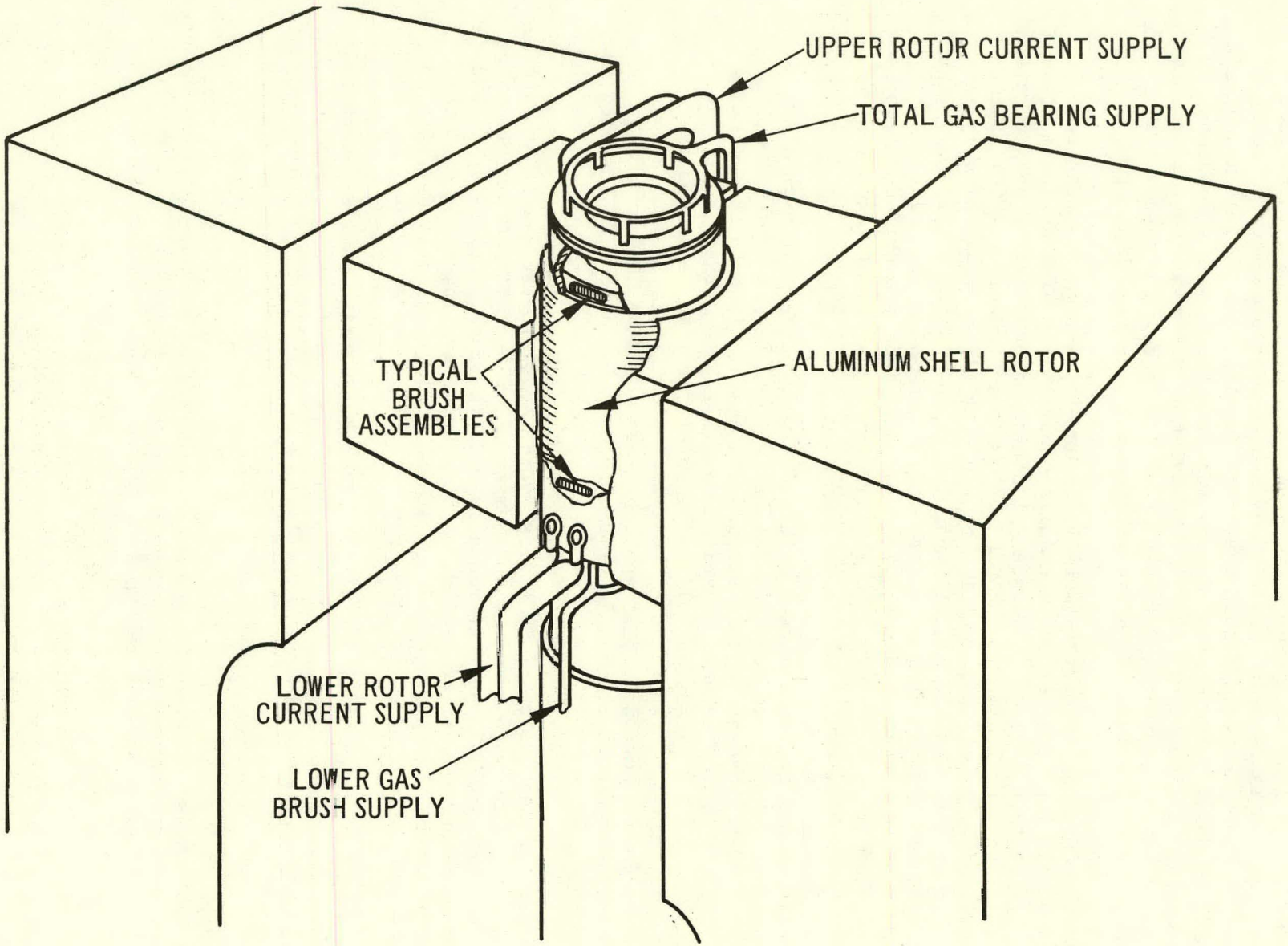

Figure V-3. Counter cyclonic generator - HOPE 1

1. Negative Ion Source Development

a. Charge Exchange H^- Ion Sources

J. A. Fasolo and H. R. Hiddleston, Accelerator Research Facilities Division

The new 30 Hz source assembly has been put into operation and has produced 9.6 mA of H^- beam at 30 Hz with the same three aligned grids used in the original assembly. This current exceeds the 8.8 mA obtained with two aligned grids and the 7.3 mA obtained with three grids in the original assembly.

The discharge geometry of the present assembly differs from, and is evidently better than the original discharge geometry, which is now used in the operational source[3] for direct H^- injection into the Zero Gradient Synchrotron (ZGS). An assembly drawing of the operational source is shown in Figure V-4. The geometry of the remainder of the original 30 Hz source, still used in the new assembly, is shown in Figure V-5.

The inside diameter of the large cylindrical portion of the new intermediate electrode is 5.65 cm, 2.00 cm larger than that of the original electrode of Figure V-4. A water-cooled, oxygen-free high conductivity (OFHC) liner for the intermediate electrode has an inside diameter of 4.68 cm and is itself lined with two 0.038 cm thick heat shields made from Type 304 stainless steel sheet stock. The heat shields were "pebbled" with a center punch to minimize thermal contact of the shields with each other and with the water cooled liner. The OFHC liner extends into the conical portion of the intermediate electrode, where it is lined with two conical stainless steel heat shields. The heat-reflecting liners serve three purposes: they present a cleaner first wall surface, one containing less carbon and oxygen than the mild steel of the intermediate electrode, to highly reactive atomic ions and neutrals, thus reducing plasma contamination; they reduce the heater current necessary to obtain the required cathode temperature, thus extending heater life; and, since the probability of recombination of atomic neutrals and ions on a surface decreases as the temperature increases, they increase the H^+ fraction of the ion beam extracted from the plasma by providing a surface heated to a high temperature by electron and ion bombardment.

The 30 Hz source has been disassembled and stainless steel liners are being installed in Anode II and in the source grid electrode (see Figure V-5) to raise the temperature of surfaces exposed to plasma in those regions of the source. The feasibility of applying a thin coating of aluminum oxide to the portion of the multiaperture source grid exposed to the plasma is being investigated. A sound ceramic coating on this surface, and on other nearby first wall surfaces at the same potential would, in conjunction with heat-shielding elsewhere, reduce recombination to a minimum and maximize the H^+ fraction of the ion beam.

---

[3] J. A. Fasolo, "H^- Source Development at Argonne," Proc. 1977 Particle Accelerator Conference, to be published in Trans. on Nucl. Sci. of the IEEE.

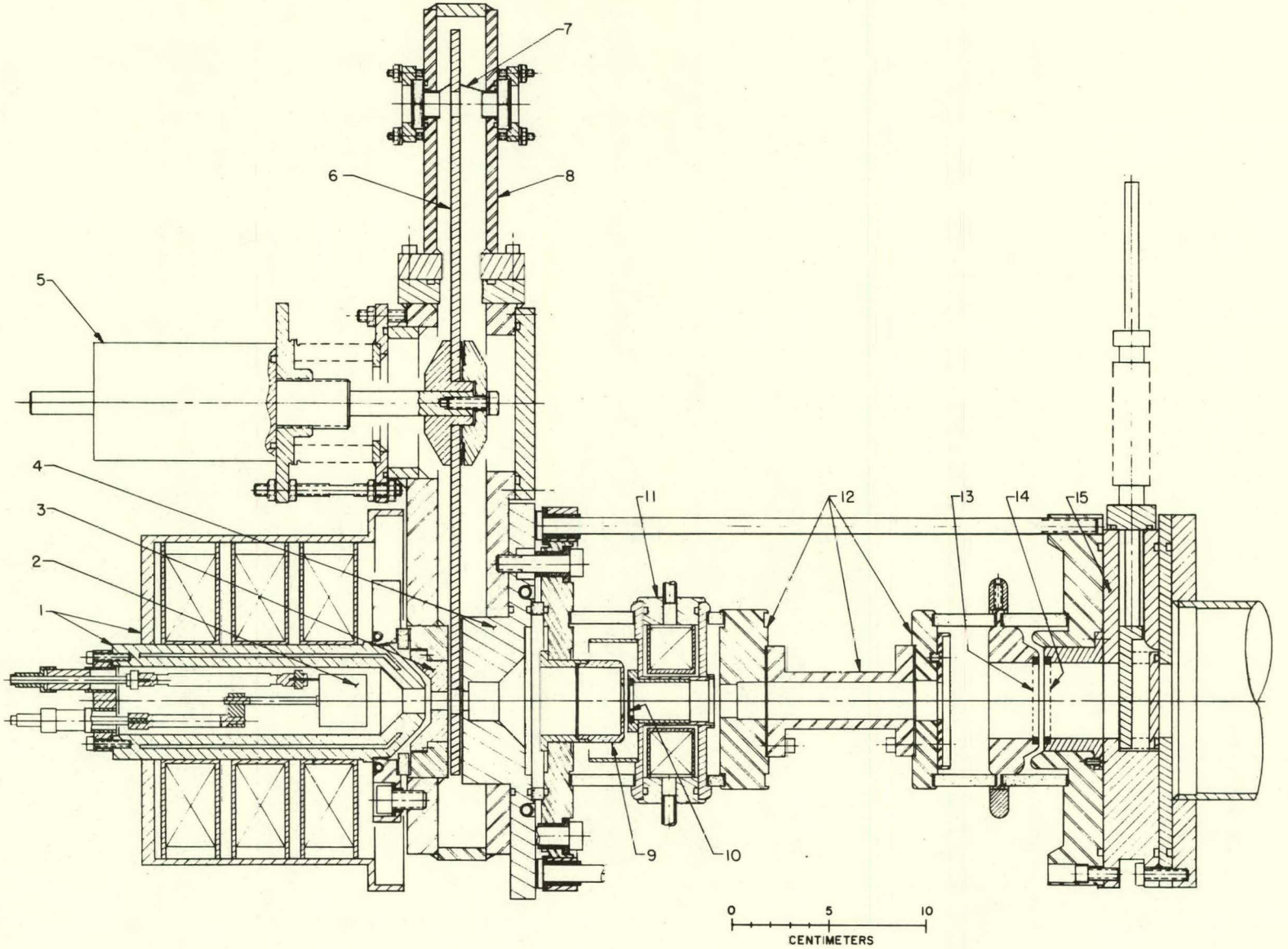

Figure V-4. Operational H^- Source Assembly. (1) Intermediate electrode and flux return. (a) cathode. (3) Anode I. (4) Anode II. (5) Ferrofluidic drive unit. (6) 30 Hz gas shutter. (7) brushes. (8) Valve housing. (9) Source grid. (10) Extractor grid. (1) Field shaping magnet (m-2). (12) Charge exchange cell. (13) Suppressor grid. (14) Grounded grid. (15) Isolation valve.

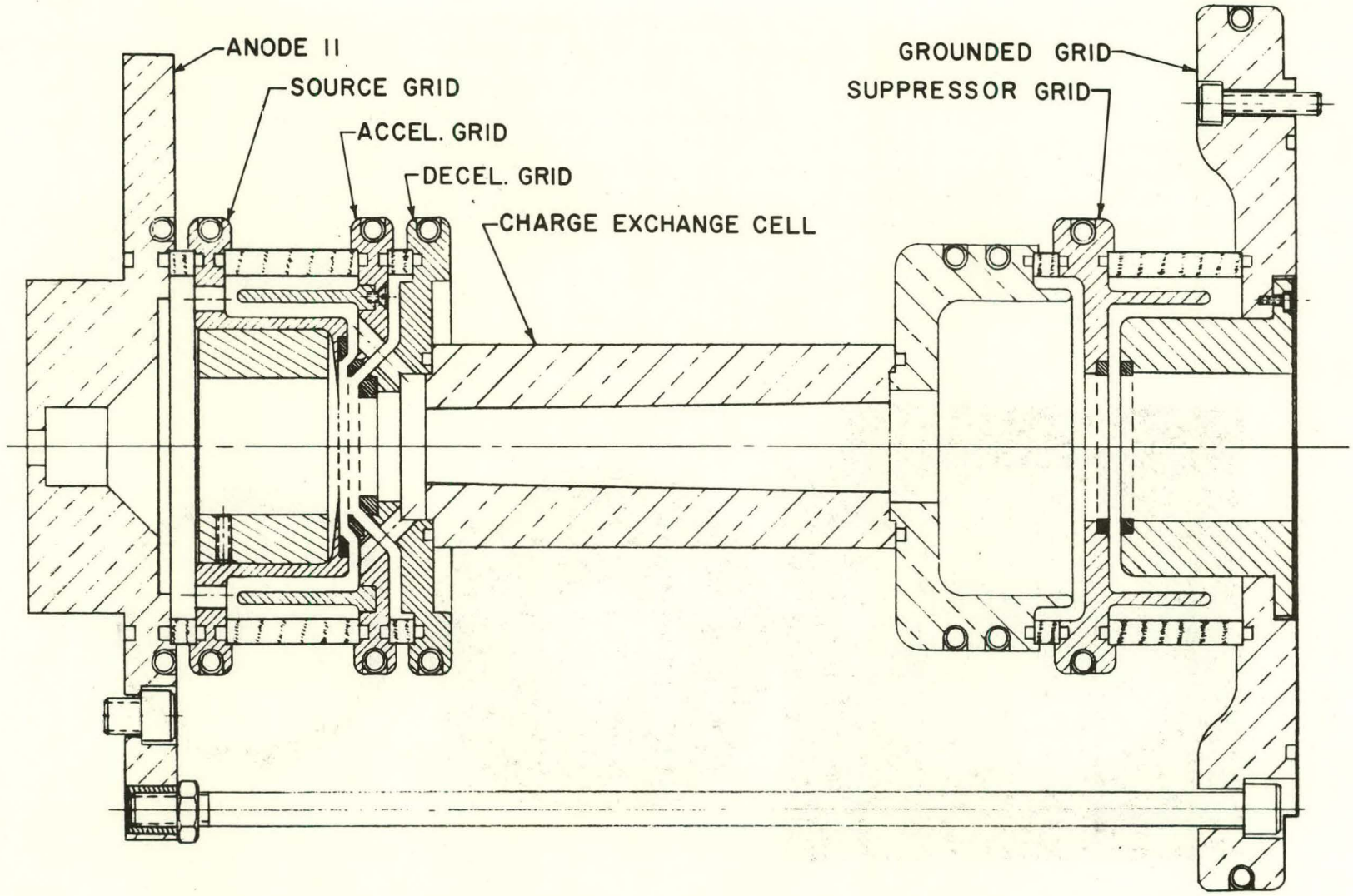

Figure V-5. Tandem-Acceleration Subassembly of the 30-Hz Source.

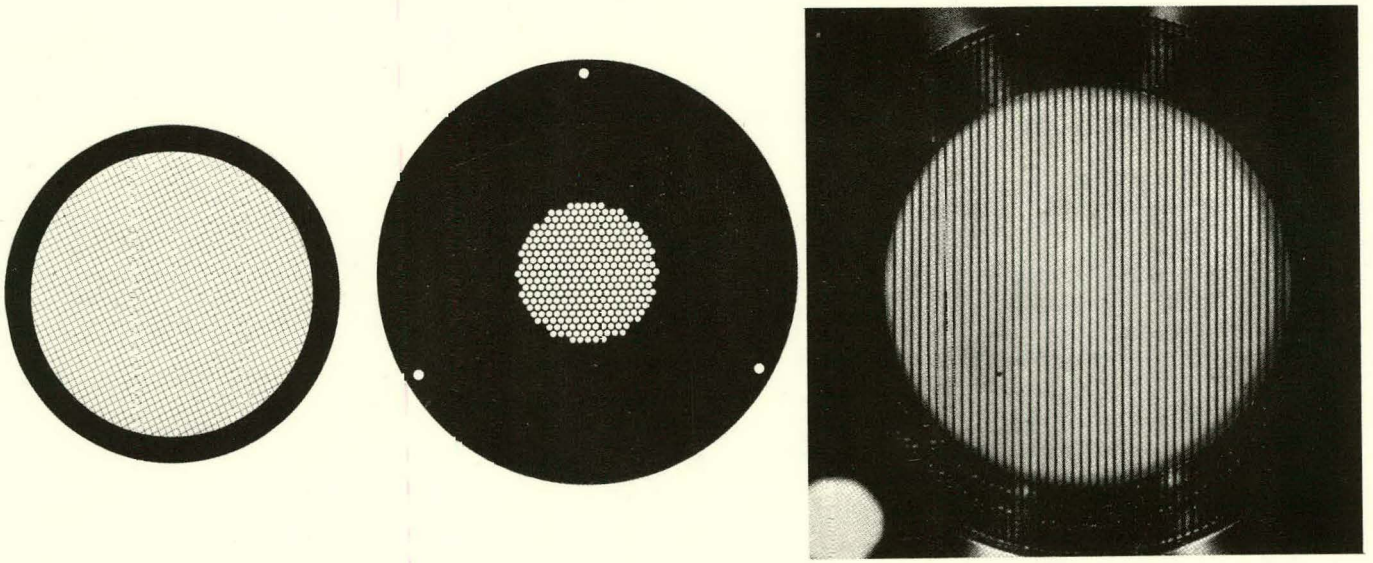

Figure V-6. a) Parallel-ribbon W-3Re extraction grid of the operational H^- source (enlarged x 3.31); b) light transmission through aligned Cu-W source and extractor grids of the 30 Hz source (grids separated by double-faced tape 2.76×10^{-3} cm thick); c) light transmission through W-3Re suppressor or grounded grid (used in either source).

Grid misalignment and uncontrolled thermal expansion (oil canning) may account for a lower than expected beam current and a rate effect which results in a decreased beam current as the pulse rate is increased. A new set of two grids has been fabricated and given a slightly spherical shape to give the sort of controlled thermal expansion that has been achieved in ion thrusters and CTR ion sources. The technique for making grids has improved considerably and much better alignment is expected with the new set of grids. Light transmission through these grids, separated by 2.76×10^{-3} cm thick double-faced tape is shown in Figure V-6, which also shows the W-3 Re parallel-ribbon extractor grid used in the operational source and a W-3 Re wire-screen grid, which serves as a spare for the suppressor or grounded grid of either of the source assemblies.

Automatic controllers have been installed to regulate the temperature distribution in the recirculating version of the sodium vapor jet which is being developed for use with a modified version of the 30 Hz source. The new duct connecting the de Laval nozzle to the cell has been built and installed. This duct was designed to reduce end losses by lowering the temperature of the portion of the duct within line-of-sight of the cell ends. Tests conducted since the duct was installed indicate that normal recirculation is not being achieved. Further tests are being conducted to determine the cause of this problem.

b. Direct Extraction H^- Source

J. A. Fasolo, Accelerator Research Facilities Division

Direct extraction surface plasma sources of the type developed by Belchenko, Dimov and Dudnikov[4] are potentially capable of providing the beam intensity and duty cycle required of ion sources for 30 Hz booster injection into the ZGS and 60 Hz injection into IPNS, an intense pulsed neutron source, which will be discussed in the next section. One version of the surface plasma source has produced $\sim$ 1A of H^- at a 1 Hz rate, with a pulse length of 1 MJ. Another version, using a Penning discharge geometry,[5] has produced more than 100 mA of H^- at 100 Hz for pulse lengths of $\sim$ 200 μs and thus has exceeded the current and pulse requirements for the 30 and 60 Hz sources but falls short of the required pulse length of 1 MJ.

A Penning type surface plasma source has recently been built at Los Alamos[6] according to the design of Reference 5 and is being developed for H^- injection into the LASL 800 MeV linac. The source has produced a 700 μ/s pulse with a current of 100 mA at a 7 Hz rate.

---

[4] Yu. I. Belchenko, G. I. Dimov and V. G. Dudnikov, Preprint IYaF 66-72 Novosibinsk (1972). UCRL-Trans-10672.

[5] V. G. Dudnikov, "Surface-plasma Source of Penning Geometry, IV U.S.S.R. National Conference on Particle Accelerators, Moscow, 1974.

[6] P. W. Allison, "A Direct Extraction H^- Ion Source," Proc. 1977 Particle Accelerator Conference, to be published in Transactions on Nuclear Science of the IEEE.

A duplicate of this source is being built at Argonne, using drawings provided by Los Alamos. The Argonne source, after initial testing, will be modified to extend the duty cycle and reduce gas consumption; it will be developed in parallel with the 30 Hz charge exchange source as a possible alternative to the latter source for 30 Hz booster injection into the ZGS and ZING, an intense neutron source.

c. IPNS H^- Source

J. A. Fasolo, Accelerator Research Facilities Division

Argonne National Laboratory has received funds for construction, planning and design of an Intense Pulsed Neutron Source (IPNS) which will be used for basic research in the study of condensed matter. The IPNS H^- source development effort for this fiscal year has the following objectives:

1. To study and evaluate sources which show promise of being able to deliver 50 mA of H^- ions to a linac in 1 ms pulses at a 60 Hz rate.

2. To identify and seek solutions to problems which cause existing sources to fall short of the requirements for an IPNS source.

3. To do a conceptual design study for an H^- injector.

4. To do a detailed design and prepare construction prints for an IPNS H^- source test stand and a prototype source.

VI. APPLIED PLASMA PHYSICS

A. Multispecies Transport In Tokamaks

C. Boley, Applied Physics Division

In a recent article, S. P. Hirshman and D. J. Sigmar established the neoclassical transport theory of a tokamak plasma consisting of several species in the low-to-intermediate collisionality regime (the banana-plateau regime) and also a single species in the collisional (or Pfirsch-Schlüter) regime.[1] More recently, E. Gelbard and S. Hirshman have shown how the results can be generalized so as to apply to a plasma with any number of Pfirsch-Schlüter species.[2] In these papers it is assumed that the mass of every Pfirsch-Schlüter (P.S.) species is large in comparison with the mass of every banana-plateau (B.P.) species. The results constitute the most general neoclassical transport expressions yet available. Consequently, it is important to incorporate them into the Argonne 1-D plasma transport code, which at present is equipped to handle only a P.S. plasma. The results are now being cast into a form suitable for coding. In practice, the procedure is rather involved, and among the problems which arise are the following:

1. For each element $L_{\sigma\sigma'}$ of the transport matrix there are four expressions, corresponding to the two possible collisionality regimes (B.P. or P.S.) of each of the two species, σ and σ' (taking $\sigma \neq \sigma'$). The collisionality of a species can vary with spatial location, since it is a function of the plasma composition. For continuity, therefore, a smoothing procedure has been devised whereby $L_{\sigma\sigma'}$ is written as the weighted sum of the various possibilities, with the weight depending on the collisionalities. There also occur numerous internal sums which, in principle, are to be taken over those species in a particular collisionality regime. The sums are now taken over all species, with appropriate weights.

2. The B.P. transport expressions involve complicated energy integrals, which contain parameters depending on the local plasma composition. It would be much too time-consuming to evaluate the integrals numerically whenever they are needed. The most reasonable approach appears to be an approximate evaluation via the partitioning of energy space into banana and plateau regimes. This would be similar to the approximation introduced by Tsang and Callen[3] in a simpler context.

3. The results of References 1 and 2 do not apply when there is a P.S. species less massive than any one of the B.P. species. Although this situation might not be expected to occur typically, a way of handling it must be developed.

---

[1] S. P. Hirshman and D. J. Sigmar, Phys. Fluids 20, 418 (1977).

[2] E. M. Gelbard and S. P. Hirshman, submitted to Phys. Fluids.

[3] K. T. Tsang and J. D. Callen, Phys. Fluids 19, 667 (1976).

B. Atomic Data for the Resonance Transitions of the Sodium Isoelectronic Sequence

Y. K. Kim, Radiological and Environmental Research Division

Excitation energies, oscillator strengths (f values) and electron-impact cross sections in the Bethe approximation[4] have been computed from the relativistic Hartree-Fock wavefunctions for the 3s → 3p and 3s → 4p transitions of Na-like ions. The excitation energies and oscillator strengths show qualitatively similar trends as those seen in the Li-like ions;[5-7] namely, (a) f values for the $3s_{1/2} \rightarrow 3p_{1/2}$ transitions decrease monotonically as the nuclear charge Z increases, (b) f values for the $3s_{1/2} \rightarrow 3p_{3/2}$ transitions increase drastically for higher Z because the excitation energies increase from relativistic effects, and (c) f values for both $3s_{1/2} \rightarrow 4p_{1/2}$ and $3s_{1/2} \rightarrow 4p_{3/2}$ transitions show slight departure from nonrelativistic values.

The Bethe cross sections, which represent the leading terms of the plane-wave Born cross sections, show 20 ∿ 40% reduction (as compared to the nonrelativistic Bethe cross sections) owing to two different relativistic effects. The first one is the reduction in the geometric cross section of the ion due to the relativistic contraction of the valence orbitals. The second one is the reduction in the range of allowed momentum transfers due to the relativistic increase of the excitation energies, particularly for the $3s_{1/2} \rightarrow 3p_{3/2}$ transitions. We found that the latter is far more important than the former. This implies that relativistic excitation energies should be used in cross section calculations based on more sophisticated theories. Otherwise, the error introduced by incorrect momentum ranges could reduce whatever improvement gained by using superior collision theories.

Details of the relativistic and nonrelativistic data are presented in Reference 8, and a summary has been reported at the American Physical Society Topical Conference on Atomic Processes in High Temperature Plasmas (February 16-18, 1977, Knoxville, Tennessee).

---

[4] Y.-K. Kim and M. Inokuti, Phys. Rev. A 3, 665 (1971).

[5] Y.-K. Kim and J. P. Desclaux, Abstracts of Papers of the IXth International Conference on the Physics of Electronic and Atomic Collisions, Seattle, Washington, July 24-30, 1975, Eds. J. S. Risley and R. Geballe (Univ. of Washington Press, Seattle, 1975), p. 1047.

[6] Y.-K. Kim and J. P. Desclaux, Phys. Rev. Letters 36, 139 (1976).

[7] L. Armstrong, Jr., W. R. Fielder, and D. L. Lin, Phys. Rev. A 14, 1114 (1976).

[8] Argonne National Laboratory Report, ANL-76-88, Part I (1976).

FPP AND FPP-RELATED DOCUMENTS AUTHORED BY ARGONNE PERSONNEL

M. A. ABDOU, L. J. MILTON, J. C. JUNG, E. M. GELBARD
"Multidimensional Neutronics Analysis of Major Penetrations in Tokamaks," Proceedings of the Second Topical Meeting on The Technology of Controlled Nuclear Fusion, CONF-760935 - P3, Richland, Washington, September 21-23, 1976, p. 845.

S. C. AGARWAL, A. TAYLOR
"Radiation-Enhanced Precipitation in a V-10 wt% Ti Alloy," Proceedings of the Second Topical Meeting on The Technology of Controlled Nuclear Fusion, CONF-760935 - P3, Richland, Washington, September 21-23, 1976, p. 949.

W. BAUER, C. R. FINFGELD, M. KAMINSKY (Eds.)
"Surface Effects in Controlled Fusion Devices," Proceedings of the Second Conference on Surface Effects in Controlled Fusion Devices, San Francisco, California, February 16-20, 1976, published by North Holland Publishing Co.

W. F. CALAWAY, E. H. VAN DEVENTER, B. MISRA, C. J. WIERDAK, V. A. MARONI
"Review of the ANL Program on Liquid Lithium Processing Tritium Control Technology," Proceedings of the Second Topical Meeting on the Technology of Controlled Nuclear Fusion, CONF-760935 - P3, Richland, Washington, September 21-23, 1976, p. 905.

A. EI-DERINI, E. GELBARD
"Neutral Transport Code in Plasma," ANL/FPP/TM-75, (February, 1977).

M. KAMINSKY
"Ion, Photon-Surface Interactions in Fusion Reactors," Proceedings of the Second Topical Meeting on The Technology of Controlled Nuclear Fusion, CONF-760935 - P1, Richland, Washington, September 21-23, 1976, p. 169.

Y. K. KIM, J. P. DESCLAUX
"Spectroscopic and Bethe Cross Section Data for Sodium-Like Ions," ANL-76-88, Part I (RER Annual Report).

Y. K. KIM
"Relativistic Effects in Excitation Cross Sections for Stripped Ions," Oak Ridge National Laboratory, Abstract of a paper presented at the American Physical Society Conference on Atomic Process in High Temperature Plasmas, February 16-18, 1977, Knoxville, Tennessee.

V. A. MARONI
"Tritium Processing and Containment Technology for Fusion Reactors: Prespective and Status," Proceedings of the Second Topical Meeting on The Technology of Controlled Nuclear Fusion, CONF-760935 - P3, Richland, Washginton, September 21-23, 1976, p. 799.

R. F. MATTAS, H. WIEDERSICH
"Elevated-Temperature Tensile Properties of V-15Cr-5Ti Containing Helium Introduced by Ion Bombardment and Tritium Decay,"
Proceedings of the Second Topical Meeting on The Technology of Controlled Nuclear Fusion, CONF-760935 - P1, Richland, Washington September 21-23, 1976, p. 199.

F. E. MILLS, J. N. BROOKS, K. EVANS, JR., R. L. KUSTOM, W. M. STACEY, JR., T. WANG
"Plasma Driving Systems for a Tokamak Experimental Power Reactor,"
Proceedings of the Second Topical Meeting on The Technology of Controlled Nuclear Fusion, CONF-760935 - P4, Richland, Washington — September 21-23, 1976, p. 1233.

B. MISRA, V. A. MARONI
"Isotopic Enrichment of Plasma Exhausts for Controlled Thermonuclear Reactors by Cryogenic Distillation,"
Proceedings of the Second Topical Meeting of The Technology of Controlled Nuclear Fusion, CONF-760935 - P3, Richland, Washington September 21-23, 1976, p. 917.

J. NOREM
"Start-up in Tokamak Experimental Power Reactors"
ANL/FFP/TM-76, (March, 1977).

D. I. POTTER, H. A. HOFF
"Irradiation Effects on Precipitation in γ/γ' Ni-Al Alloys,"
Acta Metallurgica, 24, (1976), pp. 1155-1164.

W. PRIMAK, E. MONAHAN
"Ion Bombardment of Refractory Materials and Silicate Glasses at Elevated Temperatures,"
Bull. Am. Phys. Soc. 22, (Jan. 1977), p. 25.

J. REST, S. DANYLUK, R. B. POEPPEL
"GRASS-Code Calculation for the Behavior of Helium in Austenitic Stainless Steels,"
Proceedings of the Second Topical Meeting of The Technology of Controlled Nuclear Fusion, CONF-760935 - P1, Richland, Washington September 21-23, 1976, p. 239.

T. D. ROSSING, S. K. DAS, M. KAMINSKY
"Reduction of Surface Erosion in Fusion Reactors,"
J. of Vac. Sci. & Tech. 14(1), (1977), p. 550.

R. A. SACKS & J. E. ROBINSON
"Accurate Point Source Modeling for Extended-Source Stress,"
Bull. Am. Phys. Soc. 21, (Dec. 1977), p. 1289.

W. M. STACEY, JR., M. A. ABDOU, C. C. BOLTA, J. A. FASOLO, R. L. KUSTOM, V. A. MARONI, R. F. MATTAS, F. E. MILLS, B. MISRA, J. S. MOENICH, J. S. PATTEN, D. L. SMITH, H. C. STEVENS, S-T. WANG, C. K. YOUNGDAHL
"Tokamak Engineering Technology Facility,"
Proceedings of the Second Topical Meeting on The Technology of Controlled Nuclear Fusion, CONF-760935 - P1, Richland, Washington September 21-23, 1976, p. 95.

W. M. STACEY, JR., M. A. ABDOU, P. J. BERTONCINI, C. C. BOLTA, J. N. BROOKS, K. EVANS, JR., J. A. FASOLO, J. C. JUNG, R. L. KUSTOM, V. A. MARONI, R. F. MATTAS, J. S. MOENICH, A. MORETTI, F. E. MILLS, B. MISRA, J. H. NOREM, J. S. PATTEN, W. F. PRAEG, P. SMELSER, D. L. SMITH, H. C. STEVENS, L. TURNER, S-T. WANG, C. K. YOUNGDAHL
"Tokamak Experimental Power Reactor,"
Proceedings of the Second Topical Meeting on The Technology of Controlled Nuclear Fusion, CONF-760935 - P1, Richland Washington September 21-23, 1976, p. 21.

W. M. STACEY, JR., D. L. SMITH, J. N. BROOKS
"Impurity Control in Near-Term Tokamak Reactors,"
Proceedings of the Second Topical Meeting on The Technology of Controlled Nuclear Fusion, CONF-760935 - P1, Richland, Washington September 21-23, 1976, p. 315.

W. M. STACEY, JR., M. A. ABDOU, J. N. BROOKS, R. G. CLEMMER, K. EVANS, JR., J. A. FASOLO, S. D. HARKNESS, R. L. KUSTOM, V. A. MARONI, B. MISRA, J. S. MOENICH, A. MORETTI, J. H. NOREM, D. L. SMITH, H. C. STEVENS, L. R. TURNER, S-T. WANG, C. K. YOUNGDAHL
"EPR-77: A Revised Design for the Tokamak Experimental Power Reactor,"
ANL/FPP/TM-77, (March, 1977).

W. M. STACEY, JR., K. EVANS, JR.
"Toroidal Field Strength Requirements in Tokamak Reactors,"
Nuclear Technology, 32, (Feb. 1977).

H. C. STEVENS, M. A. ABDOU, R. F. MATTAS, V. A. MARONI, J. S. PATTEN, D. L. SMITH, D. K. YOUNGDAHL
"Tokamak Experimental Power Reactor Primary Energy Conversion System,"
Proceedings of the Second Topical Meeting on The Technology of Controlled Nuclear Fusion, CONF-760935 - P4, Richland, Washington September 21-23, 1976, p. 1551.

E. H. VAN DEVENTER, T. A. RENNER, R. H. PELTO, V. A. MARONI
"Effects of Surface Impurities on the Hydrogen Permeability of Vanadium,"
J. of Nucl. Materials, 64(3), (1977), p. 241.

S. T. WANG, L. R. TURNER, R. E. MILLS, D. W. DEMICHELE, P. SMELSER, S. H. KIM
"Conceptual Design of Superconducting Magnet Systems for the Argonne Tokamak Experimental Power Reactor,"
Proceedings of the Second Topical Meeting on The Technology of Controlled Nuclear Fusion, CONF-760935 - P4, Richland, Washington September 21-23, 1976, p. 1283.

Distribution of ANL/FPP-77-1

Internal:

M. Abdou, P. Bertoncini, K. Evans, J. Jung
C. C. Bolta, H. C. Stevens
I. Charak, P. Persiani
J. B. Darby, Jr.
E. Gelbard, C. Boley, D. Ehst
D. M. Gruen
S. D. Harkness
R. R. Heinrich, F. Cafasso
M. S. Kaminsky, S. Das
R. L. Kustom, J. Fasolo, S-T. Wang
V. A. Maroni
H. Wiedersich, F. Nolfi, D. L. Smith
R. Avery
L. Burris, Jr.
E. J. Croke
S. A. Davis
P. R. Fields
B. R. T. Frost
P. F. Gustafson
R. V. Laney
R. L. Martin
M. V. Nevitt
E. N. Pettitt
E. G. Pewitt
D. C. L. Price
R. J. Royston
R. G. Sachs
W. K. Sinclair
W. M. Stacey, Jr.
R. G. Staker
C. E. Till
R. S. Zeno
G. T. Garvey
FP Program (41)
ANL Contract Copy
ANL Libraries (5)
TIS Files (5)

External:

ERDA-TIC, for distribution per UC-20 (190)
Manager, Chicago Operations Office
Chief, Chicago Patent Group
President, Argonne Universities Association
Applied Physics Division Review Committee:
- P. Greebler, General Electric Co., Sunnyvale
- R. L. Hellens, Combustion Engineering, Inc.
- J. M. Hendrie, Brookhaven National Lab.
- W. B. Loewenstein, Electric Power Research Inst.
- D. B. Wehmeyer, Detroit Edison
- S. A. Werner, Univ. Missouri

Chemical Engineering Division Review Committee:
- R. C. Axtmann, Princeton Univ.
- R. E. Balzhiser, Electric Power Research Inst.
- J. T. Banchero, Univ. Notre Dame
- D. L. Douglas, Gould Inc.
- P. W. Gilles, Univ. Kansas
- R. I. Newman, Allied-General Nuclear Services
- G. M. Rosenblatt, Pennsylvania State Univ.

Chemistry Division Review Committee:
- J. Bigeleisen, Univ. Rochester
- W. H. Flygare, Univ. Illinois
- H. F. Franzen, Iowa State Univ.
- D. R. Herschbach, Harvard Univ.
- E. L. Muetterties, Cornell Univ.
- J. O. Rasmussen, Lawrence Berkeley Lab.
- F. S. Rowland, Univ. California, Irvine
- J. H. Wang, State Univ. New York, Buffalo

Components Technology Division Review Committee:
J. W. Dally, Univ. Maryland
W. E. Kessler, Commonwealth Associates
N. C. Rasmussen, Massachusetts Inst. of Technology
M. A. Schultz, Pennsylvania State Univ.
A. Sesonske, Purdue Univ.
H. Thielsch, ITT Grinnell Corp.

Materials Science Division Review Committee:
G. S. Ansell, Rensselaer Polytechnic Inst.
R. W. Balluffi, Cornell Univ.
S. Doniach, Stanford Univ.
H. L. Falkenberry, Tennessee Valley Authority
C. Laird, Univ. Pennsylvania
D. Lazarus, Univ. Illinois
M. T. Simnad, General Atomic
A. R. C. Westwood, Martin Marietta Labs.

Physics Division Review Committee:
D. A. Bromley, Yale Univ.
W. L. Brown, Bell Telephone Labs.
H. Feshbach, Massachusetts Inst. of Technology
R. Middleton, Univ. Pennsylvania
D. E. Nagle, Los Alamos Scientific Lab.
D. A. Shirley, Univ. California, Berkeley

Reactor Analysis and Safety Division Review Committee:
W. Kerr, Univ. Michigan
M. Levenson, Electric Power Research Inst.
S. Levy, General Electric Co., San Jose
R. B. Nicholson, Exxon Nuclear Co., Inc.
D. Okrent, Univ. California, Los Angeles

Solid State Science Division Review Committee:
C. P. Flynn, Univ. Illinois

ZGS Complex Review Committee:
V. W. Hughes, Yale U.
J. D. Jackson, Univ. California, Berkeley
W. Lee, Columbia Univ.
R. B. Neal, Stanford Linear Accelerator Center
J. L. Rosen, Northwestern Univ.
G. H. Trilling, Lawrence Berkeley Lab.

N. Amherd, Electric Power Research Inst.
C. C. Baker, General Atomic Co.
J. Baublitz, R. Kostoff, M. Murphy, ERDA/DMFE
R. Boom, G. L. Kulcinski, C. W. Maynard, R. Conn, Univ. Wisconsin
W. Briggs, D. Kummer, McDonnell-Douglas
S. J. Buchsbaum, Bell Telephone
G. A. Carlson, R. W. Werner, Lawrence Livermore Lab.
R. A. Carruthers, R. Hancox, Culham Lab.
R. Challender, United Kingdom Atomic Energy Authority
F. F. Chen, Univ. California
J. F. Clarke, Oak Ridge National Lab.
M. Clarke, Combustion Engineering
F. Coffman, S. L. Bogart, J. Neff, B. Twining, ERDA/DMFE
M. F. Collins, E. Golankiewicz, Engelhard Minerals and Chemical Corp.
E. C. Creutz, National Science Foundation
N. A. Davies, R. Blanken, D. Ignat, J. Willis, ERDA/DMFE

S. O. Dean, A. M. Sleeper, ERDA/DMFE
J. F. Decker, G. J. Mischke, P. Stone, ERDA/DMFE
D. Dingee, Pacific Northwest Laboratories
W. E. Drummond, Univ. Texas, Austin
W. L. Ellis, E. Oktay, ERDA/DMFE
S. Fernbach, Lawrence Livermore Lab.
H. Finger, Center for Energy Systems
Bibliotheque, Fontenay-aux-Roses, Service du Confinement des Plasmas, CEA
H. K. Forsen, Exxon Nuclear Co.
T. K. Fowler, Lawrence Livermore Lab.
H. P. Furth, Princeton Univ.
M. B. Gottlieb, Princeton Univ.
W. C. Gough, Electric Power Research Inst.
J. N. Grace, L. K. Price, ERDA/DMFE
D. Grafsteen, Exxon Research and Engineering Co.
R. A. Gross, Columbia Univ.
A. F. Haught, United Technologies Research Center
C. Henning, ERDA/DMFE
N. Hershkowitz, K. E. Lonngren, W. R. Savage, Univ. Iowa
A. Hill, Massachusetts Institute of Technology
R. L. Hirsch, ERDA/ASGA
H. Hurwitz, General Electric
G. R. Ingram, ERDA/DMFE
E. E. Kintner, ERDA/DMFE
H. Kouts, Brookhaven National Lab.
W. B. Kunkel, Lawrence Livermore Lab.
R. Lengye, Bibliothek, Max-Planck Institut fur Plasmaphysik
Library, Centre, de Recherches en Physique des Plasma
Library, Culham Lab.
Library, FOM Institut voor Plasma-fysica, The Netherlands
Library, Japan Atomic Energy Research Institute
Library, Kurchatov Institute, U.S.S.R.
Library, Laboratorio Gas Ionizati, Italy
L. Lidsky, Massachusetts Institute of Technology
G. H. Miley, F. Y. Southworth, R. Turnbull, University of Illinois
T. Ohkawa, General Atomic Co.
G. D. Pine, Massachusetts Institute of Technology
R. E. Price, W. L. Sadowski, D. M. Priester, ERDA/DMFE
J. Raeder, West Germany
T. Reuther, ERDA/DMFE
F. Ribe, Los Alamos Scientific Lab.
R. Sambaugh, General Atomic Co.
K. H. Schmitter, Max-Planck-Institute fur Plasmaphysik, West Germany
Z. Shapiro, Westinghouse
D. Stekart, ERDA/APAE
D. Swanson, Washington, D.C.
C. Taylor, Lawrence Livermore Lab.
J. Williams, ERDA/DMFE
K. Zwilsky, W. Bennett, M. M. Cohen, E. Dalder, C. R. Finfgeld, ERDA/DMFE